REPORT DOCUMENTATION PAGE

1. AGENCY USE ONLY (Leave blank)	2. REPORT DATE April 25, 1995	3. REPORT TYPE AND DATES COVERED Final Report: 1 Apr 94 – 1 Feb 95

4. TITLE AND SUBTITLE

Investigation of Fracture Resistance in Microstructures of Intermetallic Materials for High Temperature Service

6. AUTHOR(S)

David L. Davidson and Kwai S. Chan

5. FUNDING NUMBERS

61102F 2306 AS

7. PERFORMING ORGANIZATION NAME(S) AND ADDRESS(ES)

Southwest Research Institute
6220 Culebra Road
San Antonio, TX 78238-5166

AFOSR-TR-96 97

0021

9. SPONSORING/MONITORING AGENCY NAME(S) AND ADDRESS(ES)

AFOSR/NE
110 Duncan Ave., Suite B115
Bolling AFB CA 20332-0001

10. SPONSORING/MONITORING AGENCY REPORT NUMBER

F49620-92-C-0022

11. SUPPLEMENTARY NOTES

12a. DISTRIBUTION/AVAILABILITY STATEMENT

APPROVED FOR PUBLIC RELEASE; DISTRIBUTION IS UNLIMITED.

12b. DISTRIBUTION CODE

13. ABSTRACT (Maximum 200 words)

In situ composites based on the intermetallic Cr_2Nb were formulated, fabricated, and tested to determine the effects of alloy design on fatigue and fracture toughness. Studies of Nb-Cr *in situ* composites indicated that these materials were not sufficiently damage tolerant to warrant detailed fracture studies. Alloying with titanium increased the fracture toughness of the matrix to ≈ 80 MPa$\sqrt{m}$ and the composites to ≈ 20 MPa$\sqrt{m}$, but the toughness of Cr_2Nb remained unchanged at ≈ 1.5 MPa$\sqrt{m}$. However, fracture toughness of the composites is still lower than anticipated.

Fatigue cracks were grown in the best of these materials and detailed micromechanics measurements were made. The fatigue crack growth characteristics of the high toughness matrix alloy were similar to pure Nb at higher values of ΔK where cracks in the new alloy grew much more slowly. Crack growth through the Nb-Cr-Ti composite were faster and at lower values of ΔK. Similar measurements were made in a Nb-10 at.% Si composite. Reasons for the fatigue crack growth behavior observed were that the crack tip strains for the composites were lower than matrix alloy under comparable conditions; thus, the number of cycles ΔN required for crack advanced was decreased. Also, the average increment of crack advance Δa was increased by fracture of the intermetallic. The decrease in fracture strain was attributed to an increase in the level of constraint caused by presence of the reinforcing intermetallic particles.

14. SUBJECT TERMS	15. NUMBER OF PAGES 118
	16. PRICE CODE

17. SECURITY CLASSIFICATION OF REPORT	18. SECURITY CLASSIFICATION OF THIS PAGE	19. SECURITY CLASSIFICATION OF ABSTRACT	20. LIMITATION OF ABSTRACT
UNCLASSIFIED	UNCLASSIFIED	UNCLASSIFIED	

DTIC QUALITY INSPECTED 1

19970117 087

TABLE OF CONTENTS

LIST OF FIGURES

LIST OF FIGURES (continued)

LIST OF FIGURES (continued)

Page

LIST OF TABLES

EXECUTIVE SUMMARY

Research performed during the past 3 years has represented a transition from the detailed study of the fracture of TiAl-based alloys, which are just beginning to be used in gas turbine engines, to a new material system for use in gas turbine engines of the future. These materials, termed *in situ* composites and based on the intermetallic Cr_2Nb, were formulated, fabricated, and tested to determine the effects of alloy design on fatigue and fracture toughness. This report first presents detailed results of the fracture research on the Nb-based *in situ* composites, which is just reaching publication stage, then summarizes briefly the mechanical properties studies of TiAl-based alloys, most of which have been published.

It was soon determined from studies of Nb-Cr two-phase, *in situ* composites, that these materials were not sufficiently damage tolerant to warrent detailed mechanistic studies of their fracture characteristics. Alloying with titanium increased the fracture toughness of the matrix to ≈ 80 MPa$\sqrt{m}$ and the composites to ≈ 20 MPa$\sqrt{m}$, but the toughness of Cr_2Nb remained unchanged at ≈ 1.5 MPa$\sqrt{m}$. A patent application was made for the compositions resulting in the highest damage tolerance. However, fracture toughness of the composites was lower than anticipated.

Fatigue cracks were grown in the best of these materials and detailed micromechanics measurements were made. The fatigue crack growth characteristics of the high toughness matrix alloy were similar to pure Nb except at higher values of ΔK where cracks in the new alloy grew much more slowly. Crack growth through the Nb-Cr-Ti composite was faster and at lower values of ΔK. Similar measurements were made in a Nb-10 at.% Si composite obtained from the Materials Laboratory at Wright Patterson Air Force Base. This composite behaved more like pure Nb than did the Nb-Cr-Ti composite.

Reasons for the fatigue crack growth behavior observed were that the crack tip strains for the composites were lower than matrix alloy under comparable conditions; thus, the number of cycles ΔN required for crack advance was decreased. Also, the average increment of crack advance Δa was increased by fracture of the intermetallic. The decrease in fracture strain was attributed to an increase in the level of constraint caused by presence of the reinforcing intermetallic particles.

PERSONNEL

The following personnel obtained partial support from this contract during the past year:

Principal Investigators: Drs. D. L. Davidson and K. S. Chan

Technical Support: J. B. Campbell, B. K. Chapa, and J. F. Spencer

Subcontractor: Dr. D. L. Anton, United Technologies Research Center

I. NIOBIUM-BASED ALLOYS: ALLOY DEVELOPMENT AND FRACTURE STUDIES

A. Introduction

This section presents background as to why fracture in the Nb-Cr system was under investigation, the problems encountered in research on the Nb-Cr system, and outlines the reasoning used in alloy development undertaken to surmount those problems. One composite made from the Nb-Si system was also tested, and these results will be compared to those from the Nb-Cr-Ti system.

Shah and Anton [1,2] evaluated several refractory intermetallic alloys for use at temperatures exceeding superalloy use temperatures. Test results from Cr_2Nb indicated a very low creep rate and an inherently good oxidation resistance; however, this material is also known to be extremely brittle, as are most refractory intermetallics. Anton and Shah [3] subsequently showed that the concept of ductile phase toughening was a possible method for overcoming this extreme brittleness. They determined, by microhardness indentation, that additions of Nb deflected cracks and caused them to blunt. These results provided the basis of research designed to further explore the effects of ductile phase toughening in the Cr_2Nb/Nb system.

B. Alloy Development

1.   Introduction: The fracture characteristics of several two phase alloys, or "*in situ* composites" of the Nb-Cr system were evaluated and found to have low values of fracture toughness relative to other engineering materials. It was determined that the toughness of the Nb phase was causing the low toughnesses, so alloying was sought as a remedy for this problem.

2. Nb-Cr Alloys: The fracture toughness Cr_2Nb was measured with 3-point bend tests to be about $1.5 \text{ MPa}\sqrt{m}$. Two phase binary alloys of Nb and Cr (Cr_2Nb dispersed in Nb solid solution) showed a 4-fold increase in toughness increase to about $5 \text{ MPa}\sqrt{m}$, an indication of "ductile phase toughening," but this toughness level is too low for practical alloys. The effect of alloy composition on fracture toughness is shown in **Figure 1**.

Not only were the levels of fracture toughness (K_Q) of the binary alloys too low for engineering application, they were too low for practical evaluation of fatigue crack growth rates. For example, the crack growth rates of two of these alloys were measured, as shown in **Figure 2**.
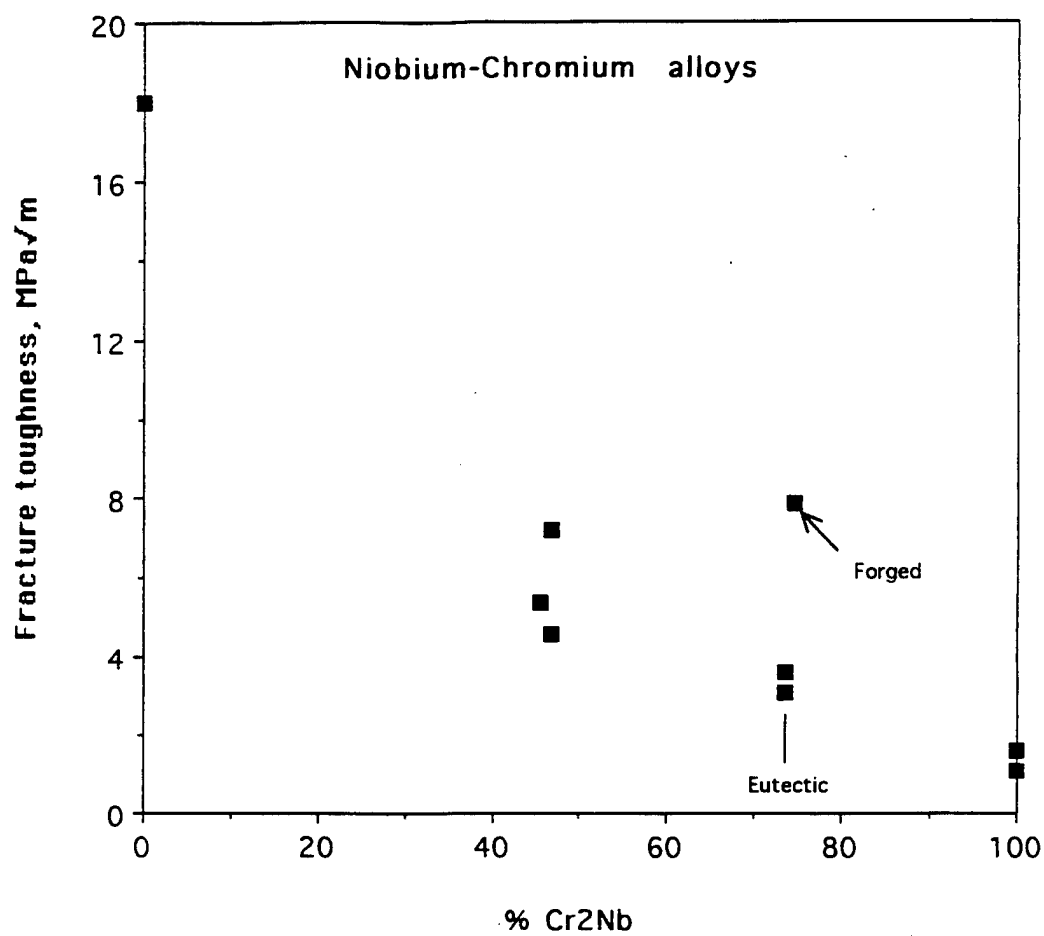
Fig. 1. Fracture toughness of pure niobium and alloys containing Cr$_2$Nb. An increased volume fraction of niobium solid solution increased the toughness of the composites to $\approx$ 6 MPa$\sqrt{m}$ from $\approx$ 1.5 MPa$\sqrt{m}$ for Cr$_2$Nb.
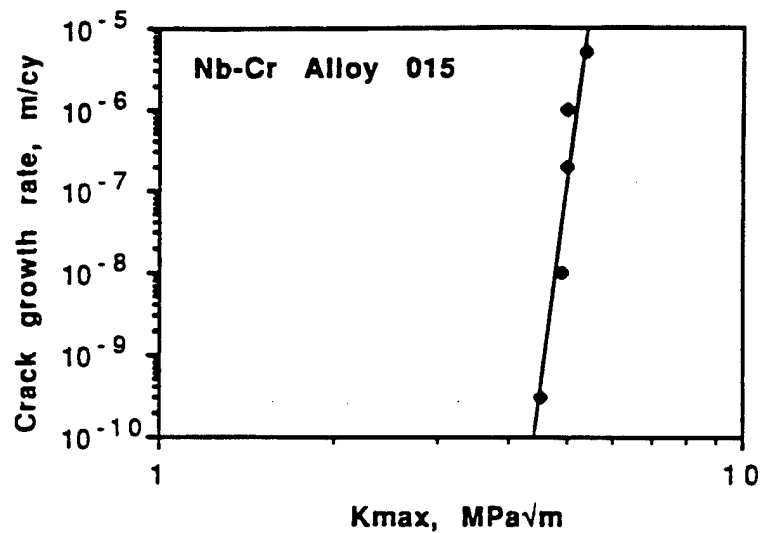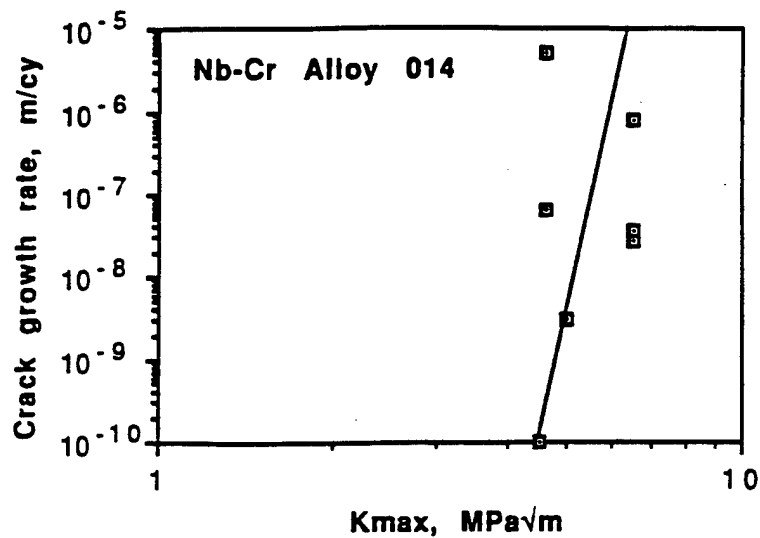
Fig. 2. Fatigue crack growth results from binary Nb-Cr composites
90-014 and 90-015. Slopes of these curves are very steep
indicating the poor damage tolerance of these composites.
Material 014 had 44 vol.% and 015 had 32 vol.% Cr_2Nb.

These curves were very difficult to obtain experimentally because of the low value of K_Q and high level of the threshold for fatigue crack growth (ΔK_{th}). From these results, it appeared that the slopes of the binary alloys would range from 20 to 100, which is an indication of their very poor damage tolerance. An example of fractography from these fatigue samples is shown in **Figure 3**, which shows that the "ductile" phase is failing without evidence of significant ductility. Increased toughness of this phase would be required if significant damage tolerance was to be obtained by this method.

Results from fracture experiments on the binary alloys indicated that it was impractical to perform detailed analyses of the processes accompanying either fatigue or toughness evaluation tests. It was imperative that the toughness of these *in situ* composites be raised before considerable effort was expended on understanding the fracture mechanisms. Alloying was certainly the first choice of methods to increase the plastic deformation of the "ductile" phase. A screening test using non-fatigue precracked, notched, 3-point bend specimens was chosen for the evaluation of alloys because of simplicity and low-cost.

3. Nb-Cr-Ti Alloys:

Considerable effort was expended in deciding which elements might be candidates for alloying with the Nb-Cr binary system to increase toughness. During this time of consideration, The Minerals, Metals, and Materials Society held a symposium on refractory alloys in which a paper was presented by R.T. Begley that summarized the effects of alloying on the properties of niobium [4]. The only alloying element shown that did not have a large effect on the temperature for a 10% reduction in area was titanium. Conversely, chromium was shown to have a very strong effect, raising the temperature by 100°C for ≈ 4 at.% addition. This information was interpreted as indicating that if titanium were substituted for chromium in solid solution, the ductility of the alloy would increase; i.e., the deleterious effects of chromium could be offset by titanium additions.

The inherent ductility in bcc transition metals (groups IVB to VIIB and VIII of the Periodic Table of the Elements) is a result of dislocation motion, which is controlled by stress level and thermal activation over the Peierls energy barrier between equilibrium locations of atoms on the slip plane. The height of the Peierls energy barrier is a direct consequence of the bonding between atoms, which for transition metals is mainly a result of d-shell electron interaction. The d-electrons have highly directional orbits which causes covalent bonding. This is offset somewhat by the s-shell electrons, and the result is hybridization between the s and d electrons that causes the transition metals to be metallic, yet exhibit many crystallographic effects that separate their deformation characteristics from non-transition metals.
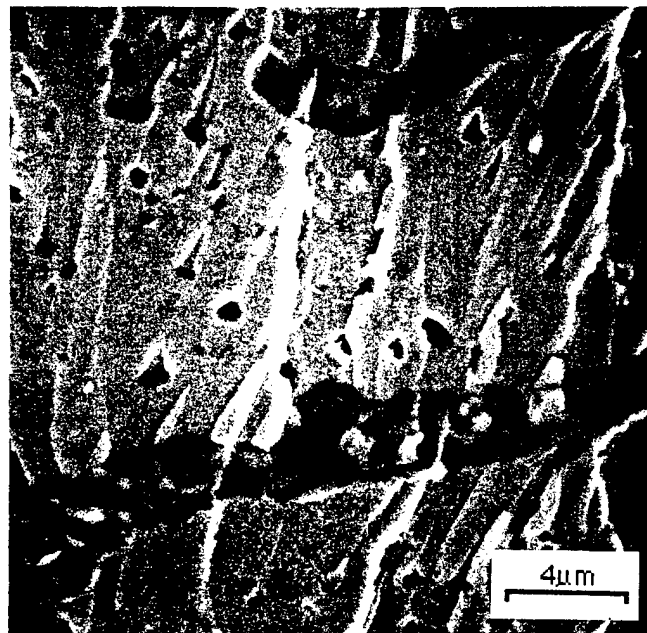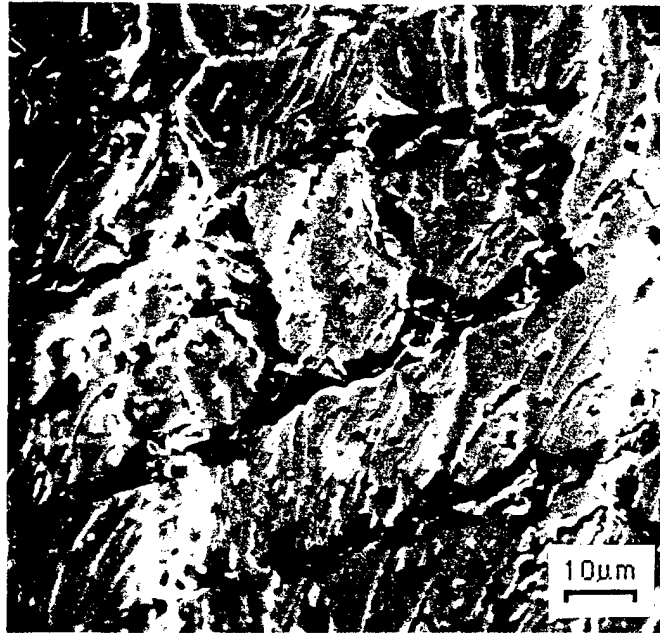
Fig. 3   Secondary electron images from the fatigue fracture surface of the 32 vol.% Cr_2Nb composite (90-015). No striations were found and behavior of both phases of the composite appeared brittle. Crack growth direction was from bottom to top.

The number of d+s electrons per atom is a good indication of the level of directional bonding, and, therefore, the height of the Peierls stress. The most highly directional bonding occurs for chromium, molybdenum, and tungsten, the group VIB elements, which have half filled d-shells (five electrons per atom), and the highest melting temperatures of any elements in their respective rows of the Periodic Table. More or less electrons per atom result in a lower level of covalent bonding, therefore, a lower Peierls stress, and a greater tendency for plastic deformation.

Addition of Cr to Nb increases the number of d+s electrons per atom; therefore, a decrease in ductility should be expected, as was observed for Cr in solid solution with Nb. Additions of elements to the left of group VIB to Nb-Cr would lower the concentration of d+s electrons and should increase the ductility of the alloy. Titanium, a group IVB element, was selected because it has a lower density than the other IVB elements, is a more common element, and there is a high solid solubility of Ti in Nb.

Presentations of papers by Perepezko and Thoma indicated that a ternary phase diagram for the Nb-Cr-Ti system had been derived by their research. Thus, a copy of Dan Thoma's PhD Dissertation at the University of Wisconsin was obtained [5], and used as guidance in deciding on how much titanium to use in alloying. Shown in **Figure 4** is Thoma's ternary diagram at 1800°C with solid solution and tie lines shown. The location of the eutectic trajectory was added by analysis of Thoma's phase diagrams at various temperatures.

Thirteen Nb-Cr alloys containing various concentrations of Ti were cast and heat treated, resulting in both single and two phase materials. Fracture toughness (K_Q) screening tests of these alloys were conducted using 25 mm long 3-point bend specimens with a/w = 0.5 for the notch. Several tests were performed on each alloy. In addition, K_Q data for other compositions were generated by Fleischer and Zabala [6] and some pieces of another Nb alloy were obtained and tested [7]. This material, obtained from Oak Ridge National Laboratories, also contained some aluminum.

The results of the fracture toughness screening tests from 3-point bend specimens are shown in **Figure 5** in the context of the ternary phase diagram and the number of electron per atom. As may be seen, there is a large increase in toughness of the solid solution alloy at 50Nb-13Cr-37Ti, which was unexpected on the basis of the number of electrons per atom. Fracture toughness of the accompanying two phase alloys on approximately the same tie lines, containing about 22 and 38 volume percent Cr_2Nb, are also higher than other alloys of nearby compositions, which is an
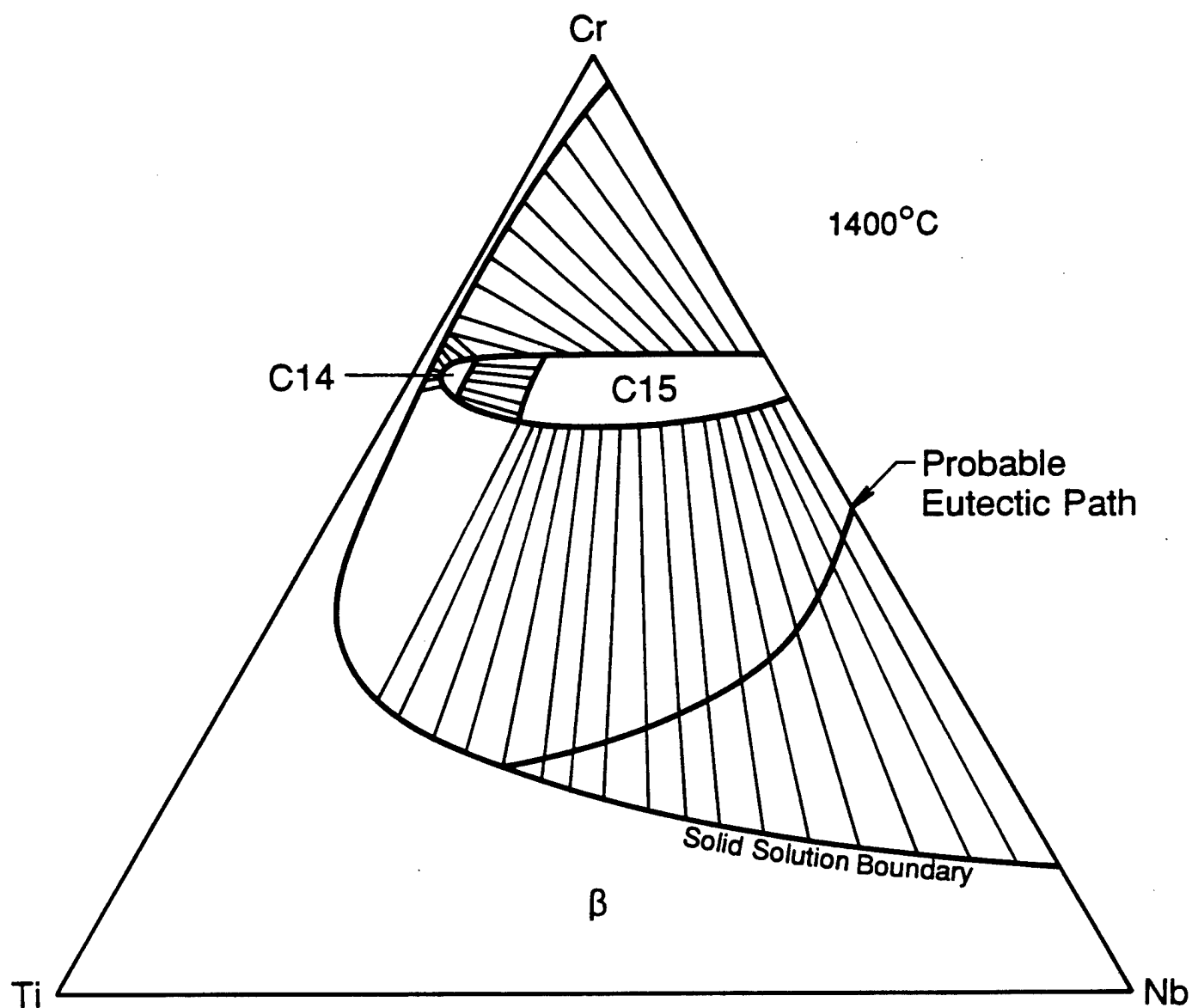
Fig. 4 Ternary phase diagram, derived from the work of Thoma [5]. Solid solution boundary at 1400°C, the probable eutectic path (varies in temperature) and tie lines for the two phase regions are shown. The intermetallic Cr_2Nb can have two crystal structures C14 and C15.
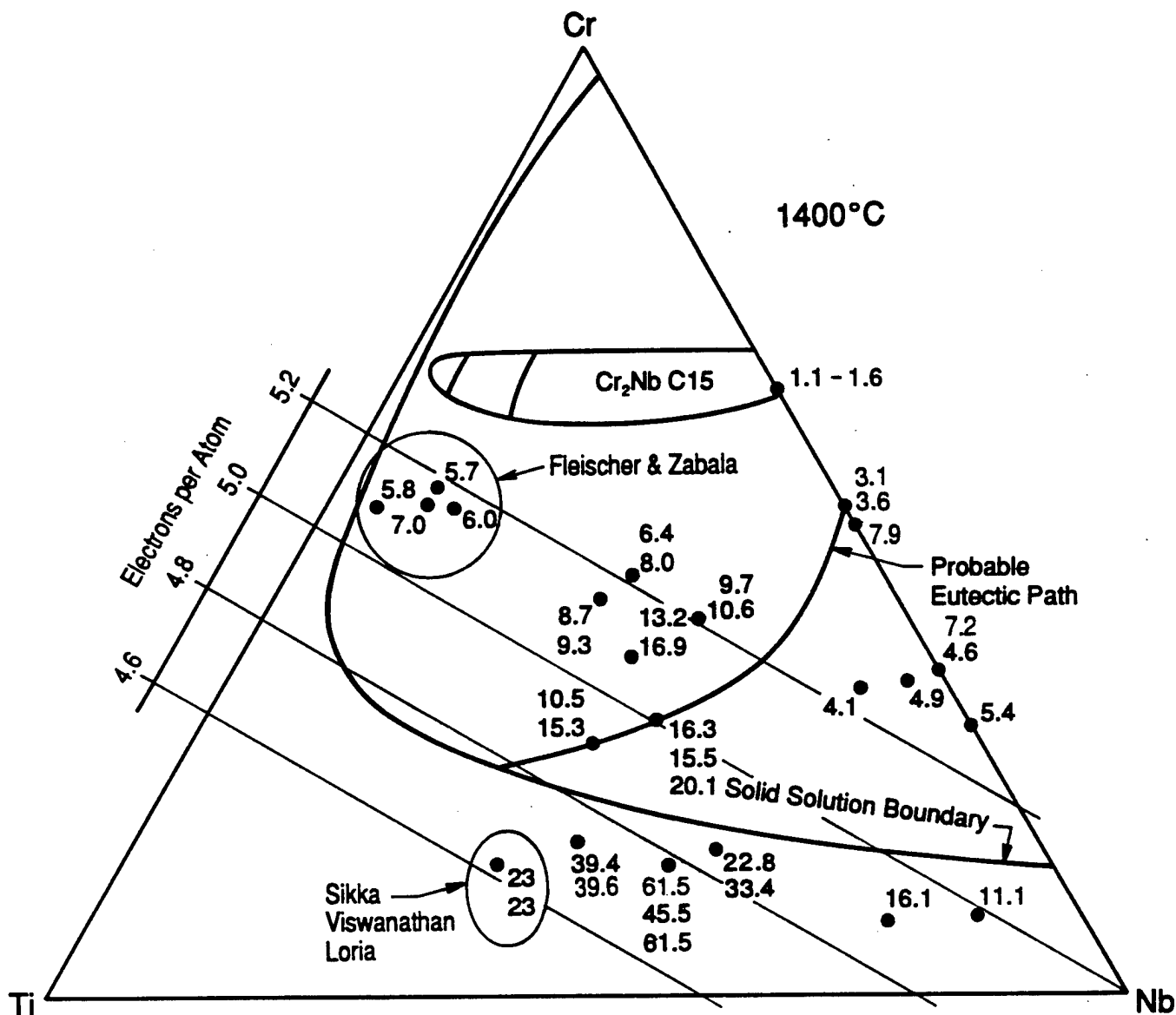
Fig. 5   Ternary phase diagram from Thoma showing lines of equal electrons per atom and the measured fracture toughness values for single phase and composite specimens made from arc melted and heat treated, and in some cases forged and reheat treated boules of the compositions shown. Also indicated on the figure are K_Q values reported by Fleischer and Zabala [6], and K_Q measured from the material of Sikka, et al. [7].

indication that the higher toughness of the matrix composition is preserved in the two phase alloys. Correlation of measured K_Q with the number of d+s electrons is shown **Figure 6**. The surprising aspect of these results is the maximum in toughness that occurs at about 4.7 d+s electrons per atom.

Another way to see the effect of composition and volume fraction of Cr_2Nb is through the cross sections of the ternary phase diagram shown in **Figure 7**. In the section having 10-20 at.% Cr, which is in the single phase region, the maximum toughness occurs at $\approx$ 37 at.% Ti, while in the two phase region, the maximum toughness is likely to occur at 30-35 at.% Ti.

One interpretation of the microstructure of these materials is that they are a matrix alloy containing additions of intermetallic phase much in the same way as composites have been formed by additions of SiC and Al_2O_3 to aluminum alloys. Thus, in interpreting the mechanical properties of these two phase niobium alloys, they will be considered as being *in situ* composites.

The volume fraction of Cr_2Nb in the composite has a large effect on the fracture toughness, as is shown in **Figure 8**. Shown for comparison to experimental results are fracture toughness values calculated from the rule of mixtures (ROM) with and without considering the differences in modulus between Nb and Cr_2Nb. In either case, the fracture toughness of the composites are below that derived from by ROM. The simplest interpretation of this result is that the materials containing Cr_2Nb have a "toughness deficit." The question to be asked is why the toughness of these *in situ* composites is so much lower than they could be potentially. The results of two models by Ashby [8] that assume the crack is growing only in a continuous brittle phase, the K_{min} model, and a model that assumes that crack bridging is the dominant toughening mechanism, the Kmax model were used also for comparison with these results. The K_{max} model predicts values above the E-modified ROM line, while the K_{min} model predicted values approximately along the Nb-Cr line. For the Nb-Cr-Ti composites, the experimental results are very different than predicted by either of these models.

Microstructures the Nb-Cr-Ti composites tested are shown in **Figure 9**. These composites are on the same tie line as the toughest solid solution alloy 93-018 and represent two volume fractions of Cr_2Nb. The composition of 93-016 is approximately that of the eutectic.

Macro-fractography of some of the 3-point bend specimens is shown in **Figure 10**. The fractographs selected demonstrate that the appearance of the fracture surfaces is unrelated to the level of fracture toughness measured.
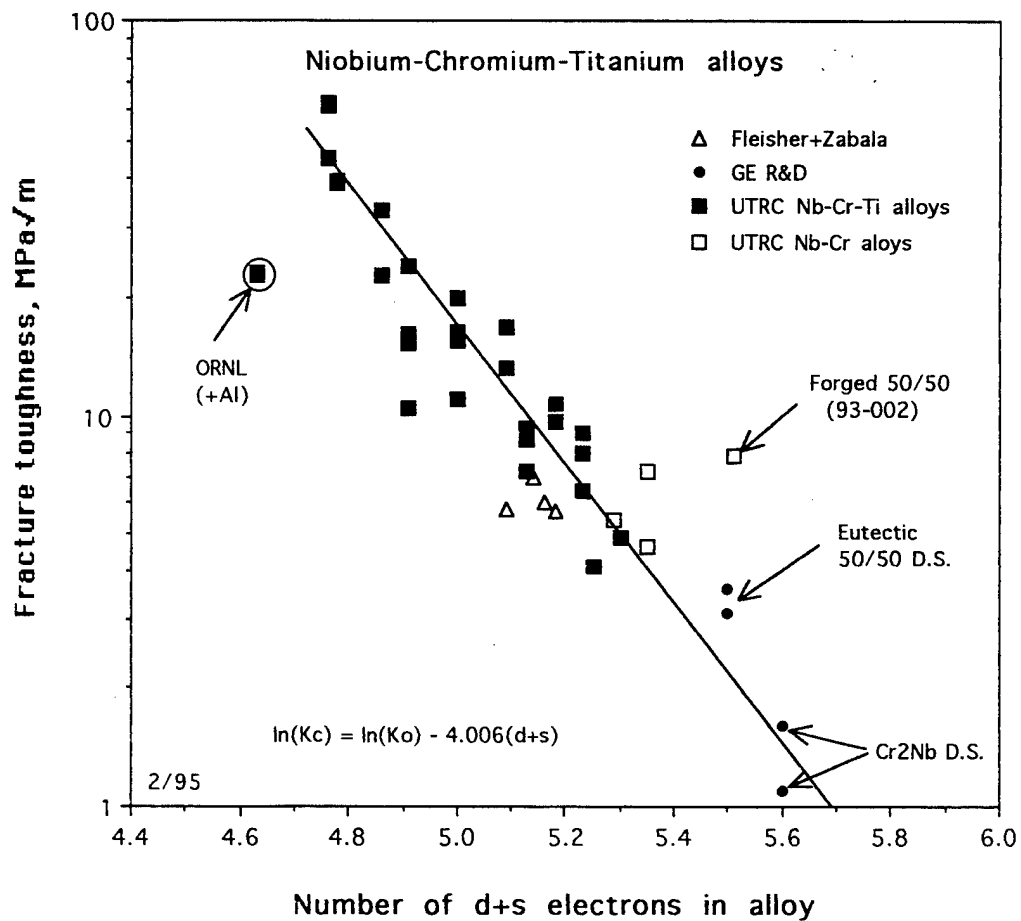
Fig. 6   Correlation between measured K_Q values and the number of d+s bonding electrons in the alloy.
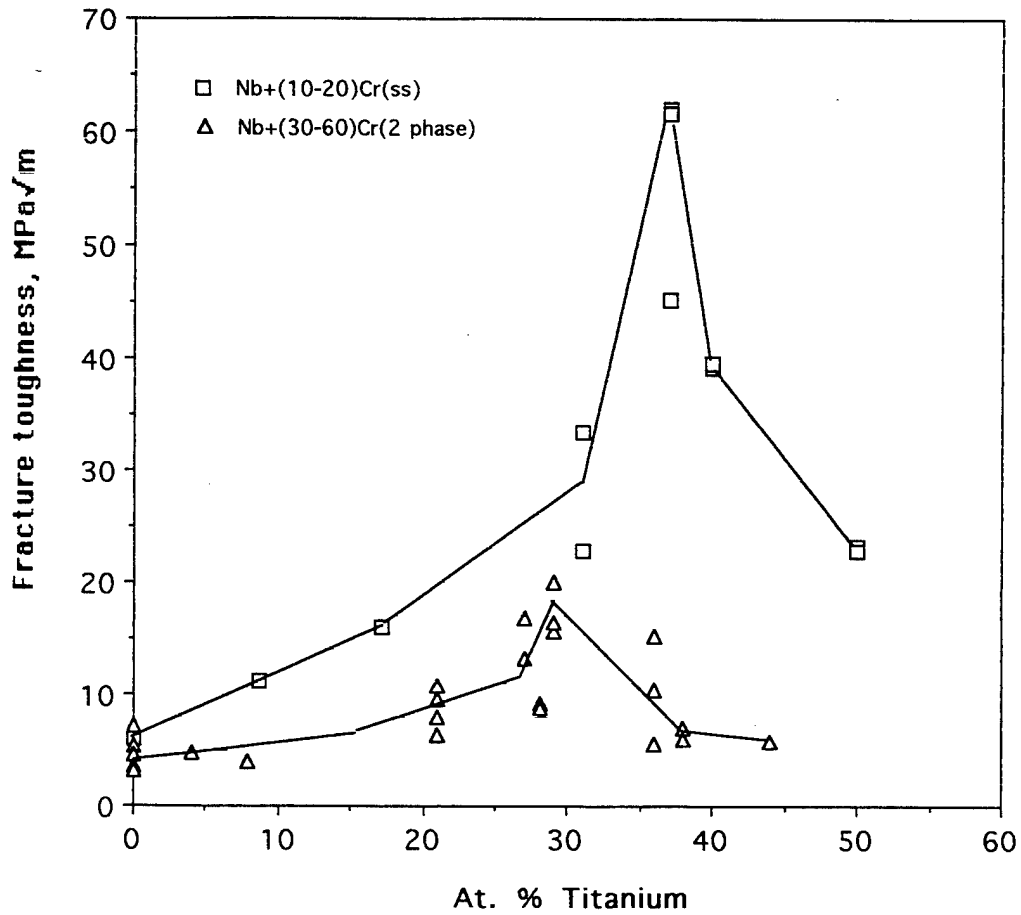
Fig. 7 Cross sections through Fig. 5 within the solid solution range (10-20 at.% Cr) and two phase region (30-60 at.% Cr) showing the unexpectedly large increase in K_Q values found for 30-40 at.% Ti additions.
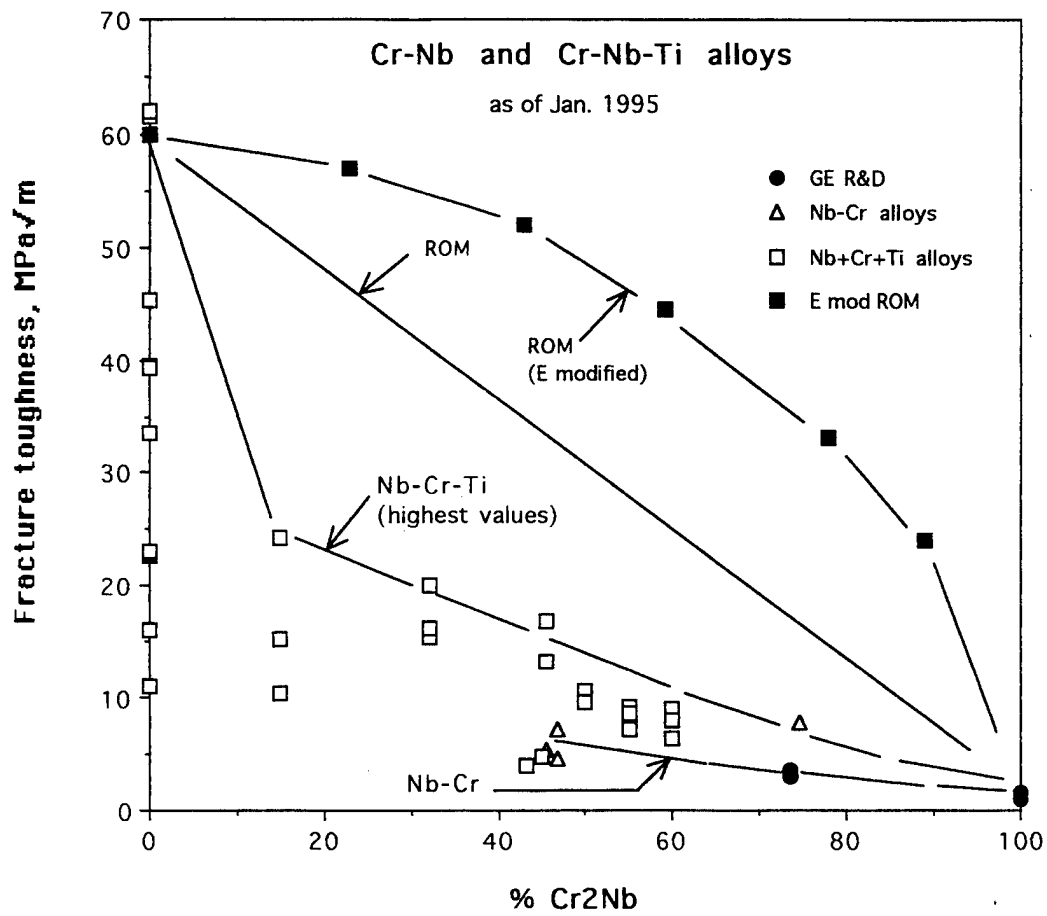
Fig. 8   Fracture toughness as a function of the vol.% of Cr_2Nb. For comparison with measured values, rule of mixtures (ROM) and ROM modified by modulus values are shown.
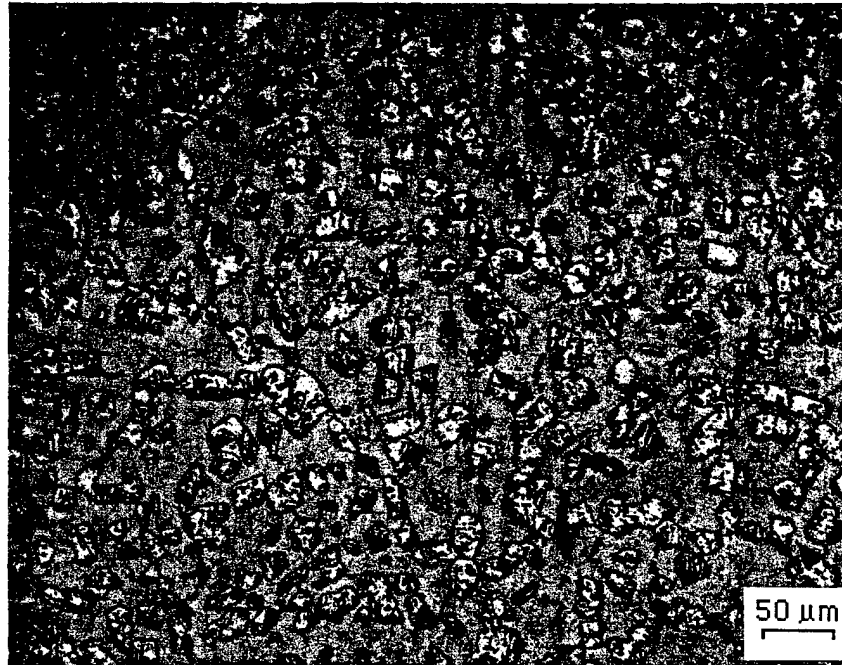
(a) 93-015 cast and heat treated
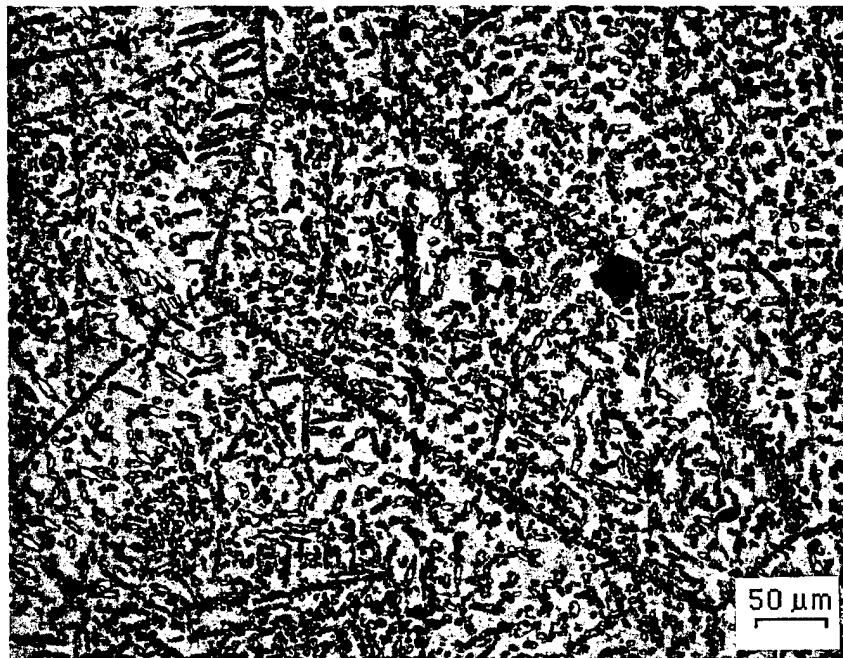
(b) 93-016 cast and heat treated

Fig. 9   Microstructures of composites 93-015 (37Nb-36Cr-27Ti) and 93-016 (42Nb-29Cr-29Ti). In 93-015, cast and after forging, the Cr_2Nb particles are well dispersed, but in 93-016, Cr_2Nb has formed on the grain boundaries for both cast and forged materials.

15
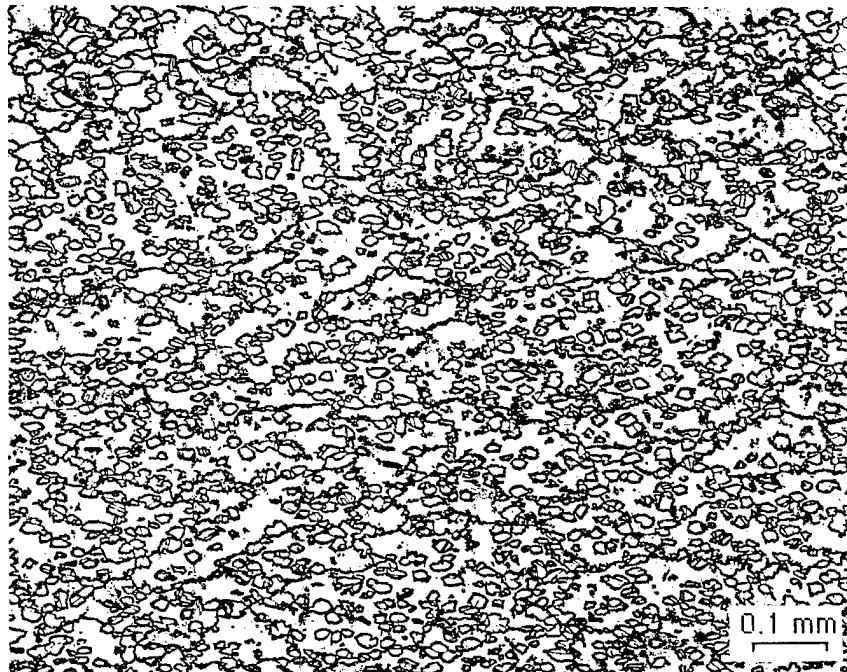
(c) 93-015F forged and heat treated
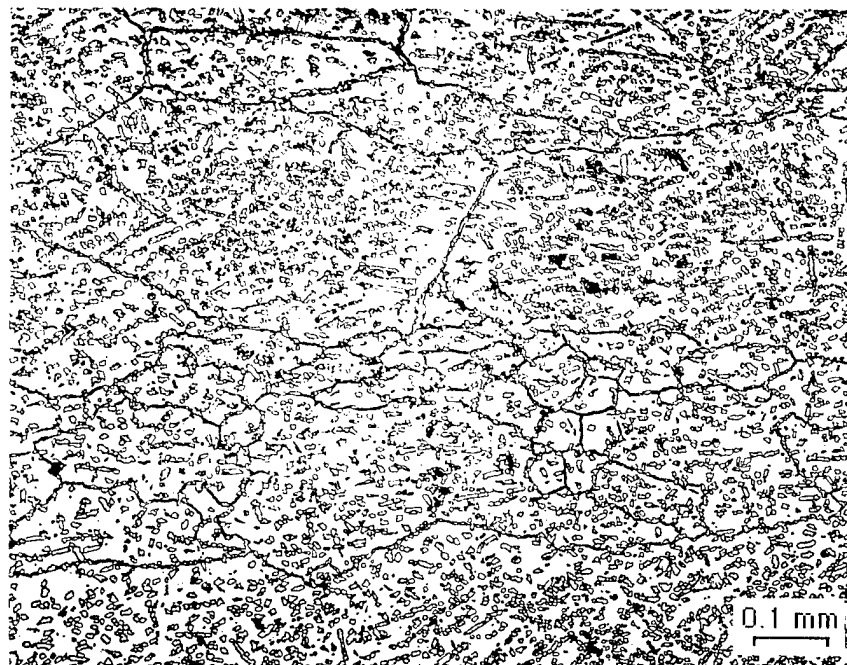
(d) 93-016 forged and heat treated

Fig. 9 continued.

16
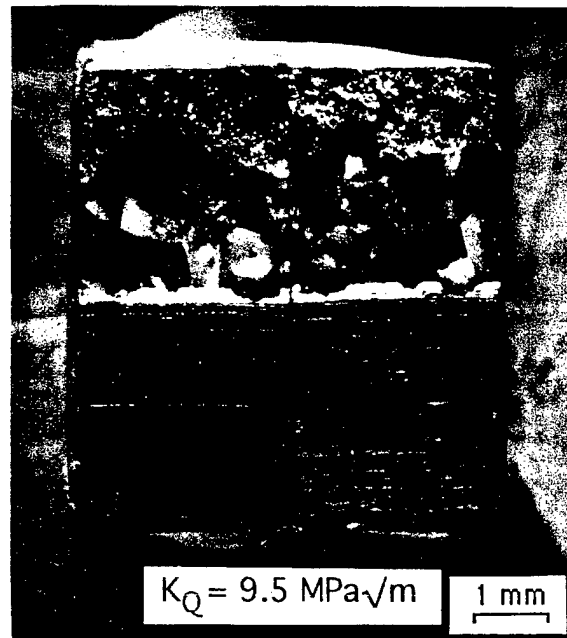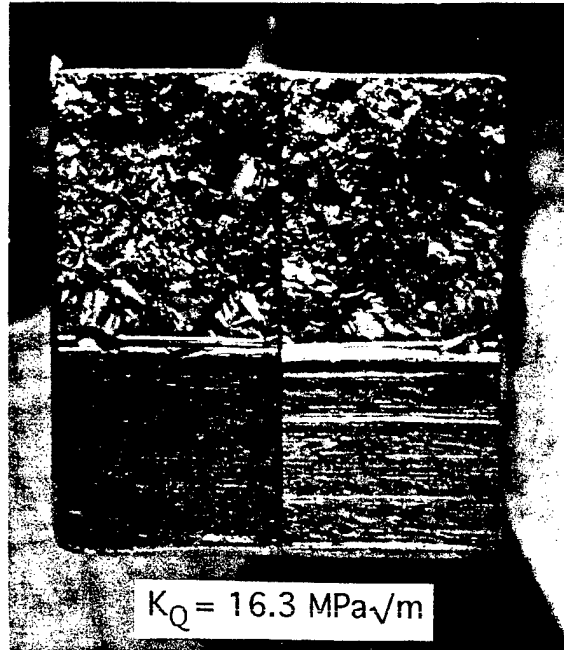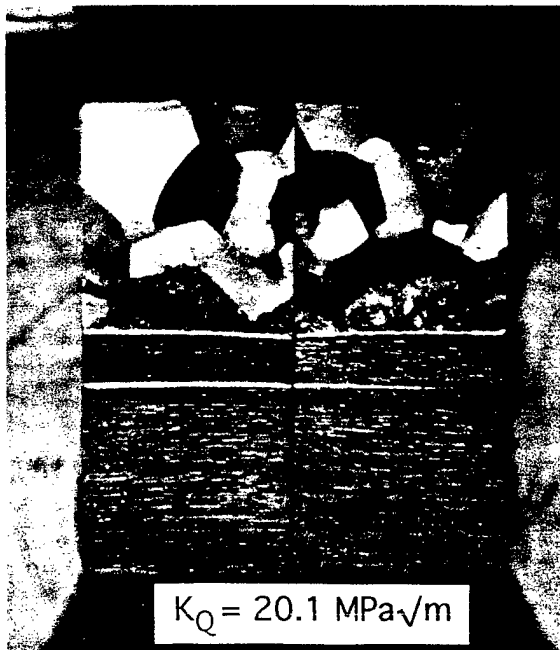
Fig. 10(a) Fracture surfaces of 3-point bend specimens of 93-016 showing the lack of correlation between K_Q values and overall fracture surface appearance.
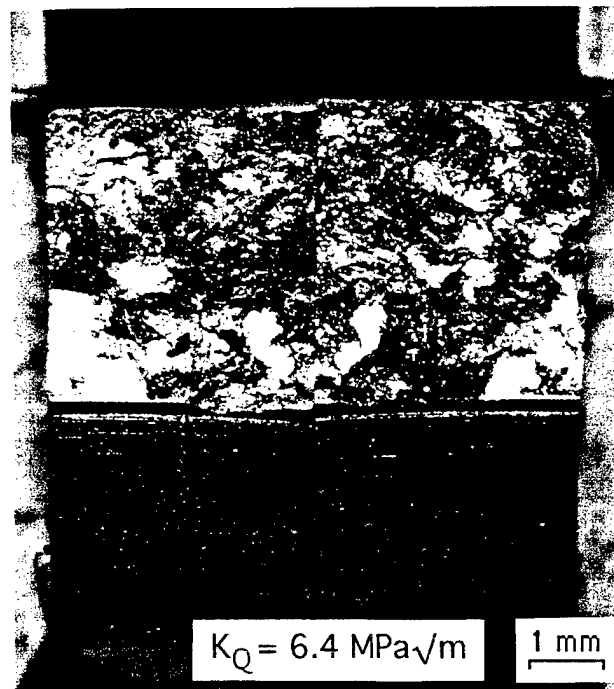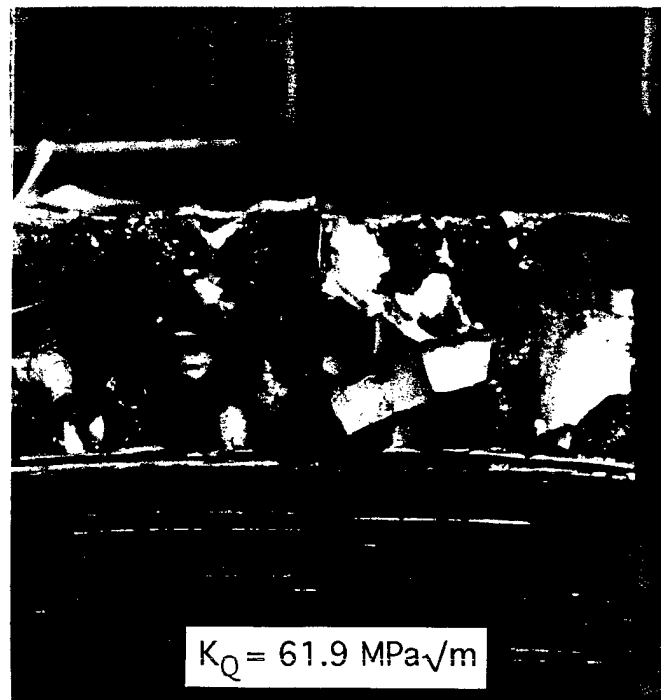
Fig. 10(b) Fracture surfaces of 3-point bend specimens with a K_Q difference of
approximately ten times showing the lack of correlation between fracture
surface appearance and measured fracture toughness.

All the fractures shown in **Figure 10(a)** are for the composite 93-016. The specimen with the most extensive intergranular fracture, upper left, had the highest value of K_Q, while the specimen with mixed trans- and intergranular fracture had the lowest. Closer examination indicates that for the highest toughness specimens fracture began transgranularly, while for the lowest K_Q, fracture started intergranularly. The differences in the fracture surfaces of **Figure 10(b)** are particularly striking. The mostly intergranular and "cleavage" fracture shown in the upper photograph had a K_Q approximately 10X that of the transgranular appearing fracture shown in the lower photograph.

4.   Nb-Si Alloys: Binary alloys, or *in situ* composites, from the Nb-Si system have been studied in work performed mainly at Wright Patterson Air Force Base (WPAFB) [9,10] similar to those of the Nb-Cr system. The materials that resulted were *in situ* composites containing Nb_5Si_3. A variety of cast and thermomechanically treated alloys including the composition Nb-10 at.% Si were examined. The highest toughness version was cast composite material that had been extruded at 1426°C at a ratio of 4.5:1 followed by heat treatment at 1500°C for 100 hrs.; oxygen contamination of the alloys was minimized during all operations.

Two pieces of Nb-10Si extrusion were obtained from Dr. Mendiratta. The first was heat treated at 1500°C for 100 hours in flowing argon, but the ceramic tube in which this was done at SwRI cracked after ≈ 90 hours, thus allowing oxygen contamination to occur. To test the effect of oxygen content on fracture toughness, eight 3-point notched specimens were cut from the extrusion by EDM and fracture toughness was measured. The average K_Q value measured by crack growth across the extrusion direction, was 22.3 MPa$\sqrt{m}$, with a variation of 13%, for an oxygen difference of 2.6 times (from 0.55 to 1.38 at.%). There was a weak correlation between K_Q and at.% O: $K_Q = 23.3 - 0.7(\text{at.\% O})$.

A second piece of Nb-10Si extrusion was obtained and machined into CT specimen blanks approximately 25 mm square by 2.5 mm thick so that the direction of crack growth would be across the extrusion direction. The material was then returned to WPAFB where it was held at 1500°C for 100 hrs. in order to convert the intermetallic. Machining of these CT specimens was then completed at SwRI followed by fatigue and fracture toughness testing.

Microstructure of the extruded and heat treated Nb-10Si is shown in **Figure 11.** This composite consisted of long thin fiber-like pieces of primary Nb solid solution 100 to 500 μm long and 15 to 20 μm in diameter, having a volume fraction of 0.485 [9]. Secondary Nb particles about 1.3 μm in diameter, volume fraction 0.274, were distributed within regions of Nb_5Si_3 with a volume fraction of 0.241 [9]. However, an alternative description of this microstructure would
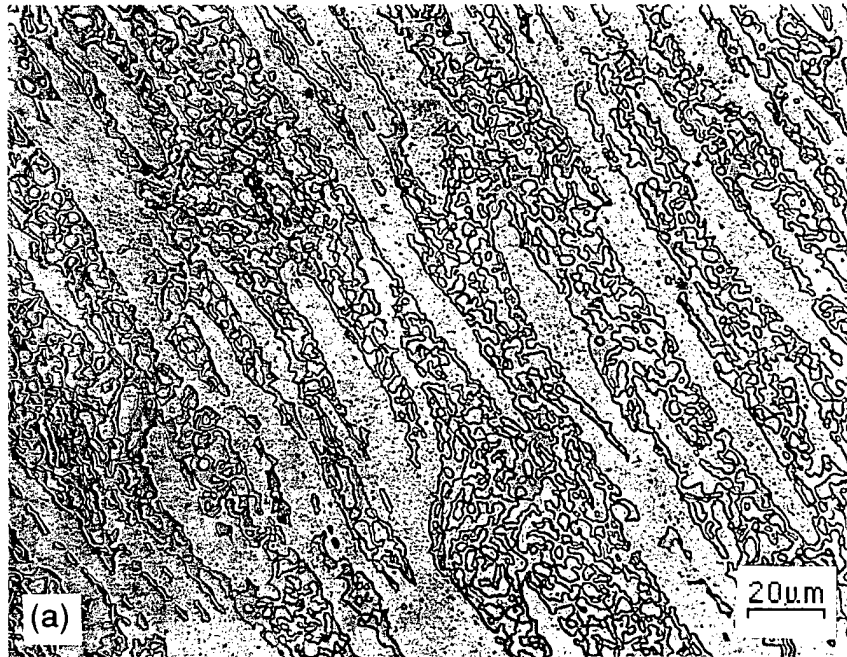
Fig. 11 Microstructure of the extruded and heat treated Nb-10Si composite.
(a) optical micrograph showing primary Nb (the lighter phase) and secondary Nb (lighter phase within the darker Nb_5Si_3 phase).

(b) SEM secondary electron micrograph showing fatigue crack path through the composite. Ion etching has revealed the large recrystallized grains of primary Nb.

20

include the secondary Nb with the intermetallic because of the fine dispersion of the secondary Nb particles; thus, the volume fraction of intermetallic (with dispersed secondary Nb) would be about 50%, with the primary Nb (ss) the remainder.

Analysis of the crack path shown in **Figure 11** indicates that the crack can traverse a much smaller area of intermetallic than indicated by the measured volume fraction. The crack path shown is approximately 237 μm long, but only about 51 μm is through intermetallic (with secondary Nb particles); thus, the crack experienced intermetallic only along about 21% of its path. Analyses of other possible crack paths approximately perpendicular to the extrusion direction shows that the intermetallic could have occupied as much as 35% of the path. These observations indicate that the effect of the intermetallic phase on fracture may be smaller than indicated by measured volume fraction.

The effect of intermetallic volume fraction on fracture toughness, as determined by Nekkanti and Dimiduk [10], is shown in **Figure 12**; also shown is the effect of extrusion and heat treatment. The measured toughness values lie below the ROM line, as also found for the Nb-Cr-Ti alloys. The K_Q values for the extruded and heat treated material lie considerably above those of the other composites and are closer to the ROM estimate. The results to be explained here are the low toughness of the hot pressed and heat treated composites, and the high toughness of the extruded composite relative to the ROM. The reason for the increase in toughness due to extrusion and heat treatment has been shown to be the increased ductility of the primary niobium caused by recrystallization [10]. If the effective volume fraction of intermetallic is less than measured from the microstructure, according to the argument given above, then the extruded and heat treated material K_Q values are approximately those expected from the ROM estimate, as shown by the rectangle in **Figure 12**.

Fractography of a 3-point bend specimens of this composite is shown in **Figure 13**, which should be compared to **Figure 10**. The macroscopic appearance of the fractures is different than those from the cast Nb-Cr-Ti composites, as might be expected from the microstructures, even though the fracture toughness is approximately the same.

5.   Comparison of Alloy Properties: For the three composites and one solid solution alloy whose fracture characteristics were determined in detail, microstructure was characterized and some mechanical properties were determined. Matrix strength in each material was estimated from microhardness indentations. The Cr_2Nb cracked when indented, thereby allowing an estimate of the K_Q of this phase in each composite. As seen in **Table 1**, the strength
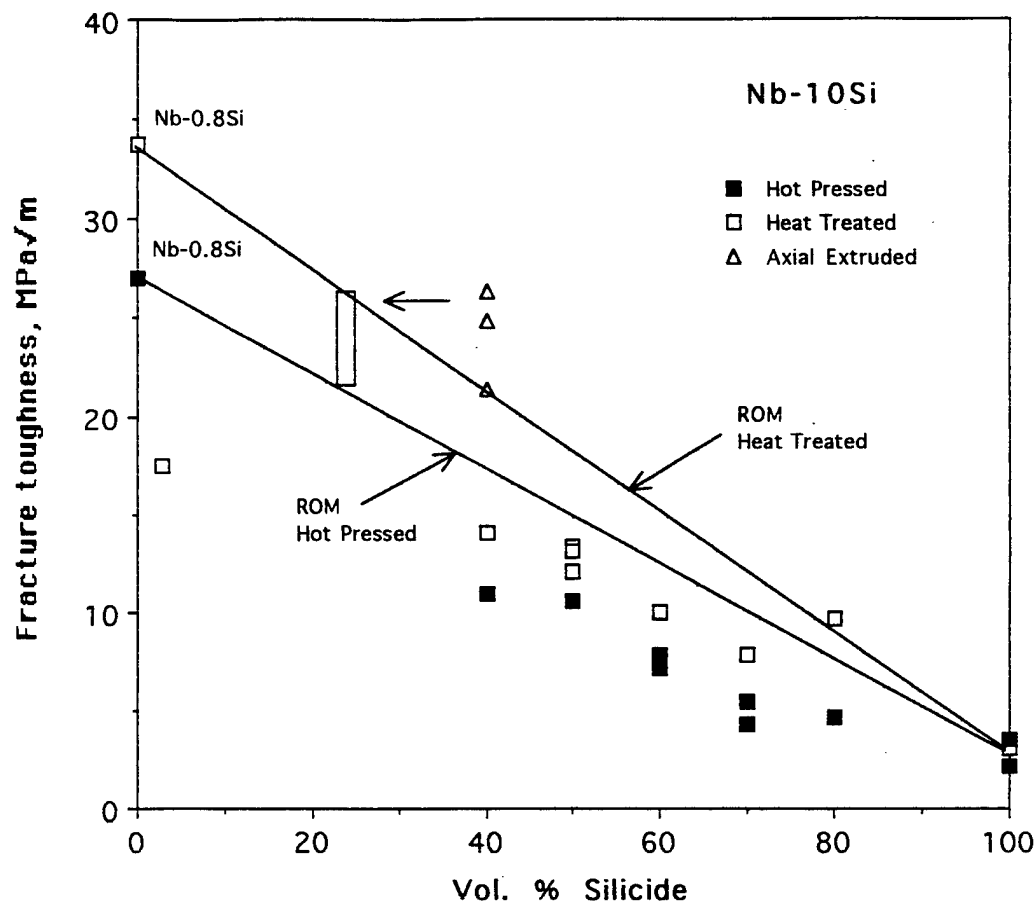
Fig. 12. Fracture toughness of Nb-10Si showing the effect of
volume fraction of Nb_5Si_3. Hot pressed and heat treated materials
are below ROM values, but the K_Q values measured perpendicular
to the extrusion axis are much closer to ROM values. The
rectangular box indicates where the toughness values of the
extruded composite would be plotted if only primary Nb is
considered as affecting the fracture process.
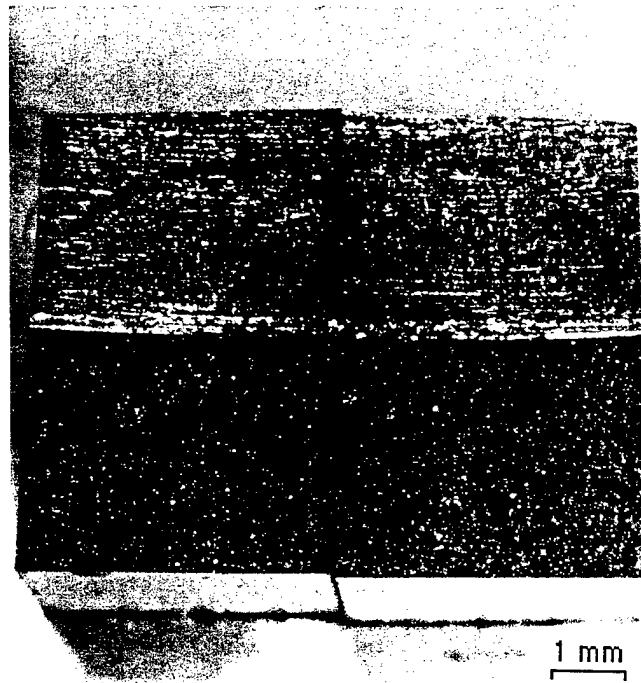
Fig. 13   Fractography of a 3-point bend specimen of extruded and heat treated
Nb-10Si composite. Compare with Fig. 10.

Table 1
Vickers Hardness (Kg/mm^2)
and Derived Cr_2Nb Toughness

Alloy Desig.	Composition Nb-Cr-Ti	vol.% Cr_2Nb	Matrix Hardness 50 gm	Matrix Hardness 100 g	Matrix Yield (MPa)	K_Q of Cr_2Nb (MPa$\sqrt{m}$)
93-007	59-33-08	43	510		1224	
93-008	62-34-04	45	475		1140	
93-009	83-08-09	0	245		588	
93-010	75-08-17	0	255		612	
93-015F	37-36-27	38		514	1234	1.40
93-016	42-29-29	22		540	1300	1.22
93-017	42-18-40	0		410	984	—
93-018	50-13-37	0	335	343	820	—
93-027	39-40-21	50	436	482	1080	1.53
Cr_2Nb	GE-1 (41-2)	100				1.3-1.5
	GE-2 (41-1)	100				1.2-1.3
	GE-3 (40)	100				1.46
	Ave. GE spec.					1.37±0.19
Nb-10Si		28*	161**		386	1.-2

* Intermetallic is Nb_5Si_3

** 10 g load (from Mendiratta, et al., Met. Trans., 1991, p. 1573).

Notes: 25 g loads did not crack the Cr_2Nb. GE Cr_2Nb specimens were directionally solidified.

of the matrix was higher in each of the Nb-Cr-Ti composites by a factor of 1.2 to 1.6 over that of the homogeneous "matrix" alloy (93-018). It may be that matrix deformation was constrained by the presence of the intermetallic, which caused the hardness to be increased. Apparently, toughness of the Cr_2Nb was not changed by additions of titanium. Although there were differences between individual hardness measurements for the various composites, the scatter was large so no identifiable difference was found.

Measured microstructural parameters of these materials are reported in **Table 2**, which also lists matrix yield strain. Modulus was computed from the rule of mixtures for the composites and yield stress was derived from hardness indentation. Measured lattice parameters are reported in **Table 3** together with values computed using the rule of mixtures. Changes in lattice parameter between the solid solution alloy 93-018 and the matrix alloy of the composites are about 2%. Thus, it appears that the matrix alloy should be representative of the matrices in the composites, but changes in hardness between the matrix alloy and the matrices of the composites don't seem to support this conclusion unless the differences are due to deformation constraint caused by the intermetallic. Detailed work on composition and microstructure of the composite matrices are probably required to fully understand the nature of the composite matrices.

A summary of K_Q values measured for these materials using 3-point bend specimens is listed in **Table 4**. There is an apparent insensitivity of fracture toughness to volume fraction of Cr_2Nb, which, so far, has not been explained.

C. Summary

Alloying Effects: Alloying the Nb-Cr composites with Ti resulted in the desired increase in fracture toughness, but also had the unexpected very large increase in toughness at about 37 at.% Ti for the matrix alloy to $K_Q \approx 62$ MPa$\sqrt{m}$. This large increase in toughness can be attributed to the ductility and strength of the alloy, but has not been explained on the basis of alloy theory. The increased matrix alloy toughness also increased composite toughness from about 5 to 18 MPa$\sqrt{m}$. The use of notched, 3-point beam specimen tests to measure K_Q to determine the effects of alloying proved to be very effective.

Table 2
Alloy Properties and Characteristics

Alloy Desig.	vol.% Cr_2Nb	—Matrix Properties—		Composite		Particle Diameter (μm)	Spacing (note 1) (μm)
		Modulus (GPa)	Yield Stress (MPa)	Yield Strain	Modulus (GPa)		
Cr_2Nb	100	216	9900	4.6×10^{-2}	—	—	—
93-015F	38	123	1234	7.7×10^{-3}	160.(2)	27	19.2
93-016	22	124	1296	8.7×10^{-3}	149.(2)	10	11.5
93-018	0	125	816	6.5×10^{-3}	125	—	—
	Nb_5Si_3						
Nb-10Si	28	105	386	3.7×10^{-3}	193.(3)	(4)	—

(1) Mean planer surface-to-surface separation of spherical particles [11].

(2) E of $Cr_2Nb \approx 220$ GPa.

(3) E of $Nb_5Si_3 \approx 327$ GPa.

(4) Mendiratta, et al. (Met. Trans., 1991, p. 1573) report the size of the primary and secondary niobium (ss) rather than the size of the Nb_5Si_3 because of the microstructural morphology.

Table 3
Lattice Parameters

Material Designation	Composition Nb %	Composition Cr %	Composition Ti %	Cr$_2$Nb %	Lattice Parameter matrix Å	Lattice Parameter Cr$_2$Nb Å	ROM calc. matrix Å
Niobium	100			0	3.301	—	—
93-018	50	13	37	0	3.228	—	3.257
93-016	29	29	42	22	3.303	7.002	3.192
93-015F	37	36	27	38	3.201	6.996	3.159

Table 4
Summary of Fracture Toughness Values
3-Point Bend Specimens

Material Designation	% Intermetallic	Measured Fracture Toughness K_Q MPa$\sqrt{m}$
93-018	0	61.7 ± 1
93-016	22	16.0 ± 1
93-015F	38	18.5 ± 1.5
Nb-10Si	28	21.4
		24.8 ± 2

II. DETAILED FATIGUE CRACK GROWTH AND FRACTURE TOUGHNESS CHARACTERIZATION OF SELECTED ALLOY COMPOSITIONS

A. Introduction

It was only feasible to perform detailed fatigue crack growth characterization of the toughest materials because the slope of the da/dN-ΔK curve was so steep for the brittle materials that meaningful information was not obtained. For example, fatigue cracks were grown in materials 90-014 (composition 65 Nb 35 Cr, 46% Cr_2Nb) and 90-015 (composition 71 Nb 29 Cr, 36% Cr_2Nb) and the slopes were measured as 20 and 64, respectively; see **Figure 2**. The thresholds for fatigue crack growth (R = 0.1) were 3.6 and 4.1 MPa$\sqrt{m}$, and $K_Q \approx 7.2$ and 5.3 MPa$\sqrt{m}$. The spread between threshold and fast fracture was, therefore, between 1.2 and 4 MPa$\sqrt{m}$. Data commensurate with the goals of this research could not be obtained from materials demonstrating this level of brittle fracture.

The materials that were evaluated in considerable detail were:

(1)   the toughest single phase material (93-018, $K_Q \approx 62$ MPa$\sqrt{m}$);

(2)   a forged and heat treated alloy (93-016F) with $\approx 22\%$ Cr_2Nb on the tie line of the tertiary phase diagram with 93-018;

(3)   a similarly forged and heat treated composite (93-015F) with $\approx 38\%$ Cr_2Nb, on approximately the same tie line as 93-018 and 93-016F; and

(4)   a Nb-10Si composite that had been forged and heat treated, with $\approx 50\%$ Nb_5Si_3. The Nb-10Si composite was obtained from the Materials Laboratory at Wright-Patterson AFB.

The hypothesis was that by testing composites having different volume fractions of Cr_2Nb, together with a single phase alloy with nominally the same composition as the matrix of the composites, it should be possible to determine the effect of volume fraction of intermetallic. These tests were made with the additional hypothesis that the intermetallic particles constrained, or restrained, flow in the matrix of the two phase alloys, and that resulted in the reduced toughness and the increased rates of fatigue crack growth compared to the homogeneous matrix alloy.

These composite materials are similar in some ways to the aluminum matrix composites reinforced with alumina or silicon carbide in that both composites are composed of nominally ductile matrices having nondeformable reinforcements. Research on the aluminum composites has shown that they have poor fracture toughness when compared to the matrix alloys, and there has been much speculation as to why and what would be required to increase toughness. It appears, after much research, as though the lack of toughness is intrinsic, i.e., the presence of the particles, regardless of size and with the best of distributions, causes a decrease in toughness, and microstructural manipulation cannot substantially increase toughness. However, there has been little systematic study of those composites, so there is still much to be learned from them that is applicable to the composites of interest in this research.

B.   Microstructural Characterization of Specimens Tested

Microstructure is often somewhat less than homogeneous for experimental materials; therefore, the specific specimens used for experiments were characterized. This section details those results.

1.   Nb-Cr-Ti Matrix Alloy (93-018): Fracture toughness $K_Q \approx 62$ MPa$\sqrt{m}$. The composition of this alloy was 50 Nb 13 Cr 37 Ti, and it was homogeneous and contained no intermetallic. The average grain size was 1.75 mm in diameter and the Vickers hardness was ≈ 340 kg/mm^2 when measured with 50, 100 and 200 g loads, which is equivalent to a flow stress of ≈ 820 MPa (see **Table 1**). Lattice parameter was measured as 3.228 Å which is smaller than that of niobium (3.301 Å).

The fatigue crack was grown from a notch through two large grains on the side of the specimen from which crack growth data, crack opening displacement, and strain analyses were derived. All the crack tip analyses were obtained when the crack tip was in one grain. This grain was so large (approximately 3.5 mm in diameter) that a Laue back reflection diffraction pattern was obtained and oriented. Analysis indicated that the normal to the specimen surface was within 5° of a <112> and that loading was in approximately the <110>. Thus, the crack growth direction was approximately <111> probably on the {110} when detailed crack tip analyses were made.

2.   Nb-Cr-Ti Composite (94-016): Highest fracture toughness from bend bar tests $K_Q = 16$ MPa$\sqrt{m}$. The microstructure of this composite, shown in **Figure 9**, consisted of many Cr$_2$Nb particles that were not spherical. Measured volume fraction ($\approx 17\%$) was not as large as

determined from the phase diagram (32%), which indicates an error in either the phase volume measurement or the phase diagram. As determined from the microstructure, forging and heat treatment caused precipitation of about 15% of the total Cr_2Nb in the grain boundaries.

Particle size and spacing were measured using the line intercept method and are listed in **Table 2**. An "equivalent particle diameter" of ≈ 5 µm was determined from volume fraction and particle-line intercepts [10]. Since the microstructure consists mostly of elongated particles, this value is rather fictitious. From the particle diameter, the "mean planer surface-to-surface distance" was computed as 11.5 µm.

The matrix hardness and the toughness of the Cr_2Nb are listed in **Table 1**. The indicated matrix strength was ≈ 1300 MPa, which is $\approx 60\%$ stronger than that of the matrix specimen 93-018. Lattice parameter measurement for the matrix equals 3.303 Å, which is larger than that of 93-018, the matrix specimen; lattice parameter of $Cr_2Nb = 7.002$ Å (see **Table 3**).

The fatigue specimen broke through the grain boundary Cr_2Nb, while the fracture toughness bend specimens broke only partially through the grain boundaries. The fatigue specimen broke unexpectedly at $K_Q \approx 8$ MPa$\sqrt{m}$, which is a much lower value of toughness than derived from the 3-point bend specimens. The reason for this premature failure was related to the path of the fatigue crack through the microstructure. Starting from the notch, the crack path was transgranular until the first grain boundary containing a continuous film of Cr_2Nb was encountered. From that point to fracture, growth was in grain boundary Cr_2Nb; thus, the low value of derived toughness. Fractography of the 3-point bend specimens indicated, for the highest toughness value measured, that the crack growth began as transgranular and then switched to intergranular; thus, a higher initiation toughness was measured.

3. Nb-Cr-Ti Composite (93-015F): Fracture toughness $K_Q \approx 18.5$ MPa$\sqrt{m}$. The microstructure of this material consisted of approximately 38% dispersed, approximately spherical particles of Cr_2Nb on average 27 µm in diameter. From these parameters, the mean planer surface-to-surface separation was computed to be 19.2 µm. This value is much more realistic than for the previous composite 93-016 because the particles approximated spheres. Matrix yield estimate, as estimated from Vicker's hardness was ≈ 1234 MPa — see **Table 1**. Backscattered electron imaging and etching showed that the Cr_2Nb particles were not single crystals; straight boundaries between differently oriented parts of the phase gave the appearance of twinning. Lattice parameter measurement, **Table 3**, for the matrix equals 3.201 Å, which was somewhat smaller than that of the matrix specimen (3.228 Å), and that of the $Cr_2Nb = 6.996$ Å.

4. Nb-10Si Composite: The material tested was extruded and heat treated and had an indicated $K_Q \approx 23$ MPa$\sqrt{m}$. The microstructure of this material, shown in **Figure 11**, consisted mainly of fibers of recrystallized primary Nb "fibers" within a matrix of Nb_3Si_5 with fine precipitates of secondary Nb. The size of the intermetallic was too small to determine K_Q using a Vicker's indenter. Strength of the recrystallized primary Nb fibers was ≈ 386 MPa, which is only about one-forth the strength determined for the Nb-Cr-Ti matrix composites.

As discussed in a previous section, determination of the effective volume fraction of intermetallic is not so easy. The crack path estimate for intermetallic was 25 to 35%, whereas a value of closer to 50% is derived from microstructural analysis. The fiber-like morphology of the primary Nb(ss) is completely different than that of the matrix in the Nb-Cr- Ti alloys; thus, it is difficult to compare the microstructures of these two classes of composites using the same characterizing parameters. The surface-to-surface particle spacing has no meaning for this composite.

C. Crack Growth Rate Characterization

The growth rate of fatigue cracks through the Nb-Cr-Ti matrix alloy and two composites were obtained, although much less data was obtained on one composite than planned due to fracture at an unexpectedly low stress. Also, fatigue crack growth data were obtained for the Nb-10Si.

For the low toughness composites, crack growth was initiated at the notch with the specimen under compression-compression loading. After cracks were formed on at least one side of the specimen, the R ratio was shifted from -10 to +0.1 in several steps. Because bcc niobium is strain rate sensitive, the cyclic rate used for loading was decreased to 1 Hz, except for the high toughness matrix alloy, a rate of 5 Hz was used. The goal of this procedure was to obtain fatigue crack growth data at R = 0.1, but for the 22% Cr_2Nb composite 93-016, due to premature fracture, data were obtained only at negative R ratios. Several problems encountered in measuring fatigue crack growth from brittle materials are (1) that the crack is rarely the same length on both sides of the specimen, and (2) at low growth rates, the crack usually does not grow during each increment of cycling; in fact, the crack may not grow for exceedingly long periods and then grow a large increment. These problems were acute during the crack growth experiments with these materials and caused difficulty in determining values of ΔK and resulted in fewer crack growth data points than were expected.

For 93-018 matrix material, da/dN vs ΔK is shown in **Figure 14**. A few crack closure measurements were also made and are shown in **Figure 15**. From **Figure 14**, the data point at $\approx 2 \times 10^{-11}$ m/cy and the trend in data at higher rates gives an estimate of $\Delta K_{th} = 7$ MPa$\sqrt{m}$. From the crack closure data, $\Delta K = 5.8$ MPa$\sqrt{m}$. The two values are in reasonable agreement, but there are more crack growth data than closure data, so the higher value was used to calculate $\Delta K_{eff} = \Delta K - \Delta K_{th}$; this procedure for determining ΔK_{eff} has been shown for many materials as a proper way to account for fatigue crack closure. The resulting da/dN vs ΔK_{eff} curve is shown in **Figure 16**. In both **Figures 14** and **16**, crack growth rate data for unalloyed niobium is shown from the work of Fariabi, *et al.* [12]. Those data are in good agreement with the matrix alloy up to a growth rate of $\approx 10^{-8}$ m/cy, but the tougher matrix alloy results in a lower slope (4.8) at higher growth rates. For unalloyed niobium, crack growth rates at the lower values of ΔK_{eff} do not agree with those of the matrix alloy, but the data are few.

For 93-016 the cast 22% Cr_2Nb composite, da/dN vs ΔK is shown in **Figure 17** at negative R ratios only. The specimen broke as the transition to a positive R ratio was being made. The slopes of the curves are very high, indicative of very brittle behavior.

For 93-015F the forged 38% Cr_2Nb composite, da/dN vs ΔK is shown also in **Figure 17**, but at R = 0.1. Although the data are sparse and exhibit considerable scatter, the indications are that $\Delta K_{th} \approx 4$ MPa$\sqrt{m}$ is a reasonable estimate, and that the slope of the curve is much lower than for the other material 93-016.

For Nb-10Si extruded composite, da/dN vs ΔK at R = 0.1 is shown in **Figure 18**. The estimate of $\Delta K_{th} \approx 7.5$ MPa$\sqrt{m}$ is compatible with the data; da/dN - ΔK_{eff} is shown in **Figure 19**. The large scatter in data points comes from the reluctance of the crack to grow in a smooth and uniform manner, as discussed in the introduction to this section.

A comparison between the Nb-Cr-Ti (93-015F) and Nb-10Si composites is shown in **Figure 20**, together with associated ΔK_{th} values. The Nb-10Si composite is shown with the smaller of the estimates of intermetallic volume fraction because that is compatible with the higher value of ΔK_{th}.

D. Illustrations of Crack Tip Deformation

Detailed measurements of material response at the crack tip and crack opening displacement were performed on the matrix alloy 93-018 (12 analyses), 93-015F the 38% Cr_2Nb composite (11 analyses), 93-016 the 22% Cr_2Nb composite (2 analyses), and the Nb-10Si composite with
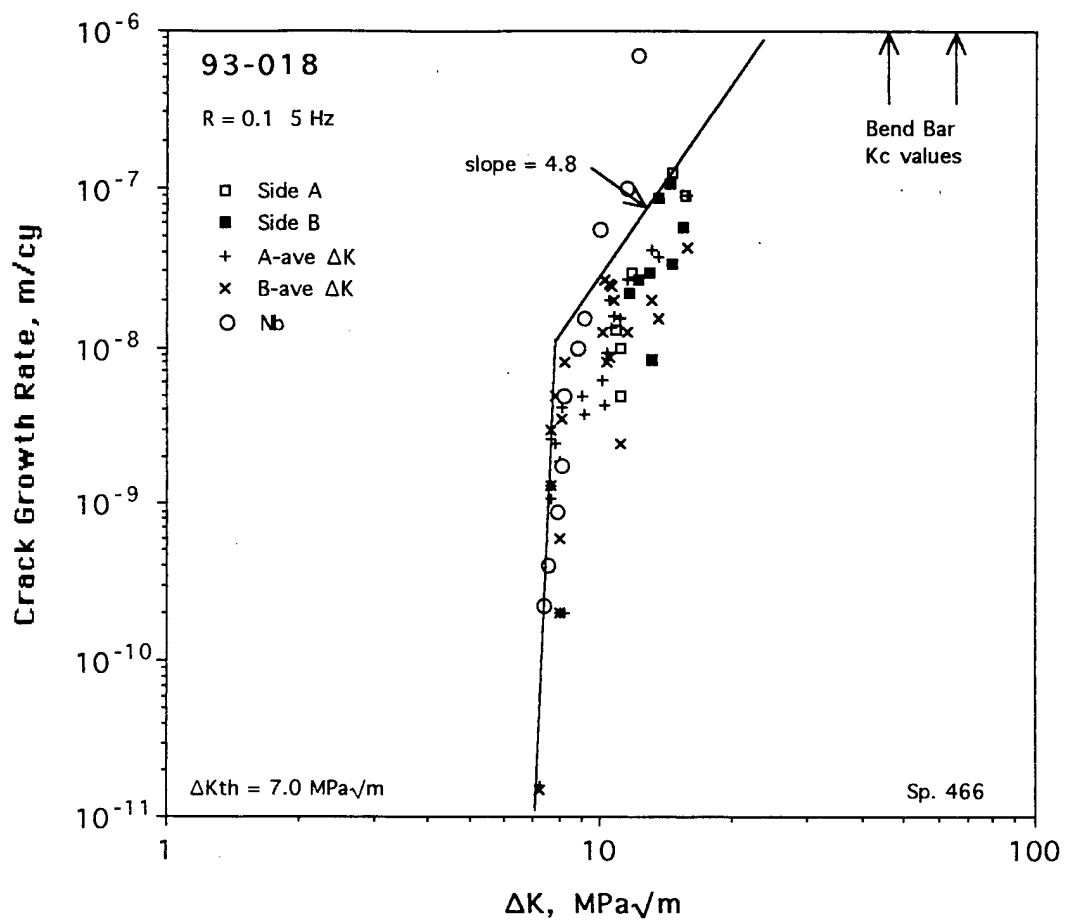
Fig. 14 Fatigue crack growth rates through the high toughness matrix Nb-Cr-Ti alloy 93-018. Shown for comparison are data for pure Nb from Fariabi, et al. [12].
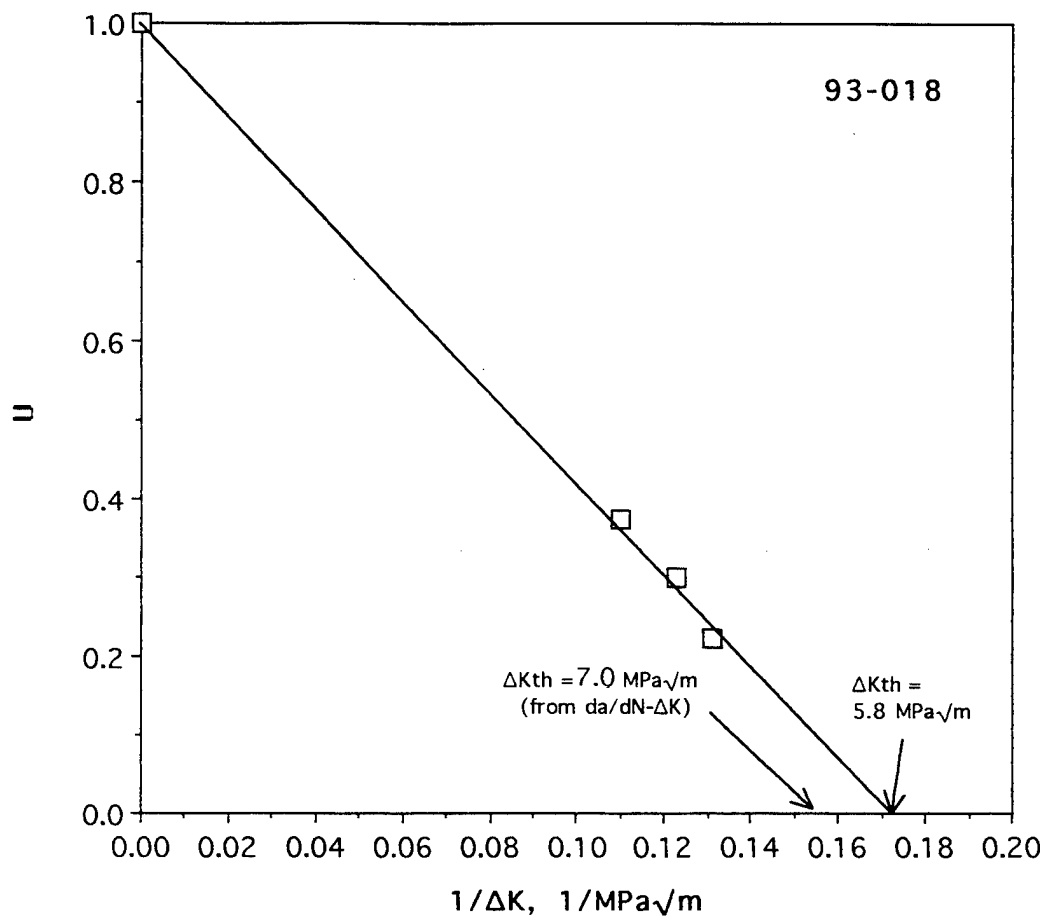
Fig. 15   Fatigue crack closure measurements made from the matrix alloy.
Closure measurements indicate $\Delta K_{th} \approx 5.8$ MPa√m while $\Delta K_{th} \approx 7.0$ MPa√m was estimated from the crack growth rate curve.
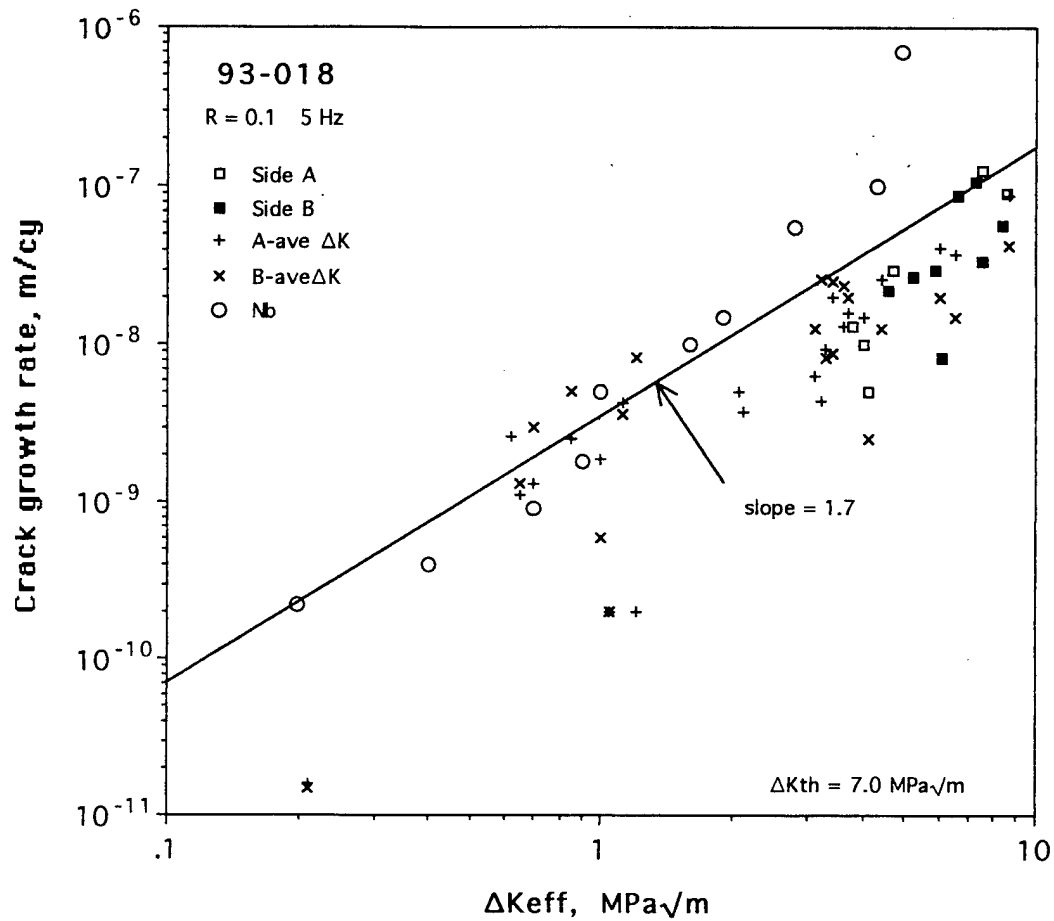
Fig. 16   Fatigue crack growth rate for 93-018 as a function of $\Delta K_{eff} = \Delta K - \Delta K_{th}$.
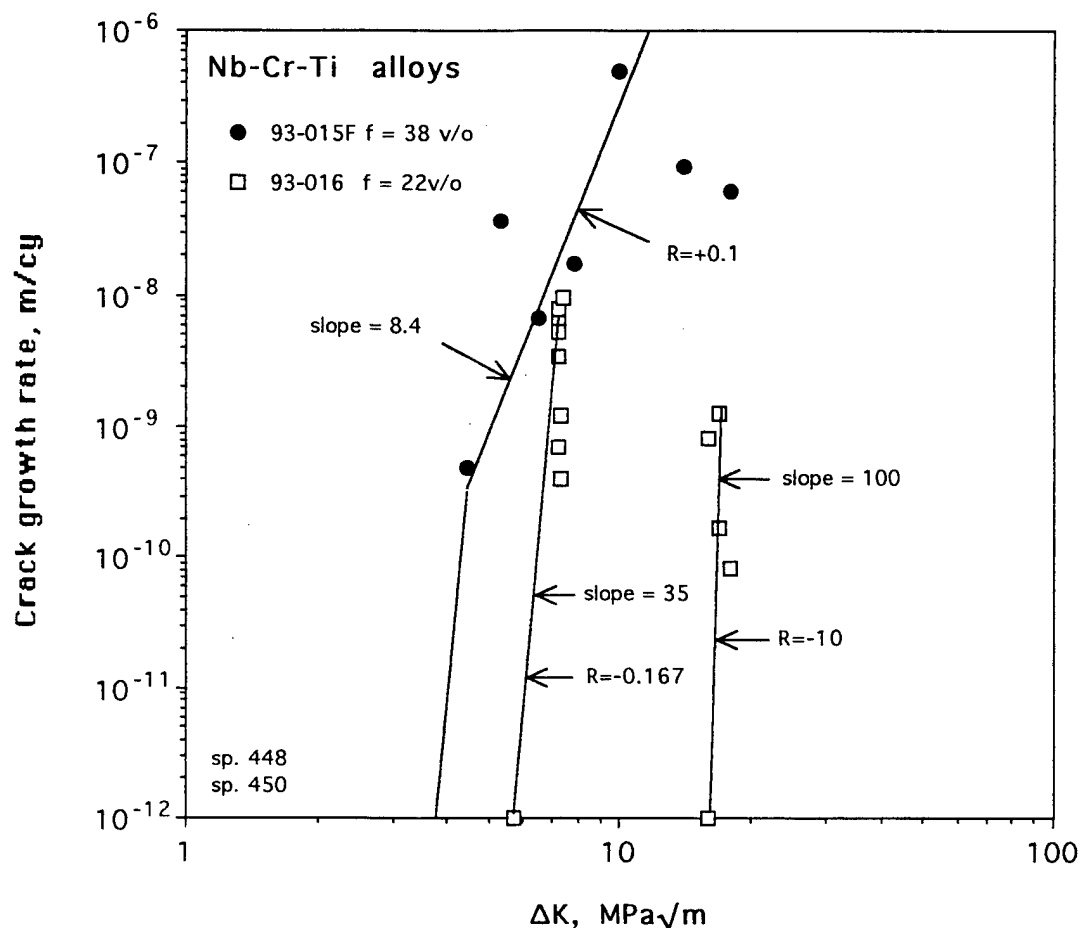
Fig. 17   Fatigue crack growth rate curves for the Nb-Cr-Ti composites 93-015F and 93-016 containing 38 and 22 vol. % Cr_2Nb respectively. Cracks were started from a notch using tension-compression loading and crack growth was very intermittant in both materials. The specimen of 93-016 broke before the transition to tension-tension loading could be made, thus only negative R-ratios are reported.
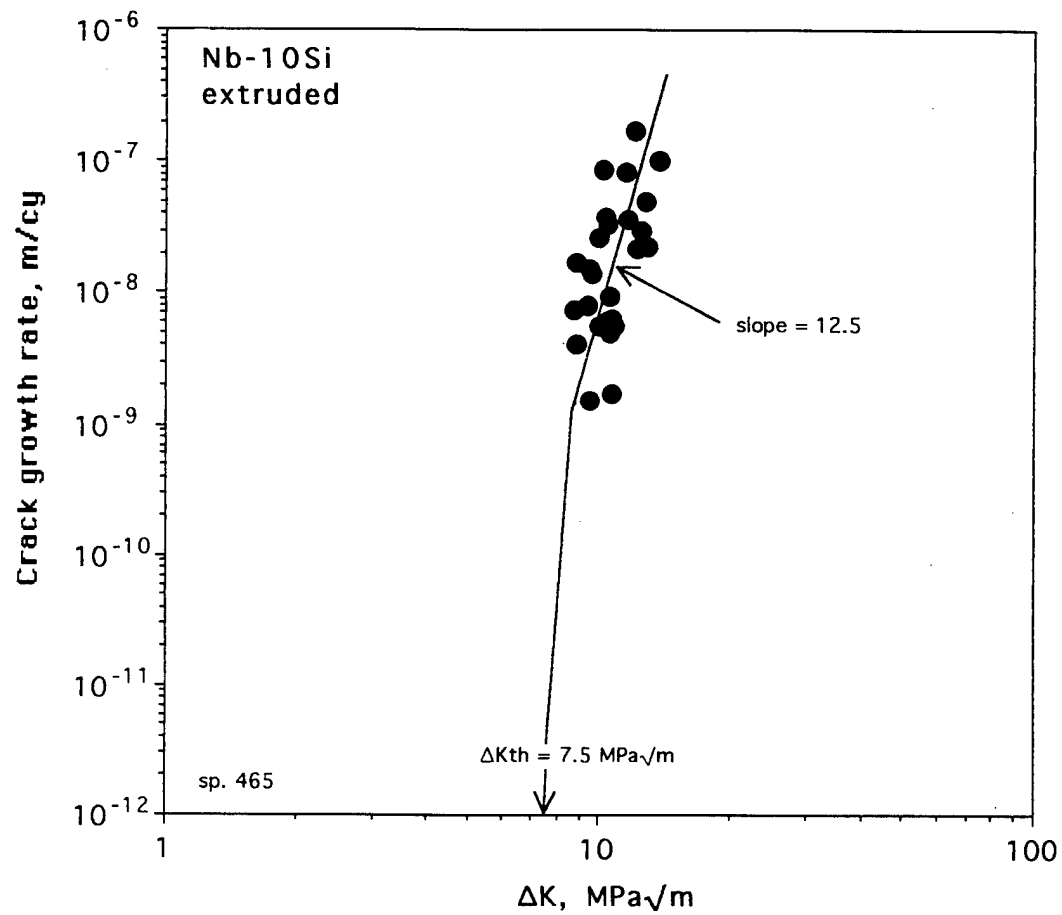
Fig. 18   Fatigue crack growth rate vs. ΔK for extruded and heat treated Nb-10Si.
Crack growth direction was perpendicular to the extrusion direction.
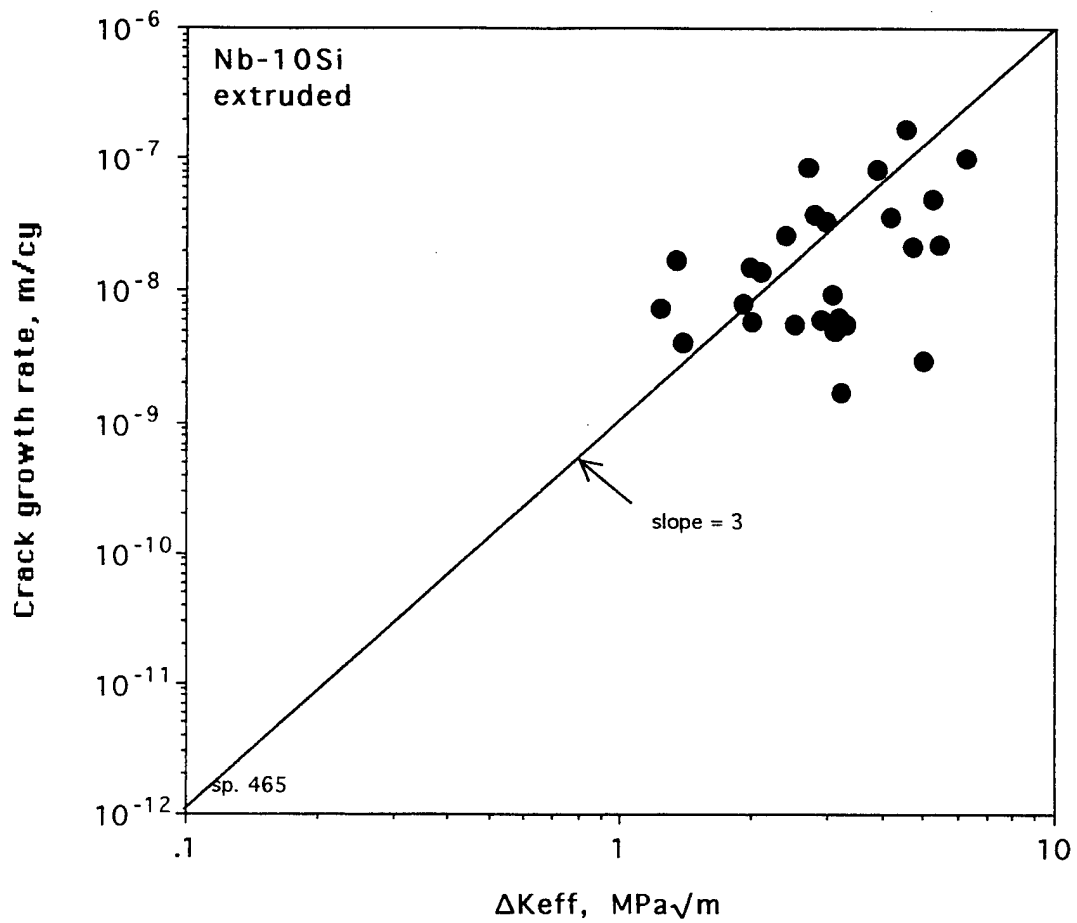
Fig. 19   Fatigue crack growth rate vs. $\Delta K_{eff} = \Delta K - \Delta K_{th}$ for extruded and heat treated Nb-10Si.
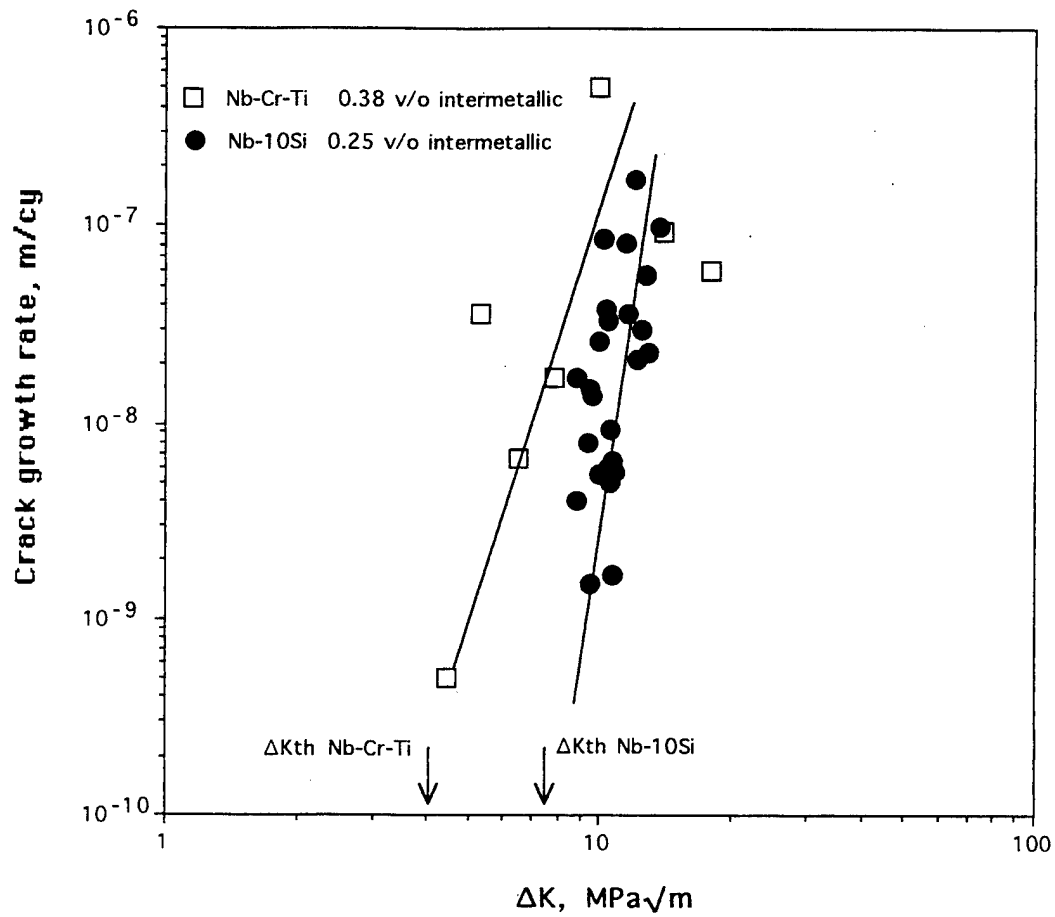
Fig. 20   Comparison between fatigue crack growth rates of the two Nb-based composites studied.

25% Nb$_5$Si$_3$ (7 analyses). In this section will be shown representative analyses of all materials but 93-016, but the results of all measurements are tabulated. In each illustration are shown (1) a photograph of the microstructure with an overlay of the measured displacements; the crack tip is indicated by a circle and the point of zero displacement by a square; (2) the crack opening displacement; and (3) the distribution of maximum shear strain. The location of the crack is drawn on the plane of zero strain in the strain distribution diagram. From the photograph and overlay, the location of reinforcement particles may be seen relative to the measured displacements. The crack opening displacement is shown as a function of the square root of distance behind the crack tip because many analyses have shown that COD is normally linear in $\sqrt{d}$. Maximum shear strain is represented because of its importance to crack growth.

For 93-018 single-phase matrix alloy, typical crack tip analyses are shown in **Figures 21** and **22**. These crack tip analyses are typical of cracks in many other monolithic alloys that have been studied, e.g., aluminum, titanium and steels. In **Figure 21**, COD = 0 at d = 0; thus, the crack tip is sharp. In contrast, COD = 0.5μm at d = 0 in **Figure 22**; thus, the crack tip is blunt in this illustration. Whether sharp or blunt, COD is linear in $\sqrt{d}$, as is typical for many monolithic alloys. The distribution of maximum shear strain ahead of the several crack tips is shown in **Figure 23**; the functional relationship shown is

$$\varepsilon' = \varepsilon(y)/\varepsilon(0) = A' - m' \ln(y + 1) \tag{1}$$

where $\varepsilon(y)$ equals strain at distance y ahead of the crack tip, and $\varepsilon(0)$ equals crack tip strain. A' and m' are empirically derived constants. The constant 1 was added to y so that the crack tip value might be shown also on the graph. This distribution is typical of aluminum and titanium alloys.

Analysis of six crack tips indicated that A' = 1 and m' = 0.304 ± 0.02 for this alloy. This compares to m' = 0.24 for aluminum alloys.

For 93-015F composite with 38% Cr$_2$Nb, typical crack tip analyses are shown in **Figures 24** and **25**. The distribution of maximum shear strain ahead of the crack tip is shown for several analyses in **Figure 26**.

The strain distribution shown in **Figure 24** is not typical for monolithic alloys, most of the strain is on the left side of the crack tip where there are fewer intermetallic particles. The crack was bridged well behind the tip (not seen in the photograph), as may be seen in the COD measurements. COD is not linear with $\sqrt{d}$ even in the region near the crack tip possibly because the crack wake is through a series of aligned, broken Cr$_2$Nb particles.

Fig. 21   Alloy 93-018. Photograph with displacment overlay, COD and distribution of maximum shear strain are shown at ΔK_{eff} = 3 MPa√m. Displacements were measured each 2 µm, and are shown 10 times actual.
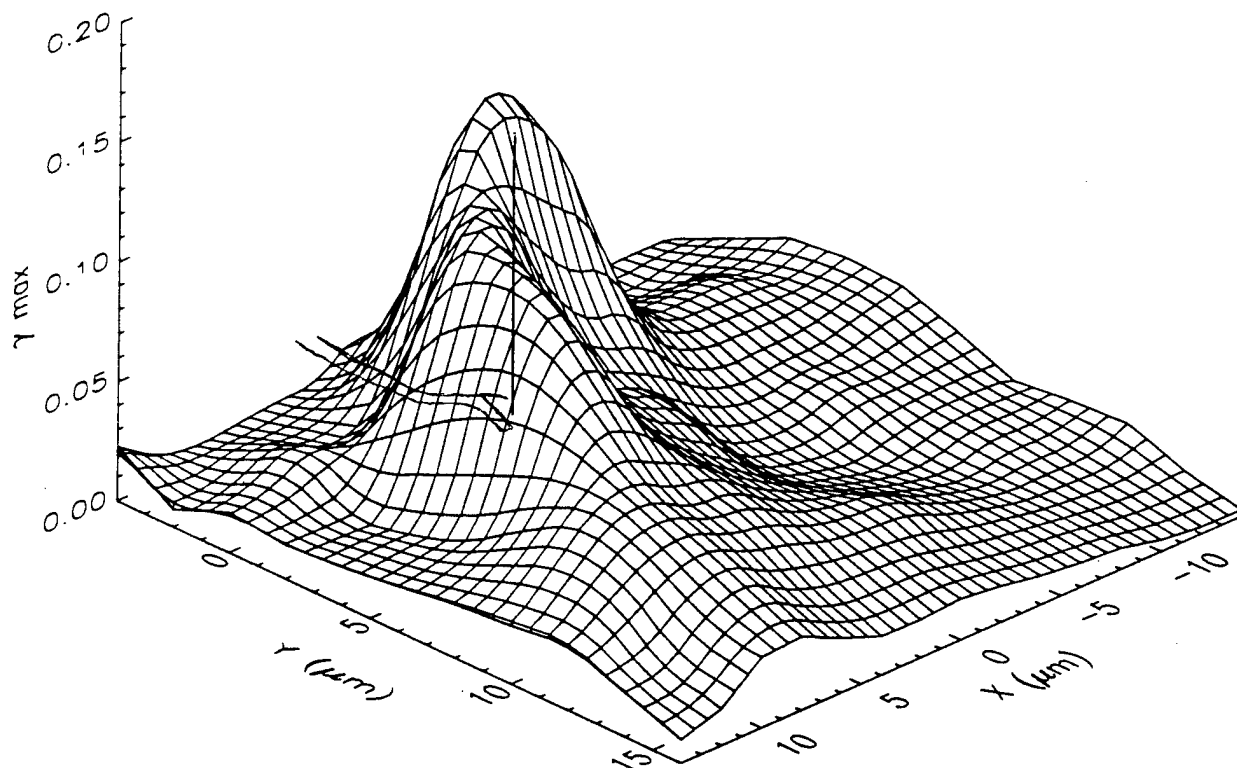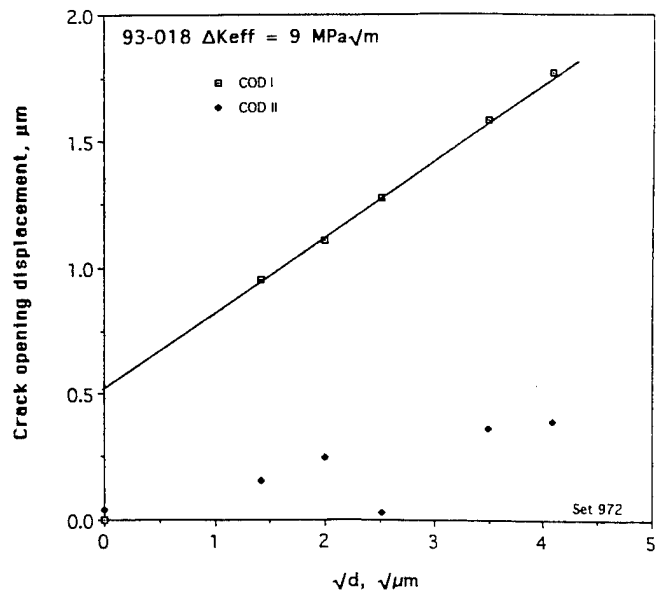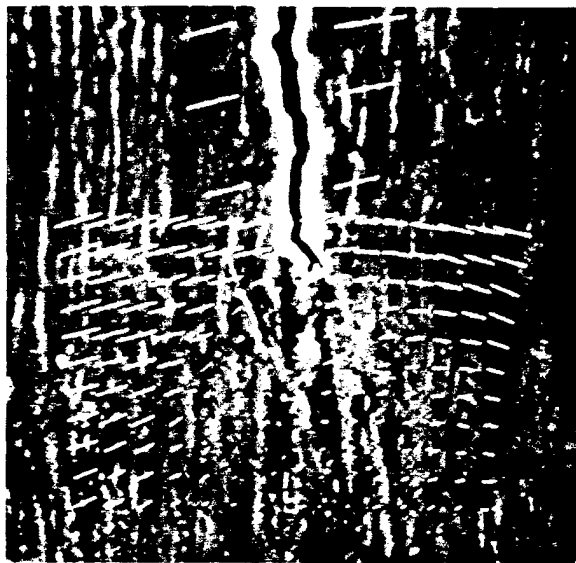
Fig. 22   Alloy 93-018. Photograph with displacment overlay, COD and
distribution of maximum shear strain are shown at ΔK_{eff} = 8 MPa√m.
Displacements were measured each 2 μm, and are shown 5 times actual.
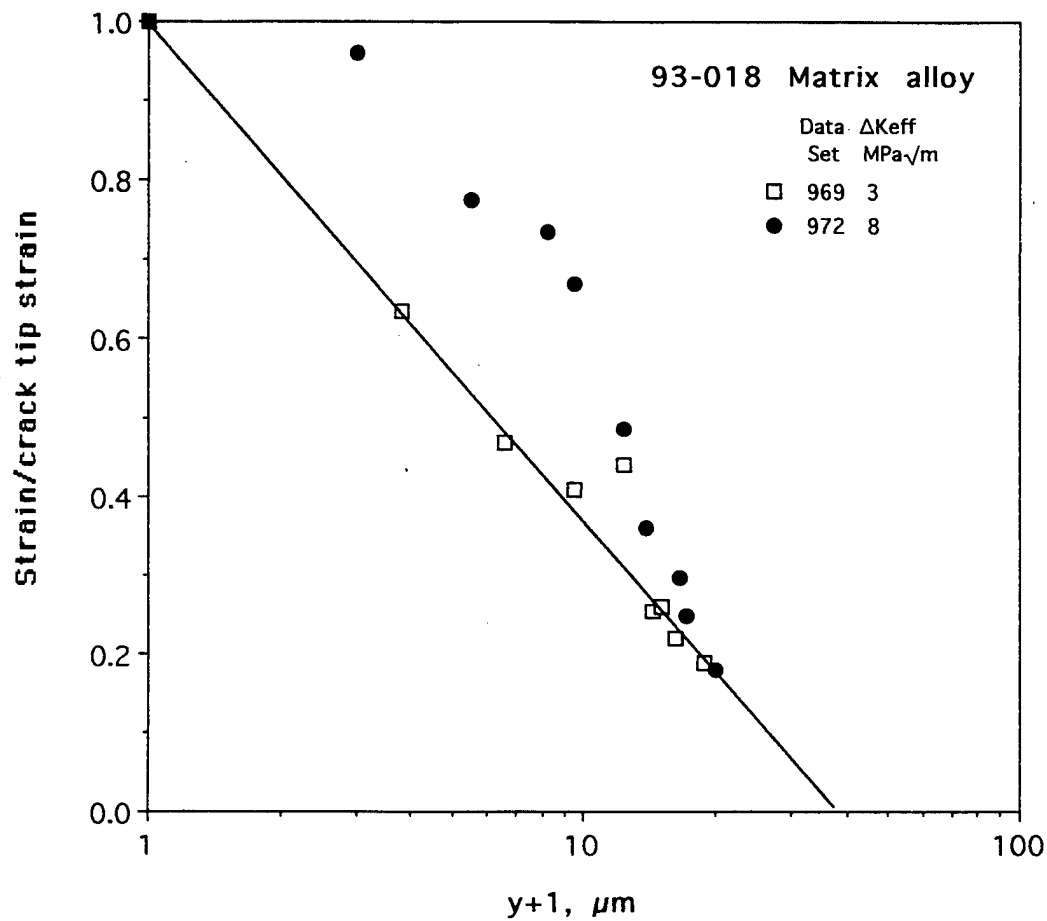
Fig. 23 Alloy 93-018. Distribution of maximum shear strain ahead of the crack tip normalized by crack tip strain for the two crack tips shown in Figs. 21 and 22. One μm has been added to distance so that the crack tip value may be shown.
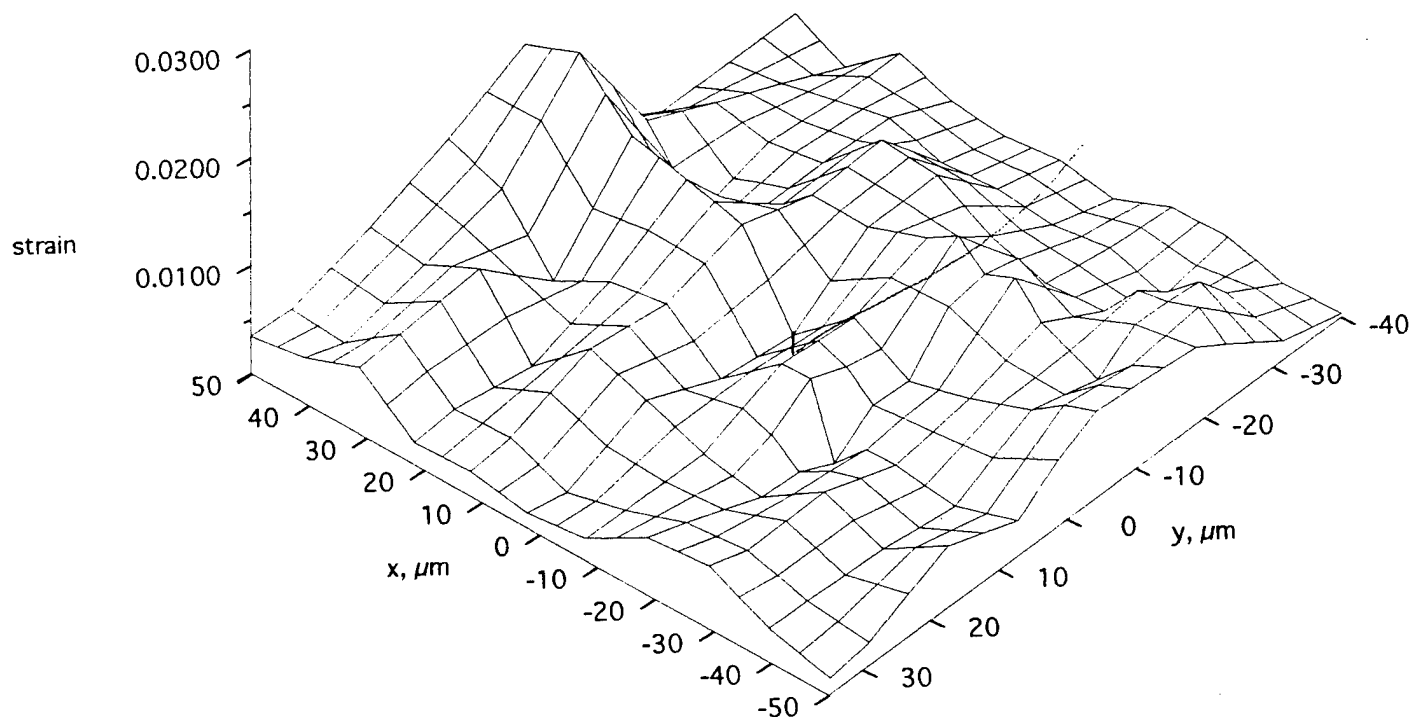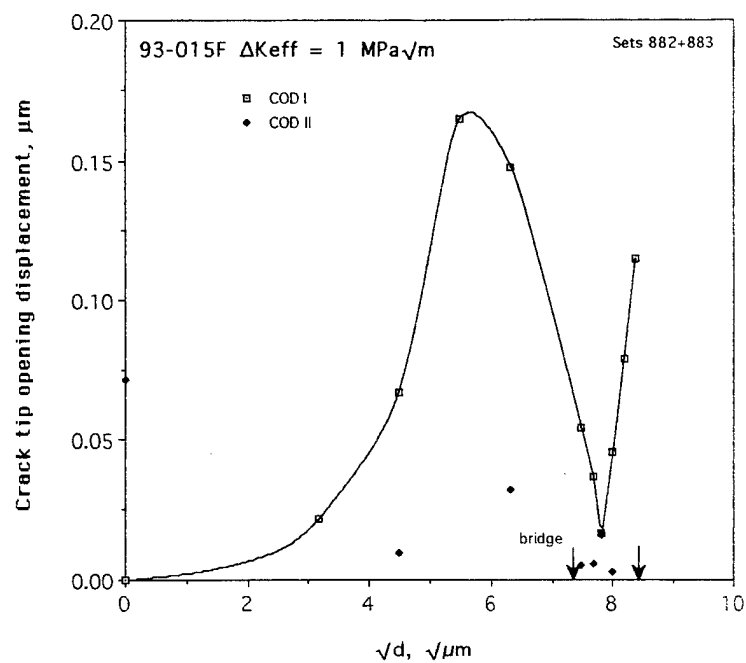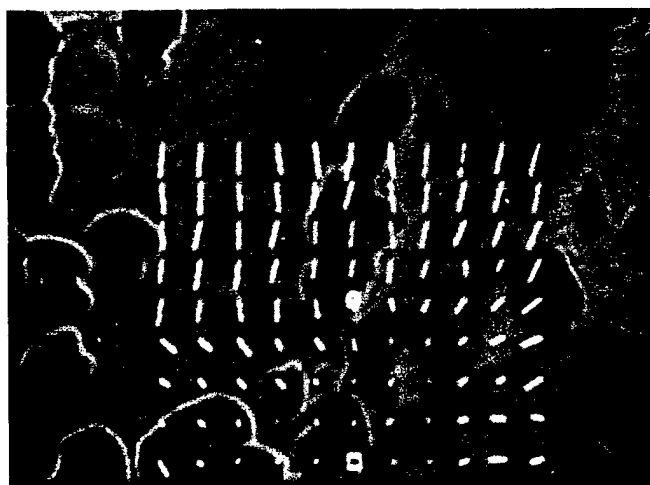
Fig. 24   Composite 93-015F. Photograph with displacment overlay, COD and distribution of maximum shear strain are shown at ΔK_{eff} = 1 MPa√m. Displacements were measured each 10 µm, and are shown 20 times actual.

44
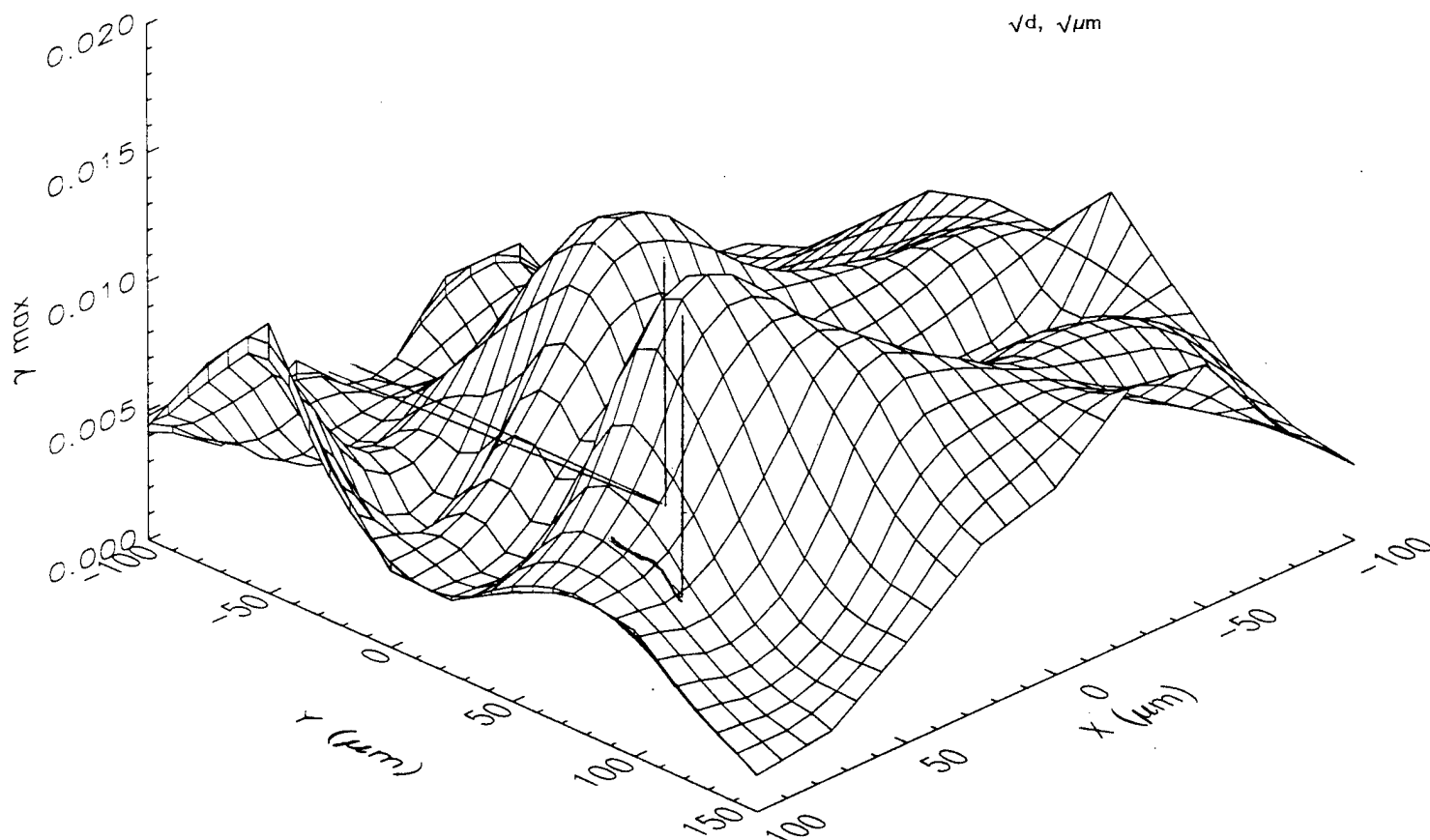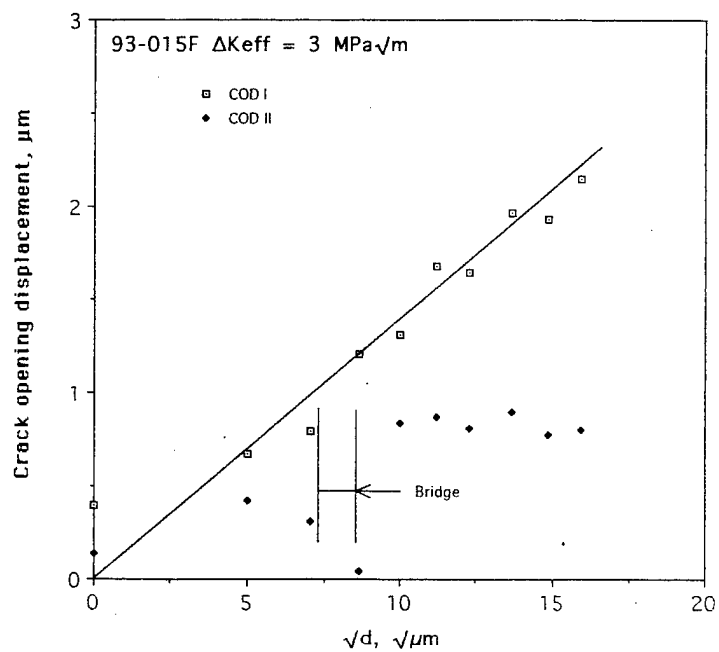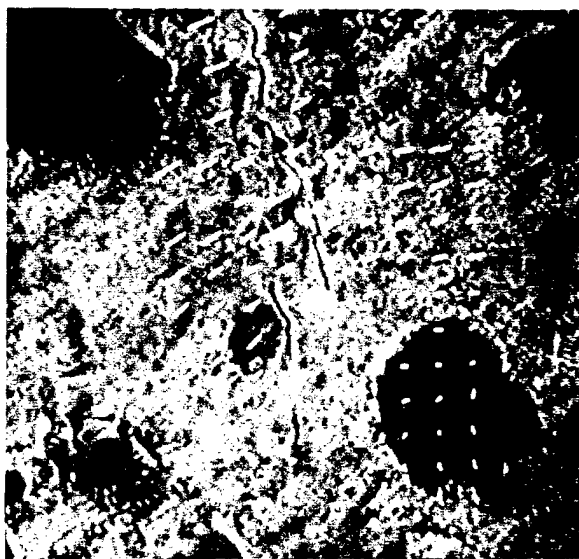
Fig. 25   Composite 93-015F. Photograph with displacment overlay, COD and distribution of maximum shear strain are shown at ΔK_{eff} = 3 MPa√m. Displacements were measured each 25 μm, and are shown 15 times actual.
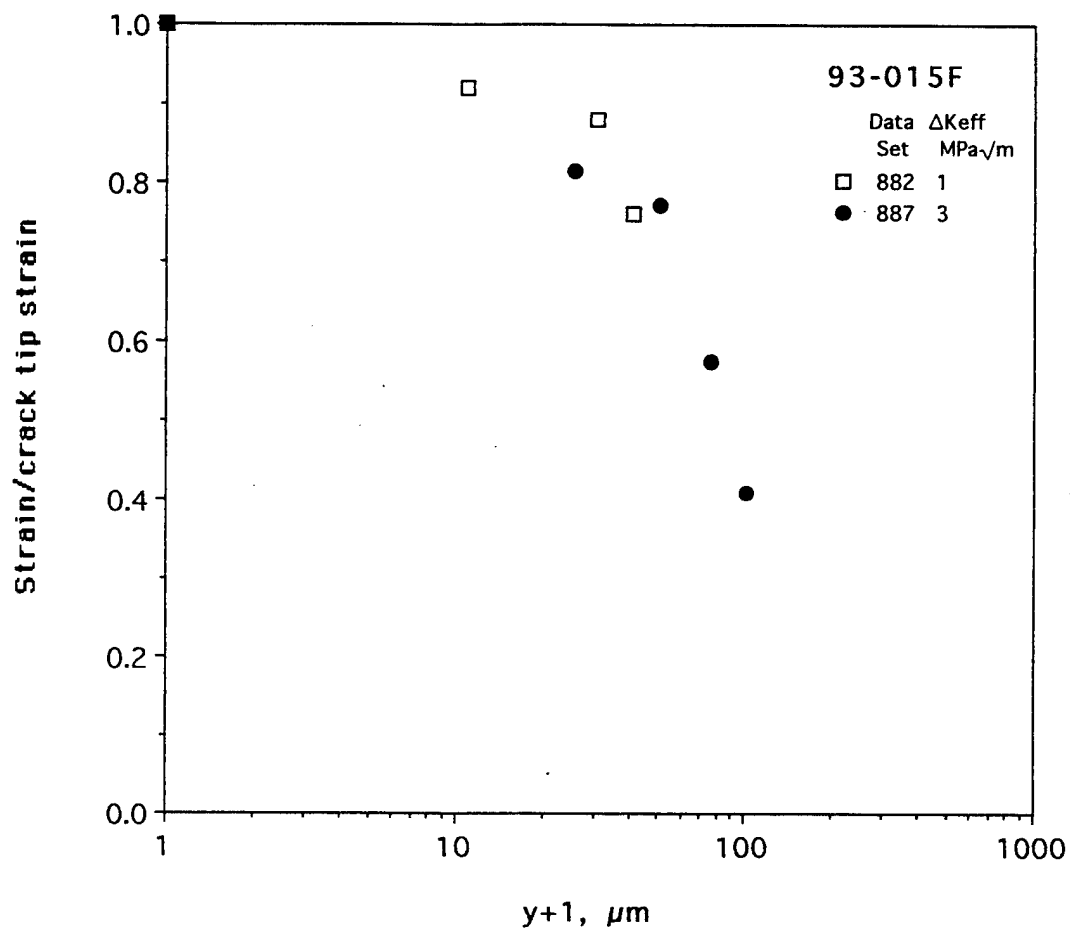
Fig. 26   Composite 93-015F. Distribution of maximum shear strain ahead of the crack tip normalized by crack tip strain for the two crack tips shown in Figs. 24 and 25. One μm has been added to distance so that the crack tip may be shown.

The crack tip region seen in **Figure 25** is complex because of the two matrix bridging regions. The effective crack tip is at the lower end of the central crack next to the intermetallic particle. The bridge between that crack and the main crack is acting like a hinge and, as seen in the COD plot, does not have much of an effect on Mode I COD. Strain on the right side is lower within the Cr_2Nb particle. Note that none of the particles seen here have fractured.

The strain distribution shown in **Figure 26** is unlike that of monolithic alloys. This behavior was confirmed by analyses of other several other crack tips.

For Nb-10Si composite with 25% Nb_5Si_3, typical crack tip analyses are shown in **Figures 27** and **28**. In contrast to the composite with Cr_2Nb, fatigue cracks in this material exhibited fewer bridged regions and microcracks accompanying the main fatigue crack.

The crack shown in **Figure 27** was growing within a region of mixed Nb_5Si_3 and secondary niobium at $\Delta K = 7.5$ for a $\Delta K_{eff} \approx 0.1$. The crack enters the photograph from the top and the tip is shown by the circle. A region of primary niobium is seen to be approximately 7 μm ahead of the crack tip. The large grains of the primary niobium, revealed by ion etching, indicate that it has been recrystallized. The crack opening displacement diagram shows non-linear behavior. At the crack tip, the level of Mode II opening is comparable to that in Mode I.

The crack in **Figure 28** has grown through a field of intermetallic with secondary niobium, and the crack tip is within primary niobium. Only 2 μm from the tip is an oval-shaped intermetallic particle, an outline of which is shown on the zero strain plane of the strain distribution plot. Note that strain is largest within the primary niobium to each side of this particle.

The distribution of maximum shear strain ahead of the crack tip is shown for several of the cracks analyzed in **Figure 29**. In **Figure 29(a)** is a linear correlation, and in **Figure 29(b)** the normalized value is shown vs ln (y+1). These strain distributions are fairly typical except for Set 984, $\Delta K_{eff} \approx 0.1$. However, contrary to the results for the Nb-Cr-Ti matrix alloy 93-018, the data do not collapse to a single line; thus, one value of m′ does not describe all the results. Even two crack tips at the same value of ΔK_{eff} (Sets 897 and 898) do not share the same strain distribution. Prediction of strain ahead of a fatigue crack tip for this composite is not possible based on this analysis.
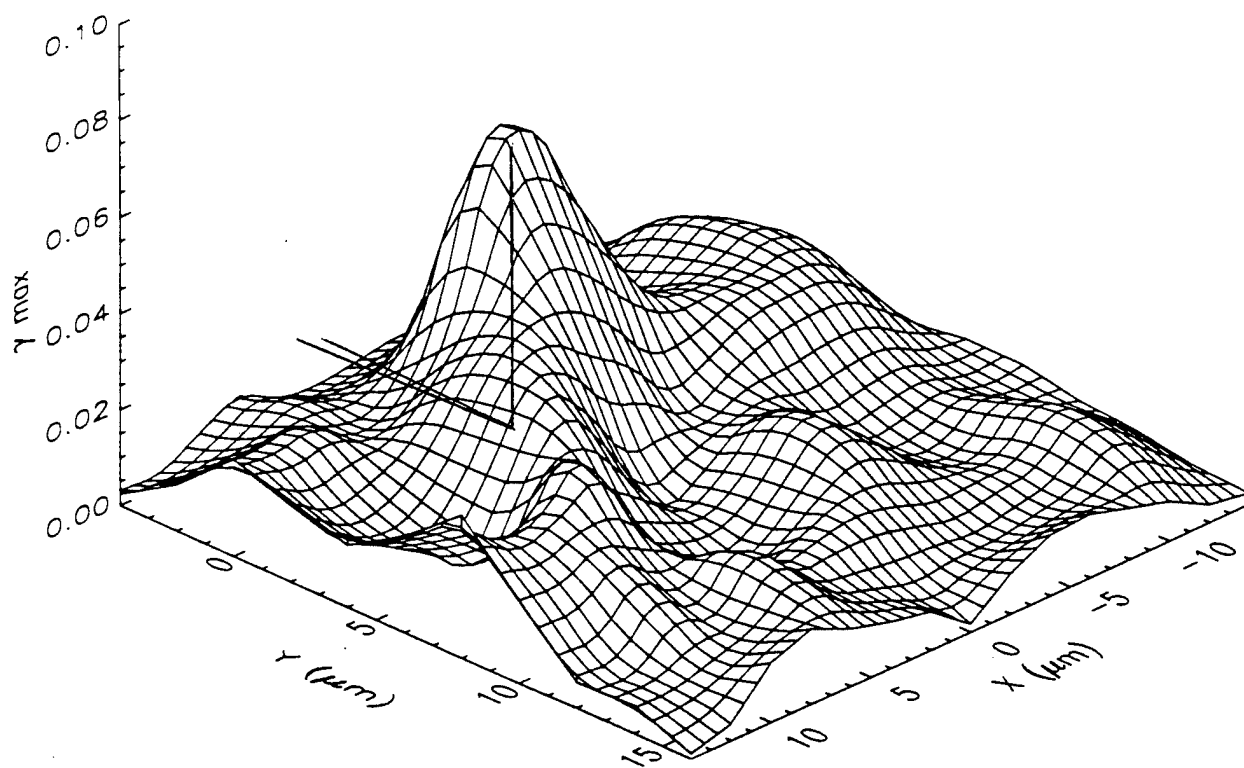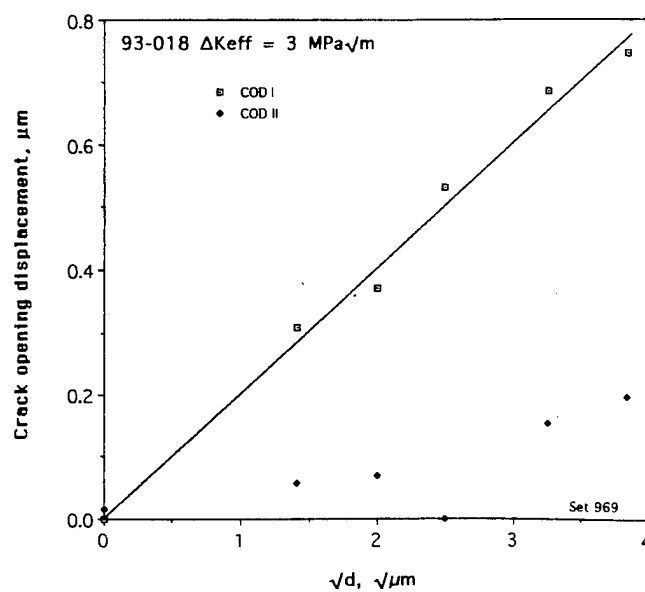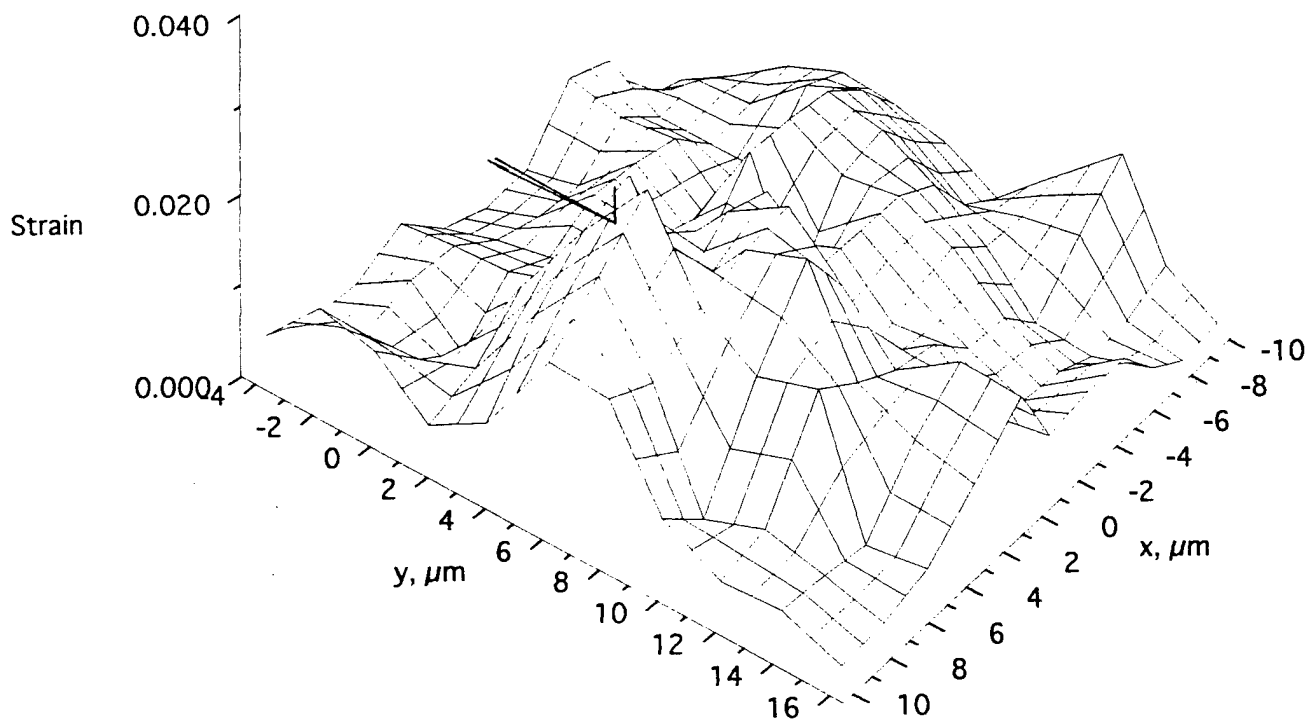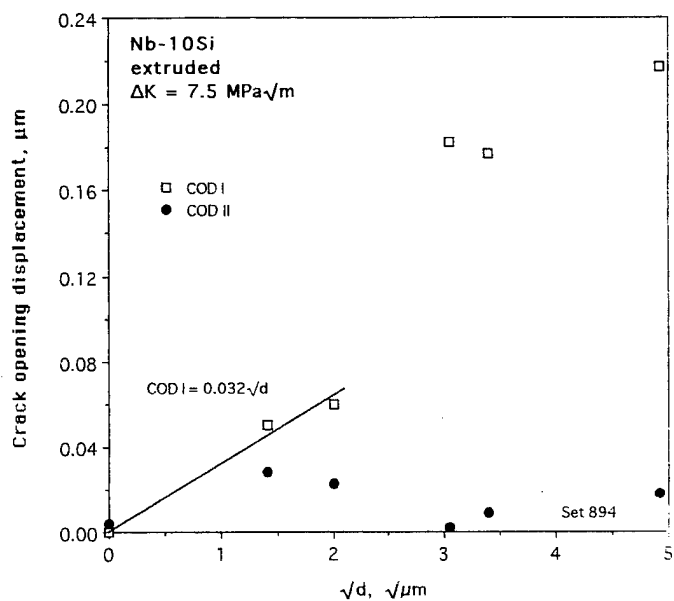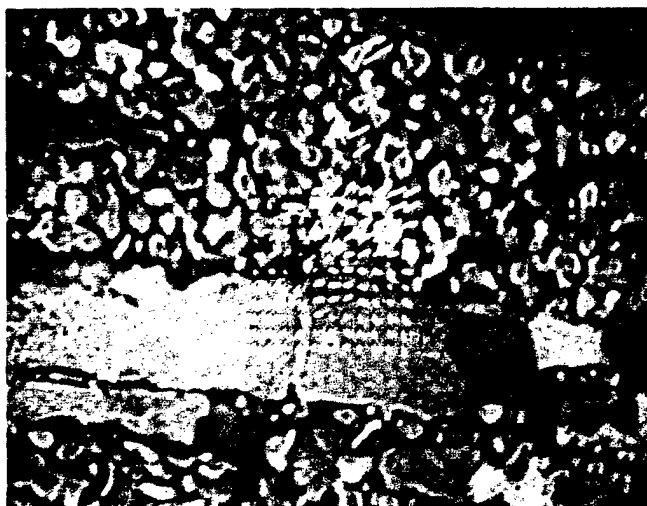
Fig. 27   Composite Nb-10Si. Photograph with displacment overlay, COD and distribution of maximum shear strain are shown at ΔK_{eff} = 0.1 MPa√m. Displacements were measured each 2 μm, and are shown 20 times actual.
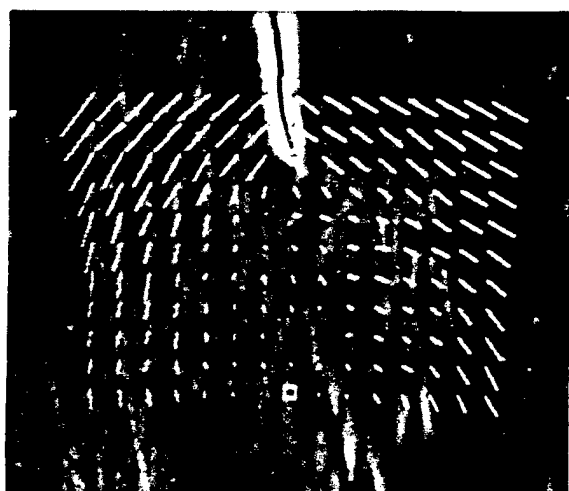
48
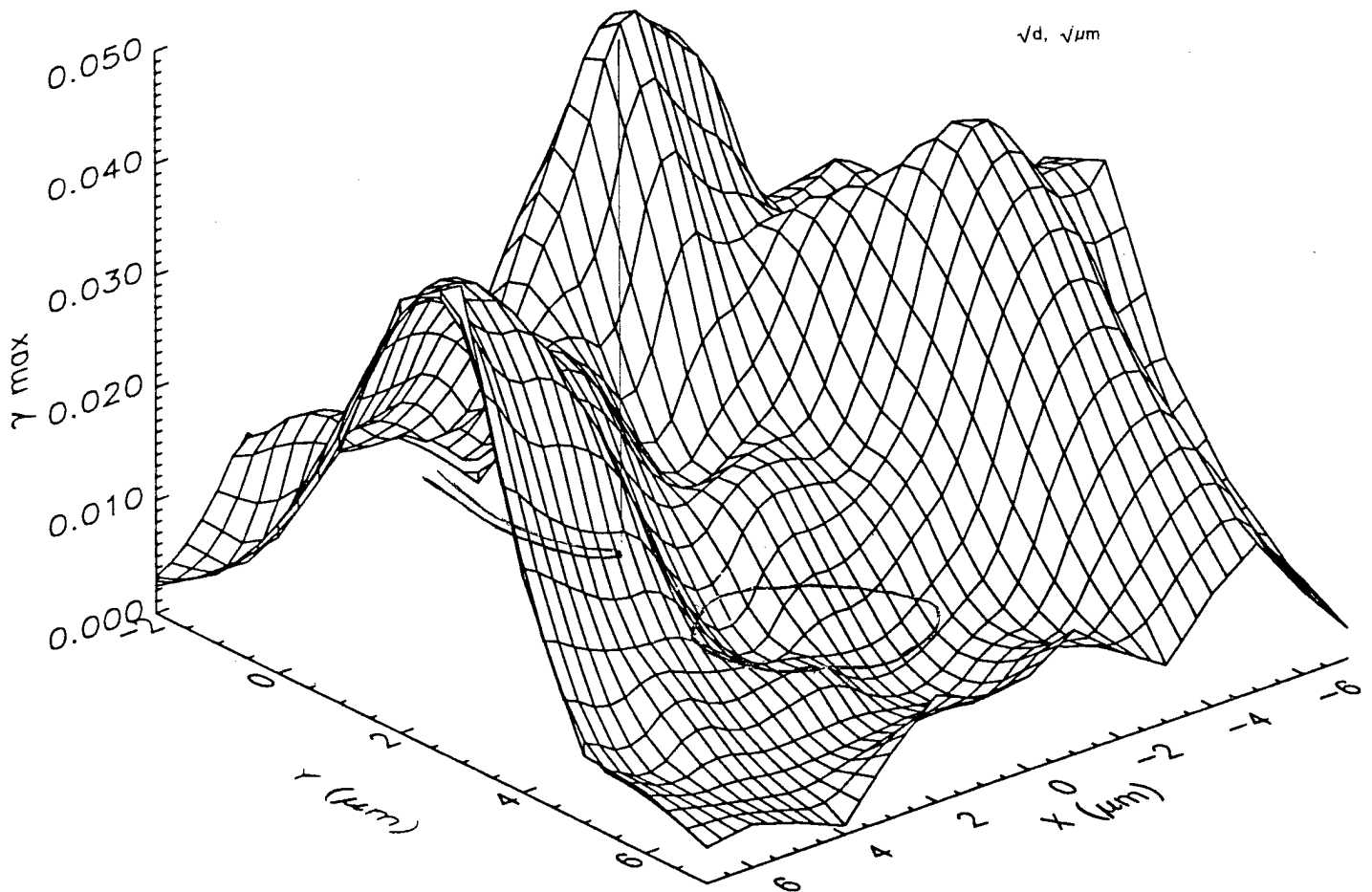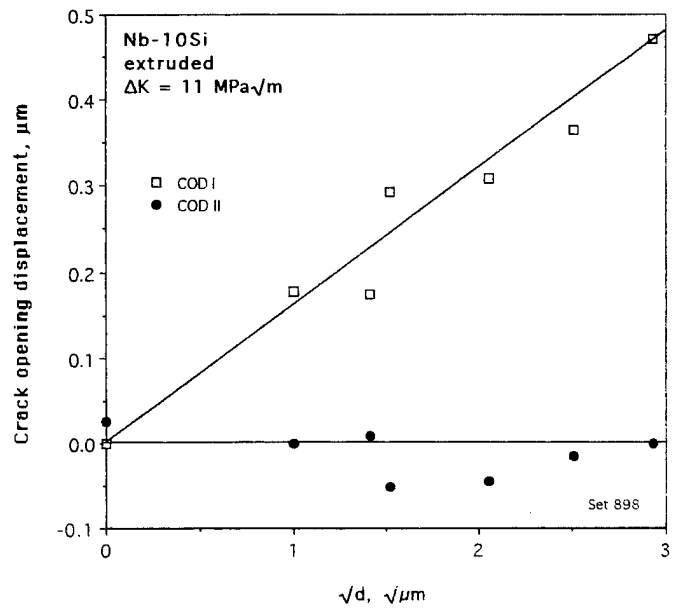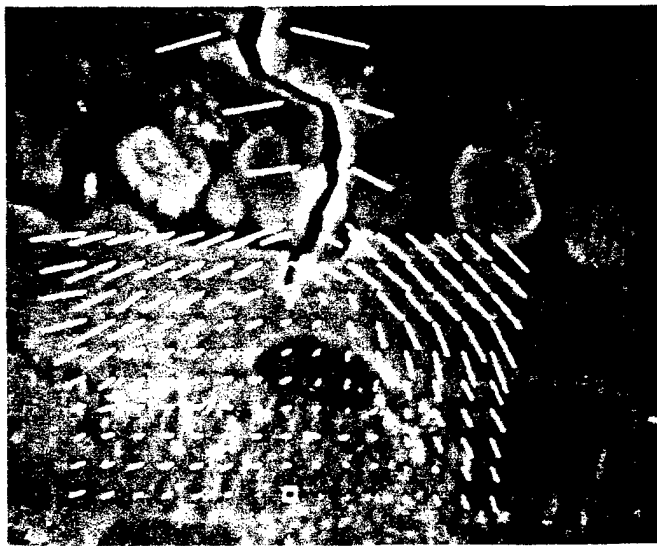
Fig. 28 Composite Nb-10Si. Photograph with displacment overlay, COD and distribution of maximum shear strain are shown at $\Delta K_{eff} = 4.0$ MPa√m. Displacements were measured each 1 μm, and are shown 10 times actual.
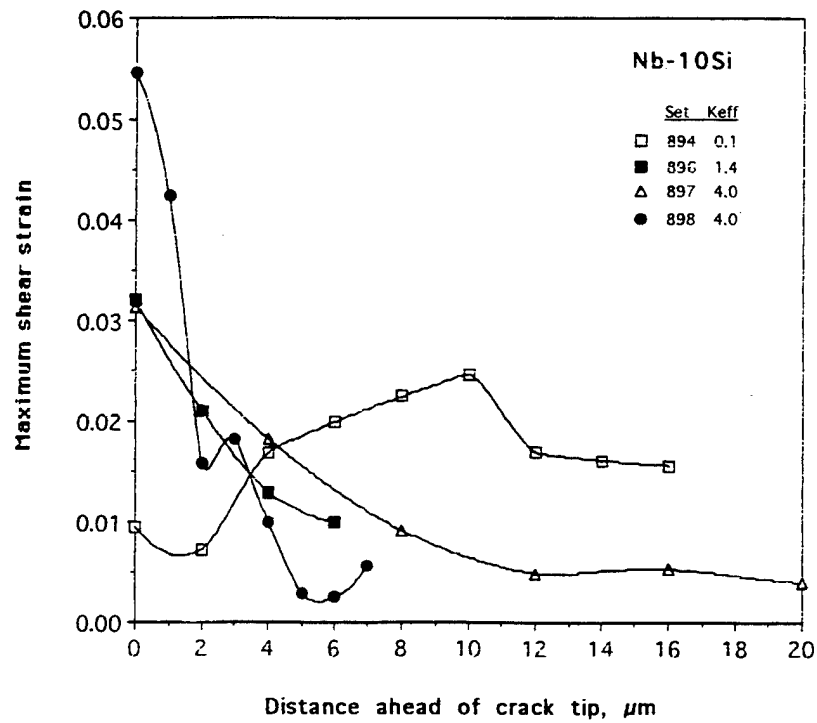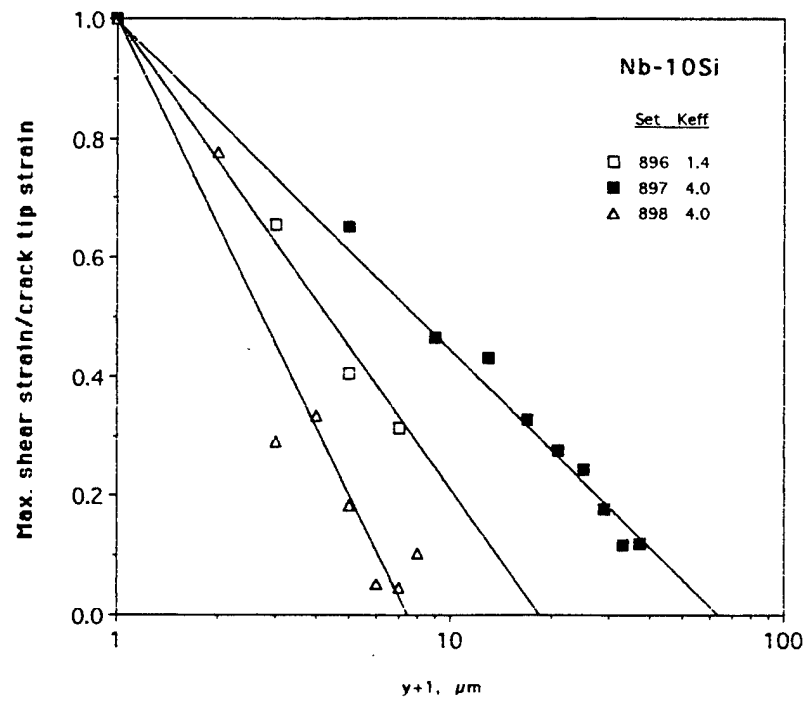
Fig. 29. Composite Nb-10Si. Distribution of strain ahead of crack tip. (a) Maximum shear strain vs. distance. (b) Normalized strain vs. ln (distance). One μm has been added to distance so that the crack tip may be shown.

E. Crack Tip Strain, CTOD, and $\Delta K_{effective}$ Correlations

Correlations of the various crack tip parameters have been made so that a comparison may be made between these measured material responses. In **Figure 30**, CTOD is correlated with crack tip strain. It should be noted that not all the data for each material was used because at higher stress intensity the transition from high constraint (plane strain) to lower constraint (plane stress) had begun; thus, the comparison with lower K was inappropriate. In general, the correlation between CTOD and γ_{max} is good, as has been shown for many other materials, and there is not much difference between the correlations found for the three materials.

Correlation of both CTOD and γ_{max} are shown vs ΔK_{eff} in **Figures 31** and **32**. This is the appropriate comparison, rather than with ΔK, because of the differences in ΔK_{th} already noted. It should be remembered that $\Delta K_{eff} = \Delta K - \Delta K_{th}$. Comparison of CTOD with ΔK_{eff} is given in **Figure 31**, while γ_{max} vs ΔK_{eff} is shown in **Figure 32**. There appears to be more similarity between the matrix alloy and Nb-10Si results than for the Nb-Cr-Ti composite, and the slopes of all these correlations are approximately 1; the greatest exception to this is CTOD for Nb-10Si, but more data might change that perception. Crack tip strains for Nb-10Si tend toward those of the Nb-Cr-Ti matrix alloy at low ΔK_{eff}, but are closer to the Nb-Cr-Ti composite at larger values of ΔK_{eff}.

Results of the crack tip parameter measurements shown in **Figures 30-32** and from the crack growth rate measurements of **Figures 14-19** have been summarized in **Table 5**. The values listed are estimates based on the data available, which is much less than desirable for the composites, but enough to characterize them approximately.

Crack tip strains at large K values are lower for both composites than for the Nb-Cr-Ti matrix alloy, as expected from the K_Q values. The sparse crack growth data indicate a lower slope for the Cr_2Nb containing composite than for the Nb_5Si_3 containing composite, probably because the Nb-Cr-Ti matrix of the former is more ductile than the Nb-Si matrix of the latter. More data would probably indicate that there is not much difference in crack growth rates between the composites in the intermediate region (10^{-6} to 10^{-8} m/cycle), but the Nb-Cr-Ti composite would be expected to grow at lower values of ΔK than Nb-10Si.
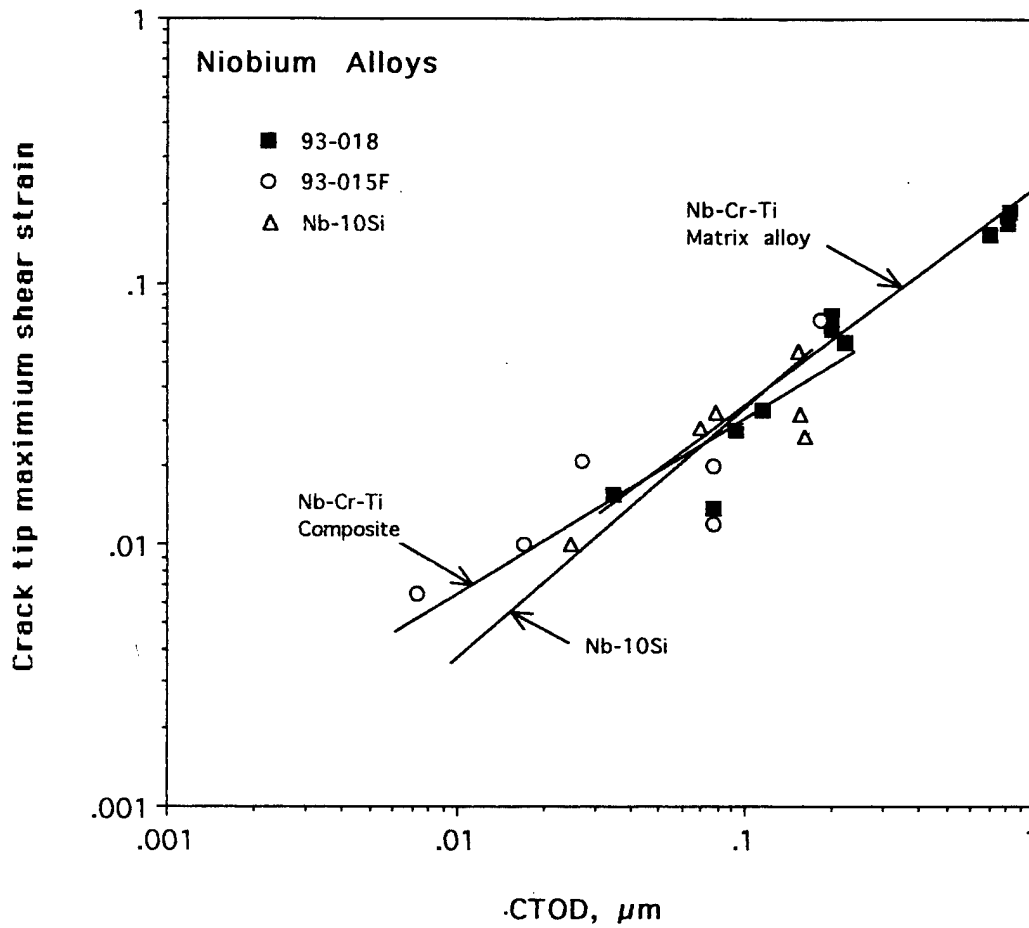
Fig. 30   Correlation between maximum shear strain at the crack tip and CTOD (the Crack Tip Opening Displacement). CTOD is defined as the COD 1 μm from the crack tip.
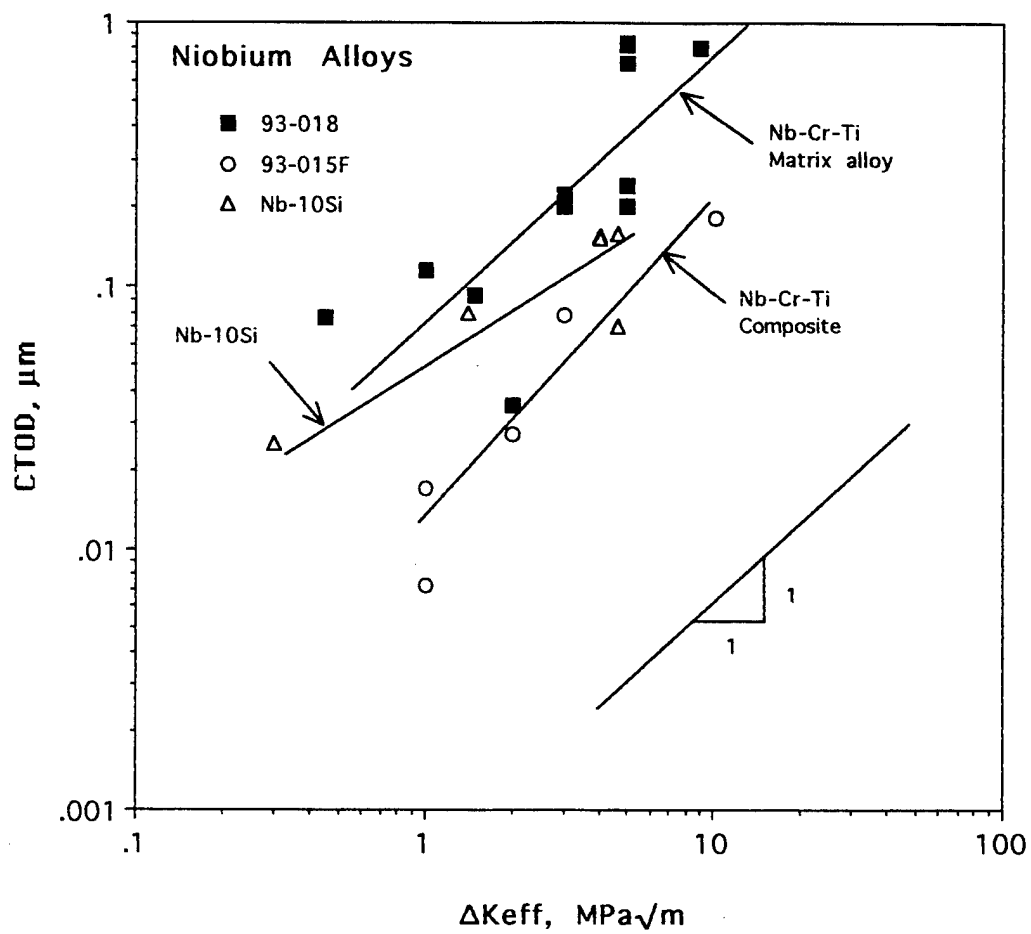
Fig. 31 Correlation between CTOD and ΔK_{eff}.
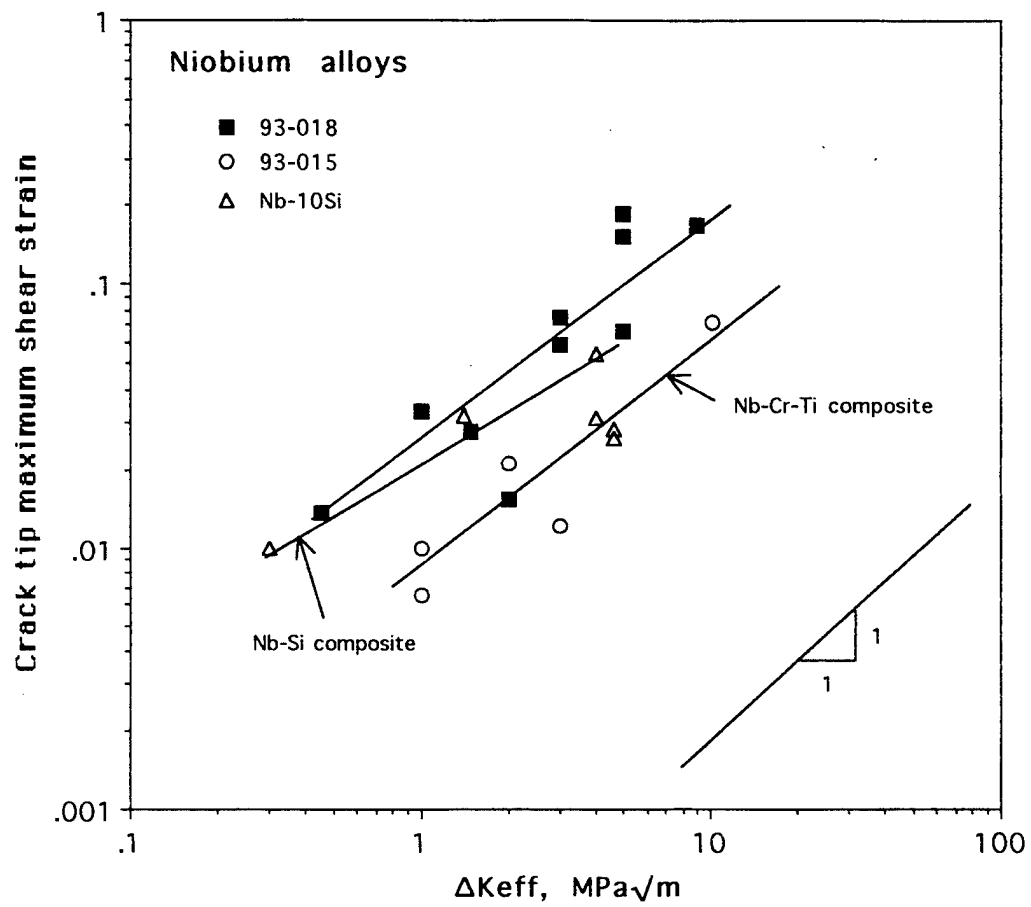
Fig. 32 Correlation between crack tip maximum shear strain and ΔK_{eff}.

Table 5
Summary of Crack Tip Mechanics
and Crack Growth Rate Parameters

Matrix Material 93-018	46% Cr$_2$Nb 93-015F	Nb-10Si
$\gamma_{max} = 0.11\, CTOD^{0.82}$	$\gamma_{max} = 0.14\, CTOD^{0.68}$	$\gamma_{max} = 0.335\, CTOD^{0.95}$
$CTOD = 7.1 \times 10^{-2} \Delta K_{eff}^{1}$	$CTOD = 1.3 \times 10^{-2} \Delta K_{eff}^{1.22}$	$CTOD = 5.2 \times 10^{-3} \Delta K_{eff}^{0.68}$
$\gamma_{max} = 2.5 \times 10^{-2} \Delta K_{eff}^{0.82}$	$\gamma_{max} = 7.4 \times 10^{-3} \Delta K_{eff}^{0.83}$	$\gamma_{max} = 2.0 \times 10^{-2} \Delta K_{eff}^{0.64}$
$\Delta K_{th} = 7.0\, MPa\sqrt{m}$	$\Delta K_{th} = 4.0\, MPa\sqrt{m}$	$\Delta K_{th} = 7.4\, MPa\sqrt{m}$
$da/dN = 3.7 \times 10^{-9} \Delta K_{eff}^{1.7}$	$da/dN = 2.5 \times 10^{-2} \Delta K_{eff}^{0.82}$	$da/dN = 1.0 \times 10^{-12} \Delta K_{eff}^{6}$
$da/dN \approx 3.3 \times 10^{-12} \Delta K^{4.8}$	$da/dN \approx 1.3 \times 10^{-12} \Delta K^{8.4}$	$da/dN \approx 3 \times 10^{-21} \Delta K^{12.5}$

F. Constraint Caused By Second Phase

Plastic constraint is known to alter the flow properties of materials. The technique normally used to assess the effect of constraint is as follows: fracture strain is measured for notched round bars where the level of constraint may be changed by varying notch radius. However, for composites, this technique has been demonstrated not to provide the same correlation between fracture strain and constraint as found for unreinforced materials [13]; in fact, fracture strain was found to be independent of constraint.

It was hypothesized that deformation within the composite matrix is constrained locally by the particles, thereby decreasing the matrix fracture strain to values below those expected from the unreinforced matrix. The imposition of local, or "microconstraint," over rides the effects of the notch radius macroconstraint. To test the validity of this hypothesis, a method was sought to use the strains measured in the crack tip region to determine the level of microconstraint. Thus, the levels of constraint exhibited by the unreinforced matrix alloy could be compared to constraint values determined for the composites.

Constraint is usually defined as the mean stress, or hydrostatic stress, divided by the effective stress. Since stress cannot be measured with enough spatial resolution to be useful in these composites, a method was sought to determine constraint from the strains determined with stereoimaging. The derivation given in the Appendix indicates that a constraint value can be derived from strains that is equivalent to that used for stress constraint. It is possible to define a

constraint in terms of strain because at the surface, a condition of plane stress exists. The strain definition of constraint equals mean strain/effective strain. In plane stress, constraint has the same bounds as when defined through stress: 0 to 0.5 [14]. By comparison, the maximum value of constraint normally encountered in plane strain is 3.

The concept of particle induced microconstraint has been tested by comparing the constraint levels of the matrix material with those of the composites. If correct, the levels of constraint for the composites should be higher than for the unreinforced matrix alloy. Constraint values were computed for the same crack tips for which strain distributions were shown in previous sections. For purposes of the comparison, a value of ≥ 0.4 was chosen to represent high constraint.

Constraint values derived for the matrix alloy 93-018 are shown in **Figures 33** and **34**. Comparison of these figures with the maximum shear strain distribution indicates that lower values of constraint are often found in areas with the largest strain; i.e., constraint has been relieved by deformation. The area of these figures having constraint levels of 0.4 and above are not large — approximately 10%.

For the 42% Cr_2Nb composite 93-015F, the level of constraint is generally larger than for the matrix alloy. The crack tip shown in **Figure 35** has fairly low levels of constraint near the crack tip, but has constraint ≥ 0.4 covering 75% of the area. The constraint values shown in **Figure 36** are lower, but constraint ≥ 0.4 still covers 20% of the area, including the area near the crack tip. In the regions approximately $\pm 45°$ to the crack growth plane, constraint is high.

Constraint in the Nb-10Si composite is the highest in regions of the crack tip region containing intermetallic. In **Figure 37**, where the top half of the region shown is intermetallic, constraint is higher than in the lower region of the figure that is primary niobium. Overall, constraint of ≥ 0.4 covers 43% of the area. The constraint distribution shown in **Figure 38** is more difficult to interpret. Most of the deformation is within niobium, but there is an intermetallic particle 2 μm directly ahead of the crack tip where strain was limited — see **Figure 28**. Constraint is lowest at the crack tip and remains low in the region of the particle. However, on each side of the particle, constraint is larger. Constraint ≥ 0.4 covers 21% of the area.

These results indicate that constraint is generally higher in the composites than in the matrix alloy. This may be seen by inspection of the figures and from the areas having a constraint of ≥ 0.40 as summarized in **Table 6**. The constraint magnitude values shown in the table were derived by ratioing area to constraint; thus, a constraint magnitude of 0.5 corresponds to a constraint ≥ 0.4 covering 100% of the area.
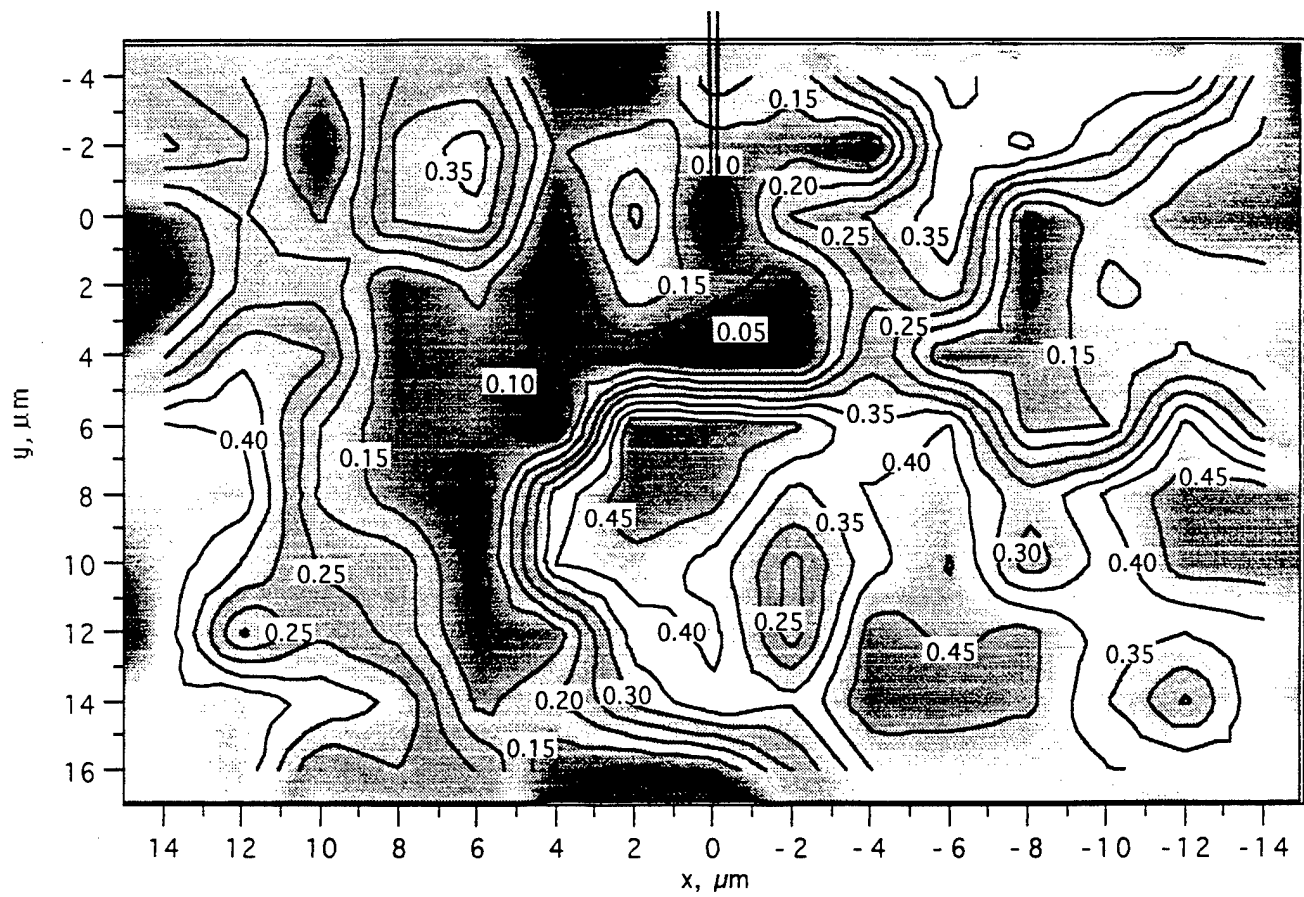
Fig. 33.   Matrix alloy 92-018.   Map of constraint values derived for
the crack tip shown in Fig. 21.
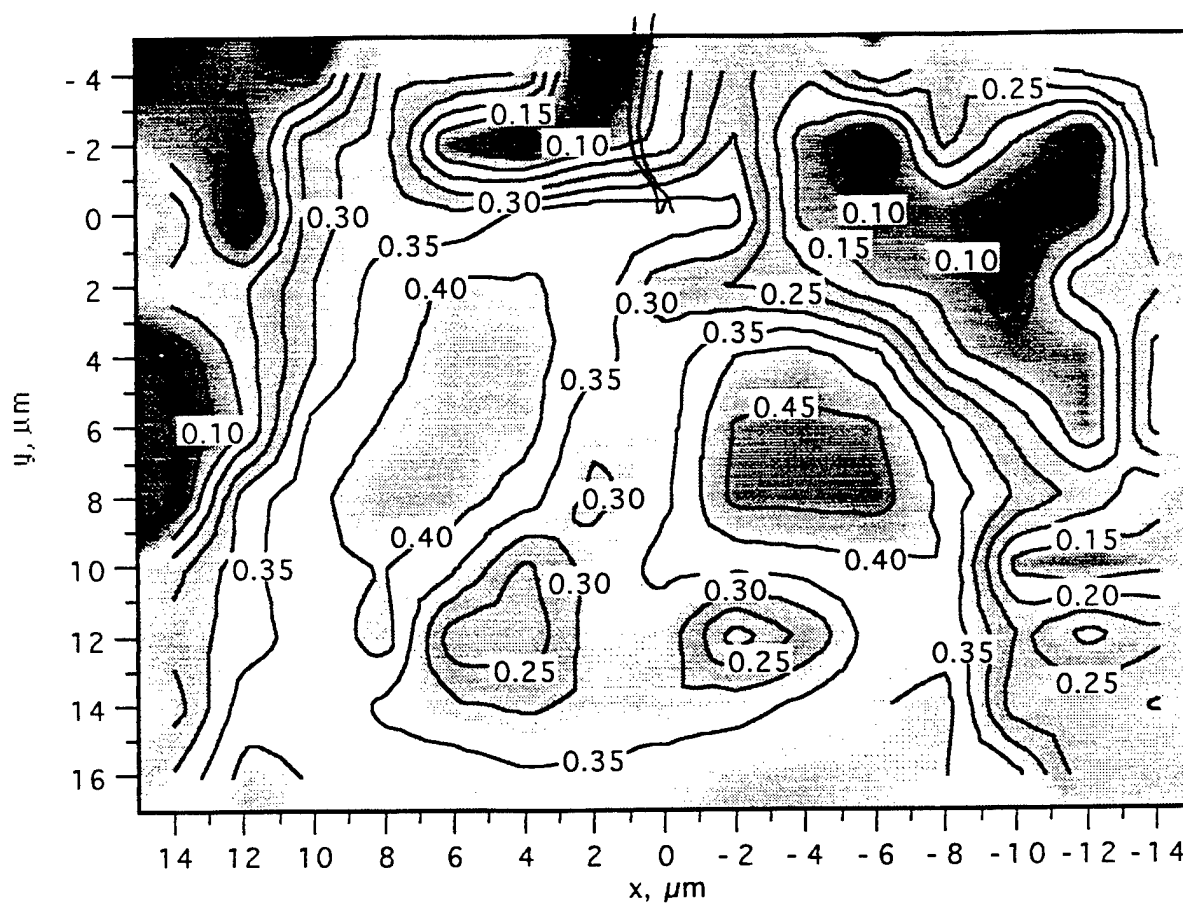
Fig. 34. Matrix alloy 93-018. Map of constraint values derived for the crack tip shown in Fig. 22.
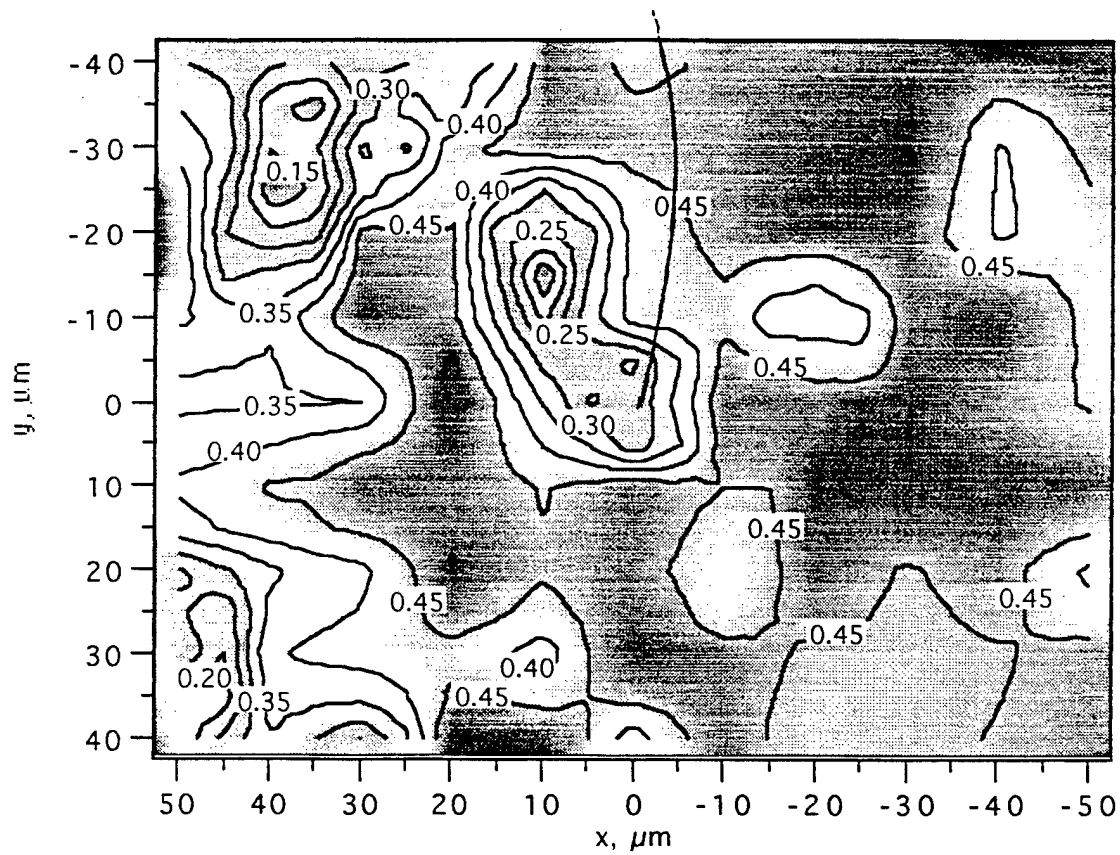
Fig. 35. Composite 93-015F. Map of constraint values derived for the crack tip shown in Fig. 24.
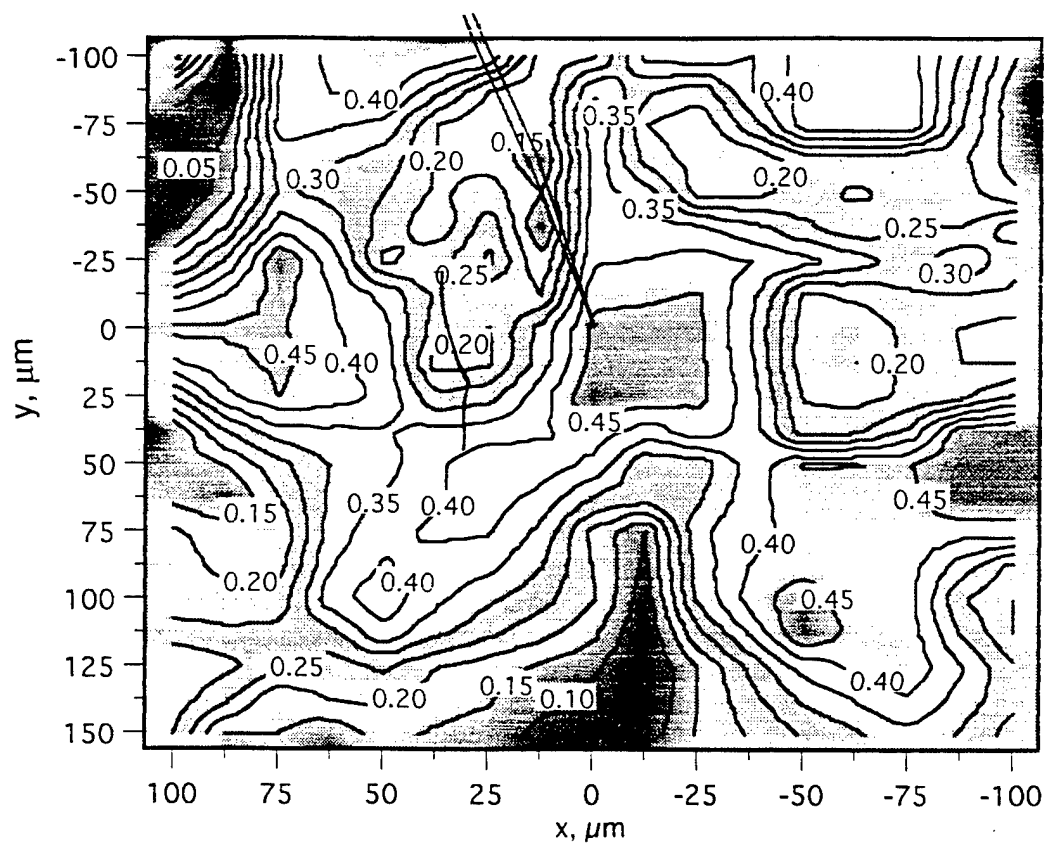
Fig. 36. Composite 93-015F. Map of constraint values derived for the crack tip shown in Fig. 25
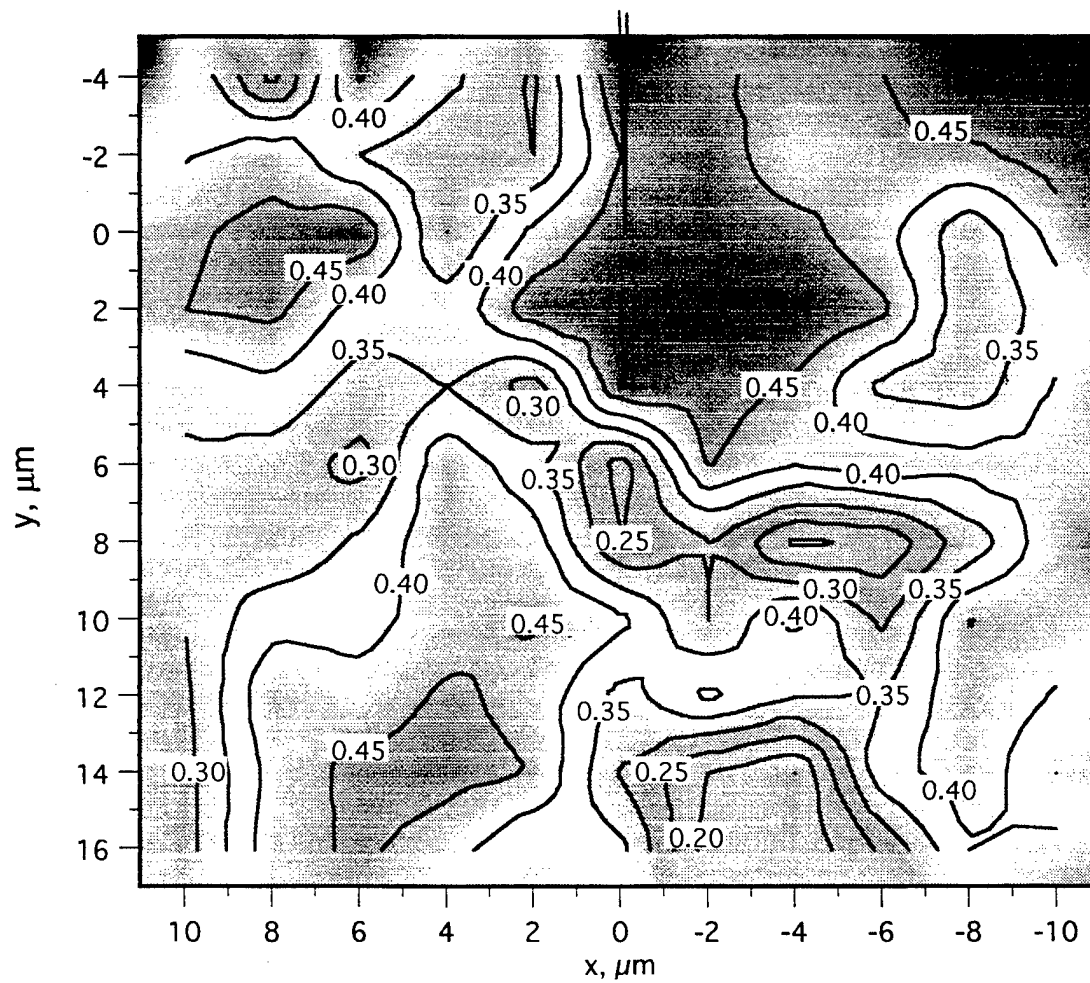
Fig. 37   Composite Nb-10Si. Map of constraint values derived for the crack tip
shown in Fig. 27.
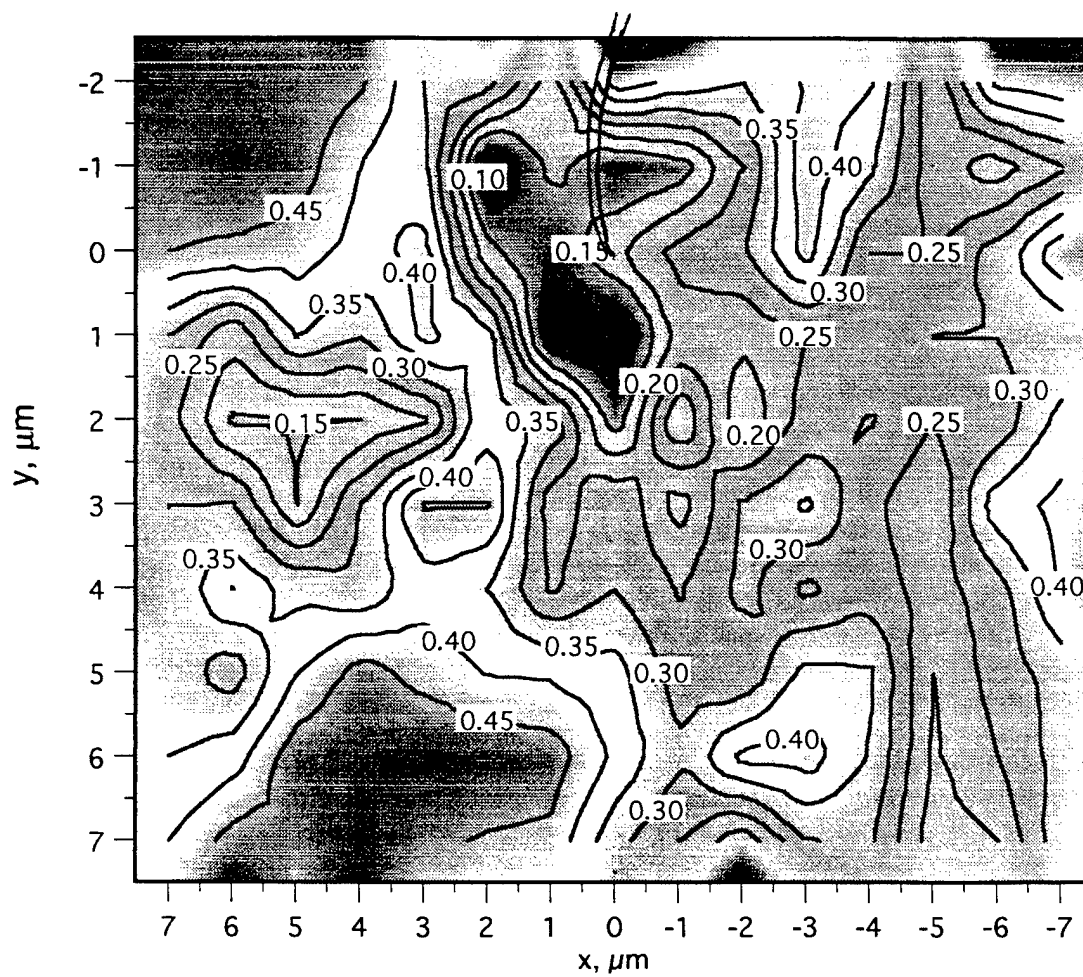
Fig. 38   Composite Nb-10Si. Map of constraint values derived for the crack tip shown in Fig. 28.

Table 6
Crack Tip Constraint

Material	Figure No.	Data Set No.	Percent Area ≥ 0.40	Constraint Magnitude	Crack Tip Strain
93-018 (Matrix)	33	969	9.1	0.046	0.062
	34	972	6.5	0.033	0.152
93-015F 42% Cr$_2$Nb	35	882	75	0.375	0.0074
	36	887	21	0.155	0.0184
Nb-10Si	37	984	43	0.215	0.008
	38	898	21	0.105	0.082

The composites have 2 to 8 times the area of high constraint seen in the matrix material. With this result, it seems much more probable that the hardness values measured in the matrix region of the composite (see **Table 1**) are higher because of deformation constraint than because the matrix deformation characteristics are different than in the unreinforced matrix alloy.

Crack tip strain and constraint are correlated in **Figure 39** which indicates the same general trend as shown for aluminum alloys in Ref. 13. The matrix alloy shows low constraint but high crack tip strains while the composites exhibit the opposite relationship. The empirically derived relationship used in ref. 15 to relate strain to constraint is

$$\varepsilon_{\text{crack tip}} = \varepsilon_o [\sigma_m / \sigma_{\text{eff}}]^{-q} \tag{2}$$

where constraint equals $\sigma_m / \sigma_{\text{eff}}$. For the data of **Figure 39**, values for the constants $\varepsilon_o = 2.25 \times 10^{-3}$ and q = 1.22 were derived, and the line shows the relation.

The wide variation in level and area of high constraint for the composites is expected because of the complex interaction between the stress field of the crack and the deformation blockage caused by intermetallic particles. These results indicate that the hypothesis of localized constraint of matrix flow by particles in the composites is essentially correct.
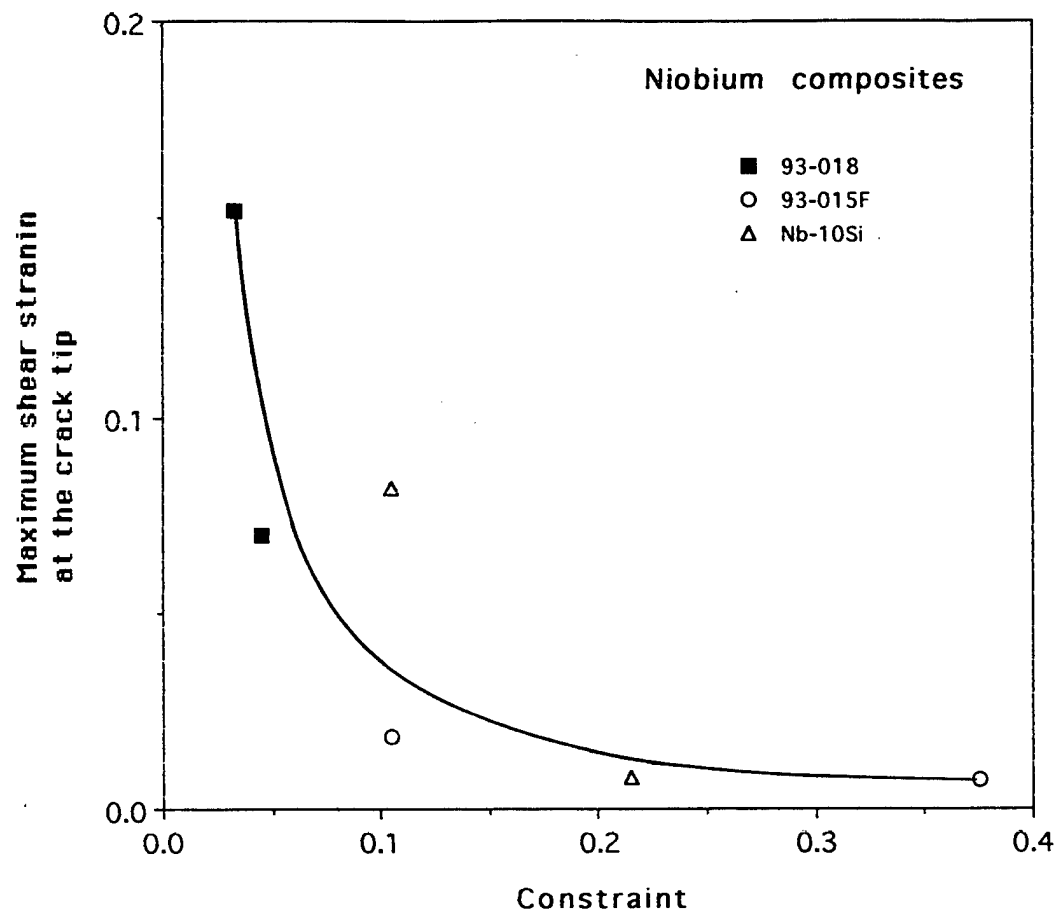
Fig. 39   Correlation of crack tip strain with constraint.   The line shown was fit
to the data.

G. Fractography

The fracture surfaces of these materials varied widely, as was expected from differences in microstructure. Although detailed fractography has not been performed, very little evidence of periodic crack arrest (fatigue striations) may be found on any of the fracture surfaces, except for the matrix alloy 93-018. In general, the fracture surfaces evidence very little of the extensive deformation found from crack tip plasticity measurements.

The fracture surface in each grain of the matrix alloy 93-018 shows large differences in appearance, **Figure 40**, and the topography of the surface is very rough. At high magnification in some of the grains, there is evidence of periodic crack arrest; several examples are shown in the figure. Striations that are closest to the appearance of those found in aluminum alloys or steels are shown in (b) where the average spacing is 2.25 μm. In (c), the deep grooving seen is parallel to the direction of crack growth and may not be not indicative of periodic crack arrest unless the local crack growth direction was perpendicular to the general crack growth direction. Average spacing of the grooves is 2.8 μm. In (d) the growth direction is within 30° of the nominal direction of crack growth and the spacing is 1.8 μm. Allowing for differences in facet tilt, and assuming that all the periodic structures are due to crack arrest, the spacing is about 2.25 μm for this region of crack growth, which is about 100 times the average crack growth rate for nominal values of ΔK.

Macro-appearance of the composite fracture surfaces is shown in **Figure 41**: The Nb-10Si fracture surface is smooth in comparison to those of the Nb-Cr-Ti composites. The fracture surfaces of 93-015F are transgranular while those of 93-016 are intergranular. In all cases, the notch is at the top and the direction of crack growth was from top to bottom.

The Nb-Cr-Ti composite 93-015F also had a rough fracture surface, as shown in **Figure 42**, but not as faceted as that of the matrix material. At higher magnification (top photograph), numerous fractured intermetallic particles are seen. An estimate of the area fraction of intermetallics is 20%, which is somewhat less than the estimated 38 vol.% of Cr_2Nb in the composite. At higher magnification, some markings exist that might be interpreted as indicating fatigue crack arrest, but these were atypical to the general appearance of the fracture surface. The "river lines," formed approximately parallel to the direction of crack growth, are evidence of limited plasticity. The Cr_2Nb intermetallic fractured with a very brittle, polycrystalline appearance, in some cases conchoidal, and appeared to be faulted or twinned.

Fig. 40 Fractography of the fatigue region of Nb-Cr-Ti matrix alloy 93-018. Crack growth was from bottom to top for all regions. (b) From smooth facet on the right-center; (c) from the large facet on the left center; (d) from the facet in the center.

66
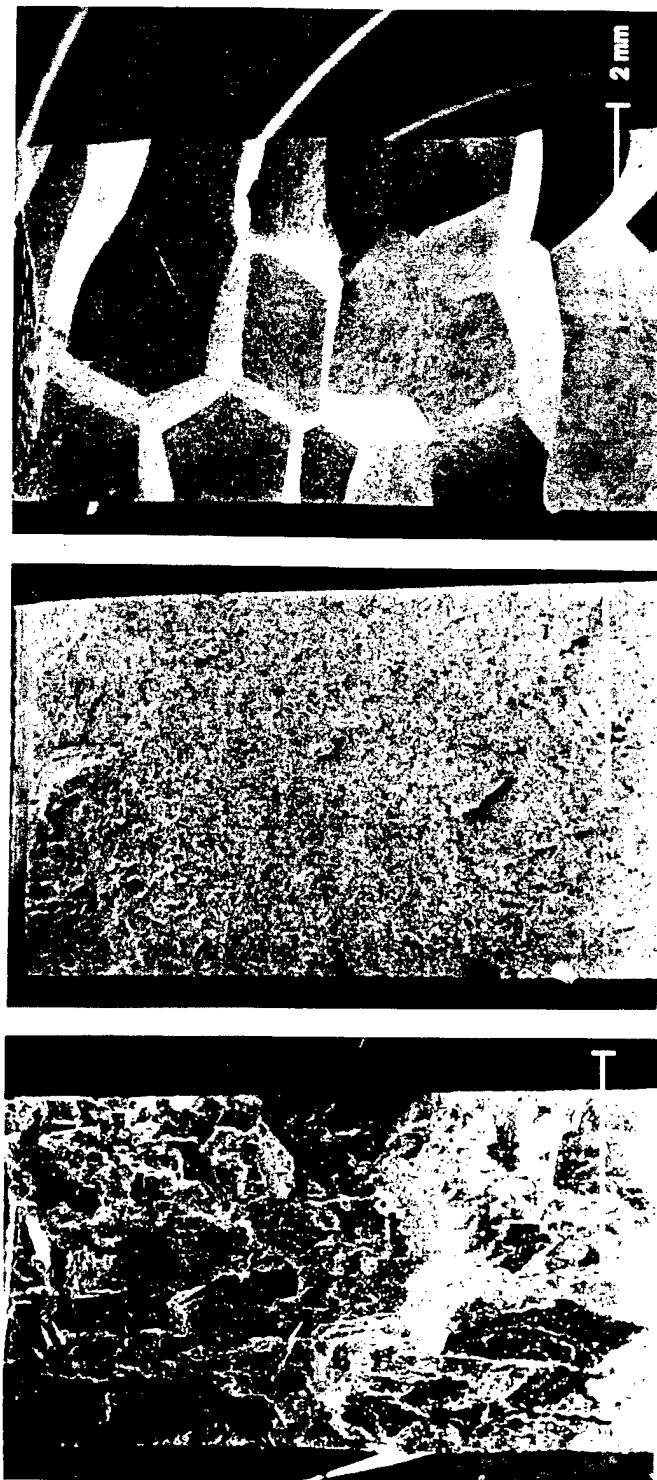
Fig. 41   Comparison of the composite fracture surfaces.
(left) 93-015F 38 vol.% Cr_2Nb (center) Nb-10Si (right) 93-016 22 vol.% Cr_2Nb.
The crack starting notch is located at the top of each photograph.

67
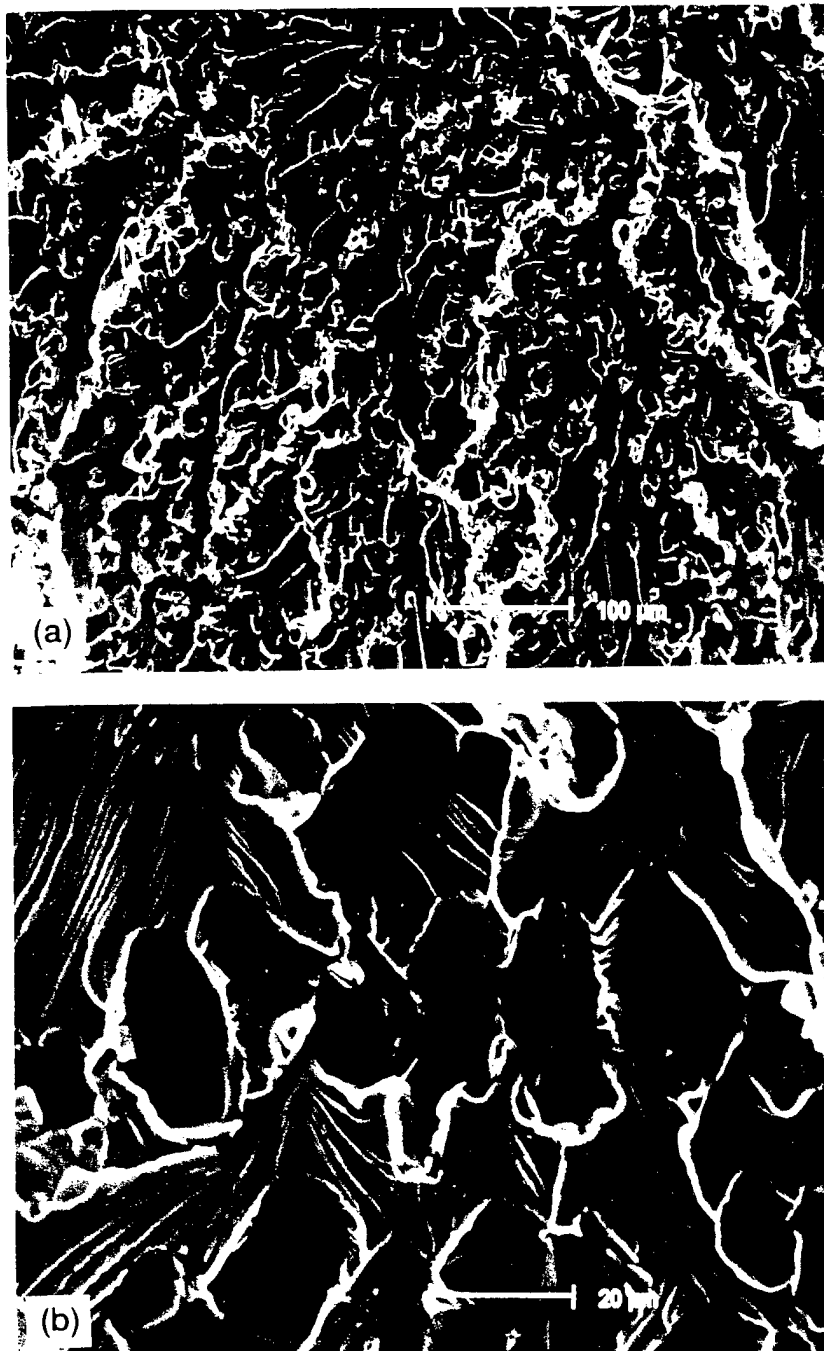
Fig. 42 Fatigue region of the Nb-Cr-Ti composite 93-015F with 38 vol.% Cr_2Nb. Crack growth was from top to bottom.

The composite 93-016, which had nearly continuous Cr_2Nb intermetallic on the grain boundaries, fractured only through the grain boundaries, as shown in **Figure 41**. Examination at higher magnification, **Figure 43**, showed regions of conchoidal fracture (upper photograph) and, on facets at high tilt to the electron beam (lower photograph) some sketchy periodicity might be discerned. The nature of fracture through the Cr_2Nb was not the same as found in composite 93-015F, but morphology of the intermetallic was not the same.

The fatigue fracture surface of the extruded composite of Nb-10Si was macroscopically flat and nearly featureless, as seen in **Figure 41**. At higher magnification, **Figure 44**, there is some evidence of crack arrest in the matrix regions, see (a) and (c), but not much. The isolated, small bits of secondary Nb(ss) appears to have fractured in a very ductile manner, tapering down to chisel points in many places. The primary Nb(ss) evidences considerable plasticity, but does not narrow to a chisel point in vary many places. The area of intermetallic seen on the fracture surface varies considerably with location, in agreement with observations of the crack path, **Figure 11**. There appeared to be more secondary cracking within the intermetallic in the interior of the specimen than observed on the surface.

H.   Summary and Comparison of Fatigue Crack Growth Results

A comparison of fatigue crack growth results for the various materials is shown in **Figure 45**. Crack growth rates for the Nb-Cr-Ti composite are considerably higher than for the matrix alloy except at about 10^{-8} m/cycle, or $\Delta K \approx 8$ MPa$\sqrt{m}$. Threshold ΔK is lower for the composite, but the large difference is at the high end of the crack growth rate curve ($\approx 10^{-6}$ m/cycle) where ΔK for the matrix alloy is twice that for the composite. One reason for this difference in growth rates appears to be the increase in average Δa (crack growth increment) and a decrease in ΔN (number of cycles to obtain growth) for the composite that is caused by fracturing of Cr_2Nb particles in the crack path. Crack growth rate in the composite is higher also because crack tip strain is lower than for the matrix alloy at the same ΔK_{eff}, which is another indication that ΔN would be decreased for the composite. One reason for the decrease in crack tip strain at the point of crack advance in the composite is the increased level of constraint caused by the intermetallic particles.

Intermetallic Cr_2Nb particles were found to be broken even at very low levels of ΔK, although the area fraction of particles on the fracture surface is less than the volume fraction in the composite. Assuming flaws in the particles are in the range 1-4 μm, the stresses on the particles
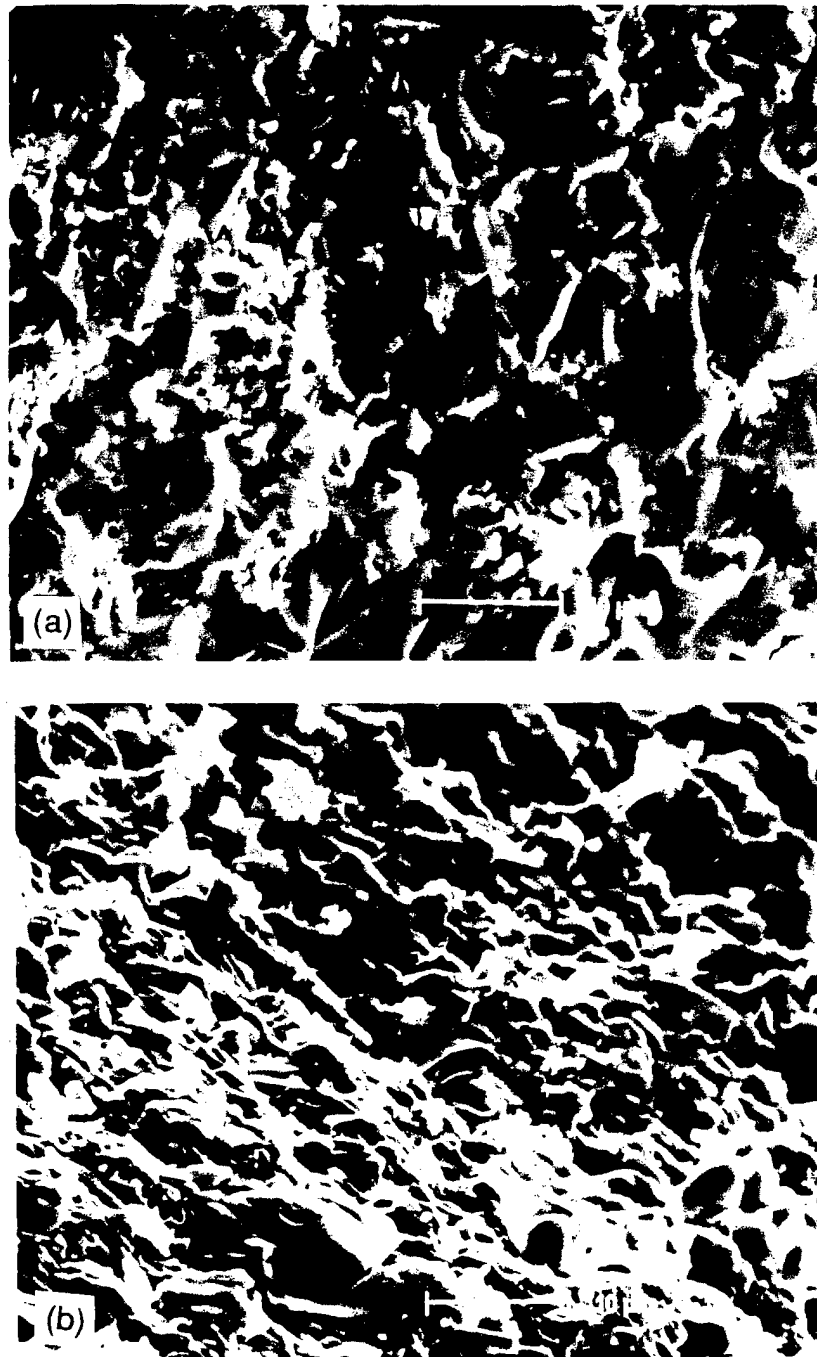
Fig. 43   Fatigue region of the Nb-Cr-Ti composite 93-016 with 22 vol.% Cr$_2$Nb.
Crack growth was from top to bottom.
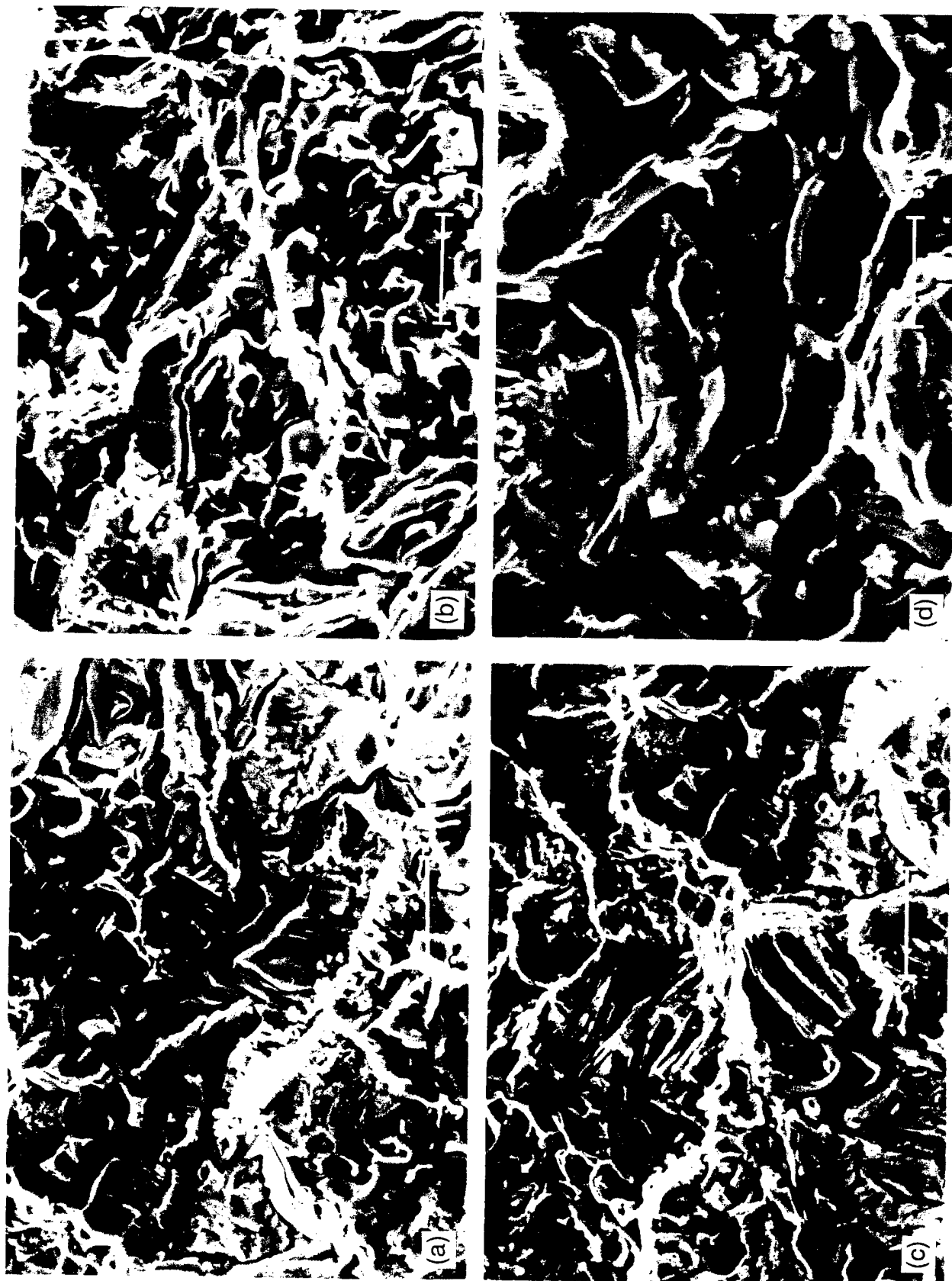
Fig. 44   Fatigue region of the Nb-10Si extruded composite.   Crack growth was from top to bottom.

71
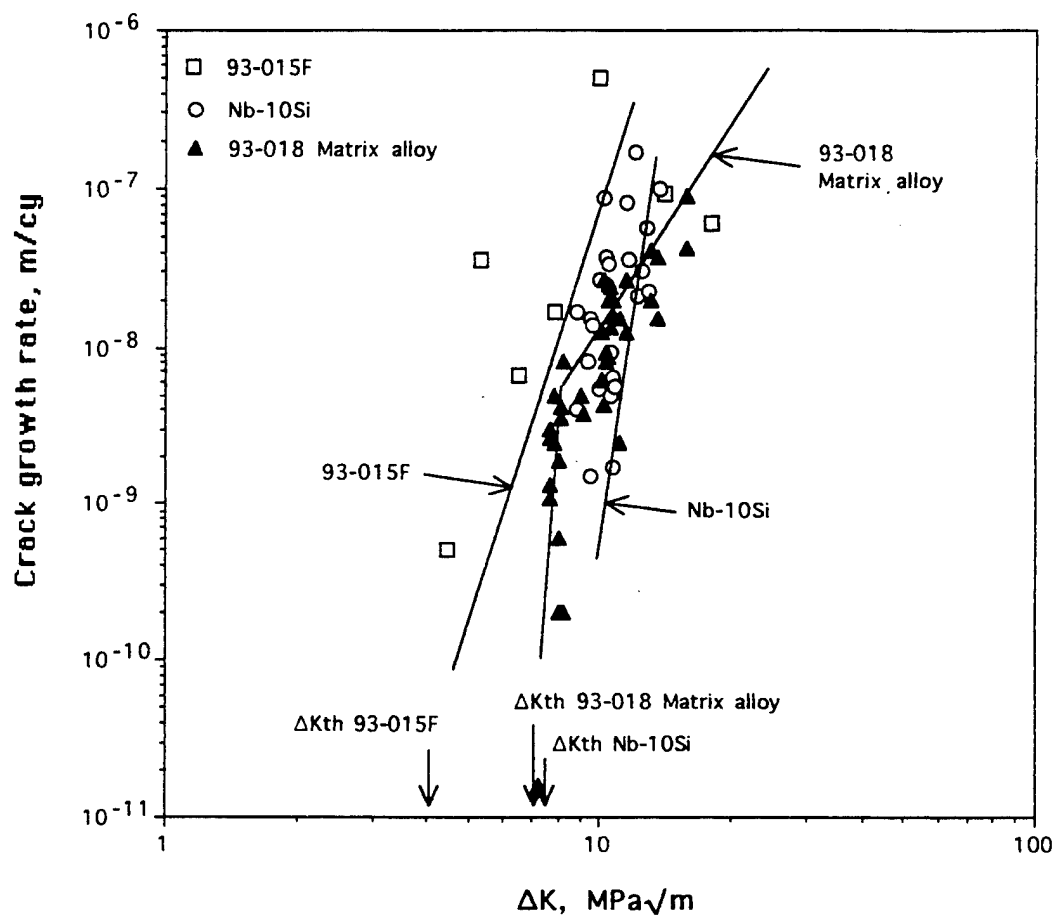
Fig. 45. Comparison of fatigue crack growth rates for the two composites and the matrix alloy.

would be 1500 to 750 MPa which is about the same level as the flow stress, as derived from hardness. But due to the crack, the actual stresses on the particles would be higher near the crack tip. Also, it is not positive that the matrix of the composite 93-015F is the same as alloy 93-018.

To minimize fracture, the intermetallic particles would have to be reduced to $\approx 4 \, \mu m$. If particle fracture was not contributing to crack advance, then the crack would be expected to deflect around them and grow mainly in the matrix alloy, so that crack growth at near ΔK_{th} would be expected to be about the same as for the matrix material, or perhaps somewhat greater, due to the increased elastic modulus of the composite. Particle induced crack deflection near ΔK_{th} in aluminum matrix composites has been demonstrated, and it was found in some instances in this composite. An alternative to decreasing particle size would be to increase toughness of the Cr_2Nb through alloying.

A major difference between the Nb-Cr-Ti composite and nickel-based superalloys is the toughness of the intermetallic. Fracture toughness of Ni_3Al in the Ni matrix of superalloys is reported to be $\approx 100 MPa\sqrt{m}$. In superalloys, the intermetallic phase is also smaller and is usually coherent with the matrix so that slip occurs through the particles and cracks are not deflected around them.

Crack growth rates in the solid solution matrix alloy are similar to pure niobium at near threshold ΔK, but diverge at above about 10^{-7} m/cycle, where the fracture toughness differences between pure Nb and the 93-018 alloy are manifest. Since the electron bonding of 93-018 and Nb are similar, the large difference in fracture toughness cannot be explained on this basis.

A direct comparison of the Nb-Cr-Ti materials with Nb-10Si is difficult because of large differences in composite microstructures. As shown in **Figure 45**, crack growth rates near ΔK_{th} are comparable to those of the 93-018 matrix alloy, but above about 10^{-7} m/cycle, there is divergence, reflecting the differences in fracture toughness. Crack tip strains for this material are more nearly equal to those of the matrix alloy than those of the Nb-Cr-Ti composite. Except at high growth rates, fracturing of intermetallic regions ahead of the crack tip was not found in Nb-10Si. There are several possible reasons for this: (1) the Nb_5Si_3 intermetallic is tougher, (2) the presence of secondary Nb particles within the intermetallic increases toughness, or (3) the size of the continuous intermetallic is small so that inherent flaws are smaller.

I. Fracture Toughness Evaluation

Fatigue-precracked compact-tension specimens were used to characterize the fracture resistance of Nb-Cr-Ti alloys of three different compositions and a Nb-10Si alloy. The Nb-Cr-Ti alloys tested included Nb-13Cr-37Ti (Alloy 93-018), Nb-36Cr-27Ti (Alloy 93-015F), and Nb-29Cr-29Ti (Alloy 93-016). Fracture resistance curves were generated for these alloys by performing fracture testing in a SEM equipped with a loading stage. In the fracture toughness test, the test specimen was loaded to different stress intensity, K, levels. At each K level, the near-tip deformation and fracture behaviors were characterized using high-resolution scanning electron microscopy, and the fracture or toughening mechanism was identified by direct observations. From the near-tip micrographs, the amounts of crack extension at individual K levels were obtained and used to generate the K-resistance curve.

After fracture testing, micrographs of the same crack-tip region under loaded and unloaded conditions, which constituted a pair of stereo micrographs, were analyzed to obtain near-tip displacement and strain data using the machine-vision-based stereoimaging technique developed at SwRI. Additionally, the fracture surfaces were characterized using SEM fractography. The near-tip strain measurements were then correlated with the observed fracture mechanism, K-resistance curve, and the fractographic results to develop a fundamental understanding of the role of the ductile phase in the toughening of the Nb-Cr-Ti in-situ composites.

Figure 46 presents a comparison of the K-resistance curve of a $Cr_2Nb/Nb(Cr,Ti)$ in-situ composite, Nb-36Cr-27Ti, against those of the Nb(Cr,Ti) solid solution alloy, Nb-13Cr-37Ti, and the Cr_2Nb compound, Nb-67Cr. As shown in **Figure 46**, the initiation toughness, K_i, which is the K level at which crack extension occurs, was $1.35\ MPa\sqrt{m}$ for Cr_2Nb. Once started, the crack propagated unstably under a constant K level, leading to a zero slope in the K-resistance curve. In contrast, crack extension in the niobium solid solution alloy, Nb_{ss}, occurred at about $34\ MPa\sqrt{m}$. Subsequent crack extension in the solid solution alloy was stable, as indicated by the rising resistance-curve shown in **Figure 46**. The maximum stress intensity factor at fracture of the solid solution alloy was $88\ MPa\sqrt{m}$. Because of the high toughness, the specimen thickness (3 mm) was insufficient for the plane strain condition and fracture of the solid solution alloy occurred under the plane stress condition. The K-resistance curve for the in-situ composite, which contains about 60 vol. pct Nb_{ss} and 40 vol pct Cr_2Nb, showed a zero slope similar to that observed in the Cr_2Nb compound. The initiation toughness of the composite was about $19\ MPa\sqrt{m}$, compared to $34\ MPa\sqrt{m}$ for the Nb_{ss} alloy and $1.35\ MPa\sqrt{m}$ for Cr_2Nb.
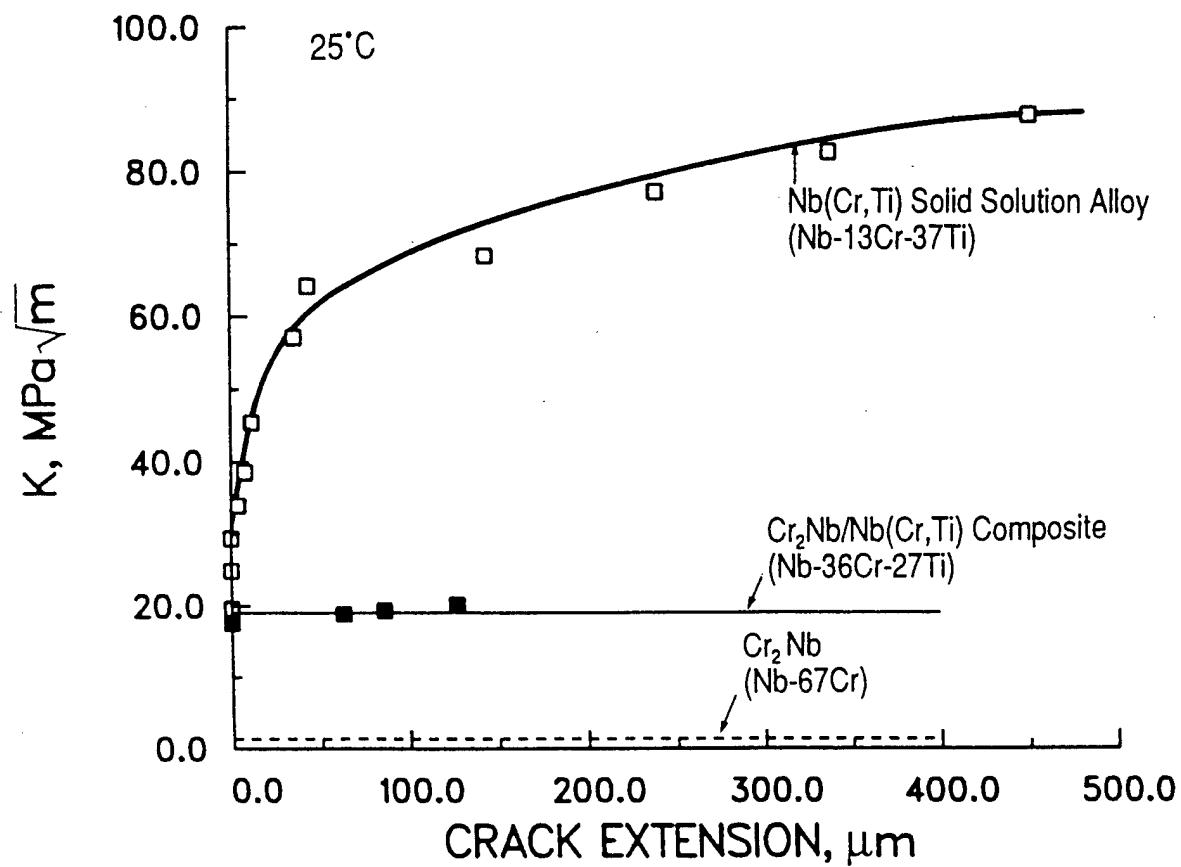
Fig. 46. K-resistance curves of Cr_2Nb, Nb(Cr, Ti) solid solution alloy, and Cr_2Nb(Cr, Ti) *in situ* composite.

The near-tip fracture process observed in the in-situ composite, Nb-36Cr-27Ti, is summarized in **Figure 47**. Initiation of crack growth occurred by cracking of Cr_2Nb particles located directly ahead of the main crack, **Figure 47(a)**. The microcracks linked with each others and with the main crack with relative ease by fracture of the interparticle ligaments, **Figure 47(b)**. Despite the presence of bridging ligaments, the composite exhibited little resistance curve behavior because of a small process zone size and ineffective ligaments that failed too easily. To understand this fracture process, the local strains in the bridging ligaments were obtained using the machine-visioned-based stereoimaging technique. The results, presented in **Figure 48**, indicate that the near-tip Mises effective strain was as high as 22% in the bridging ligaments prior to their fracture. The highly strained region was, however, quite small, indicating that strain was fairly localized.

For comparison with the in-situ composite, the fracture process in the Nb_{ss} alloy is presented in **Figure 49**. In this case, crack extension occurred at about $34\,MPa\sqrt{m}$. **Figure 49** shows that large crack-tip plasticity and crack-opening displacement accompanied crack extension in the solid solution alloy upon increasing K levels from 34 to $64\,MPa\sqrt{m}$. In addition to large crack-tip plasticity, a fine slip line developed ahead of the crack tip at about $64\,MPa\sqrt{m}$. Upon increasing K level, the slip line intensified and developed into a slipband microcrack at $K = 69\,MPa\sqrt{m}$. Back-reflection Laue X-ray diffraction was taken for the near-tip grain prior to the fracture experiment. Using the Laue pattern and a subsequent slip trace analysis, slipband cracking was determined to occur on a (112) plane. Further extension of the microcrack along the (112) slip plane led to linkage of the microcrack with the main crack and the initiation of another microcrack in the neighboring grain at $K = 82\,MPa\sqrt{m}$. Ultimate fracture of the specimen occurred at $87\,MPa\sqrt{m}$. Near-tip strain measurements for the solid solution alloy are currently underway and will be available shortly. Even without the near-tip measurements, it is safe to conclude the Nb_{ss} is relatively tough and ductile when in monolithic form.

The fractographic features observed in Cr_2Nb and in-situ composites are compared in **Figure 50**. Fracture in Cr_2Nb was by cleavage exclusively, as shown in **Figure 50(a)**. Cleavage fracture also occurred in the Cr_2Nb and the Nb solid solution phases in the in-situ composites. **Figures 50(b)** and **(c)** show the cleavage surfaces in composites with continuous Cr_2Nb and Nb_{ss} phases, respectively. **Figure 50(c)** also shows pull-out of a Cr_2Nb particle from the Nb_{ss} matrix, even though most of the Cr_2Nb particles cleaved. The fractographic features of the Nb solid solution alloy, shown in **Figure 51**, are more complex. Despite the high fracture toughness, the
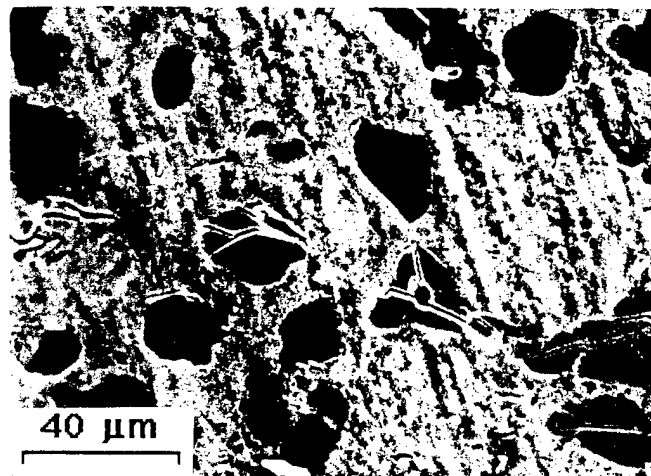
(a)
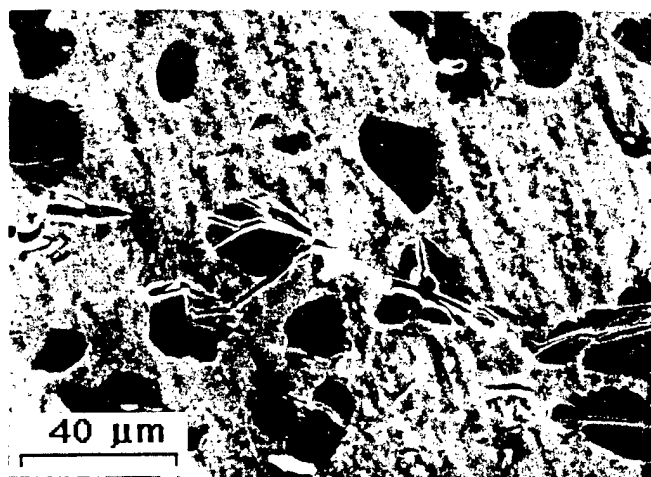
(b)

Fig. 47.   Near-tip fracture process observed in the Cr$_2$Nb/Nb in-situ composite with the Nb-36Cr-27Ti composition.
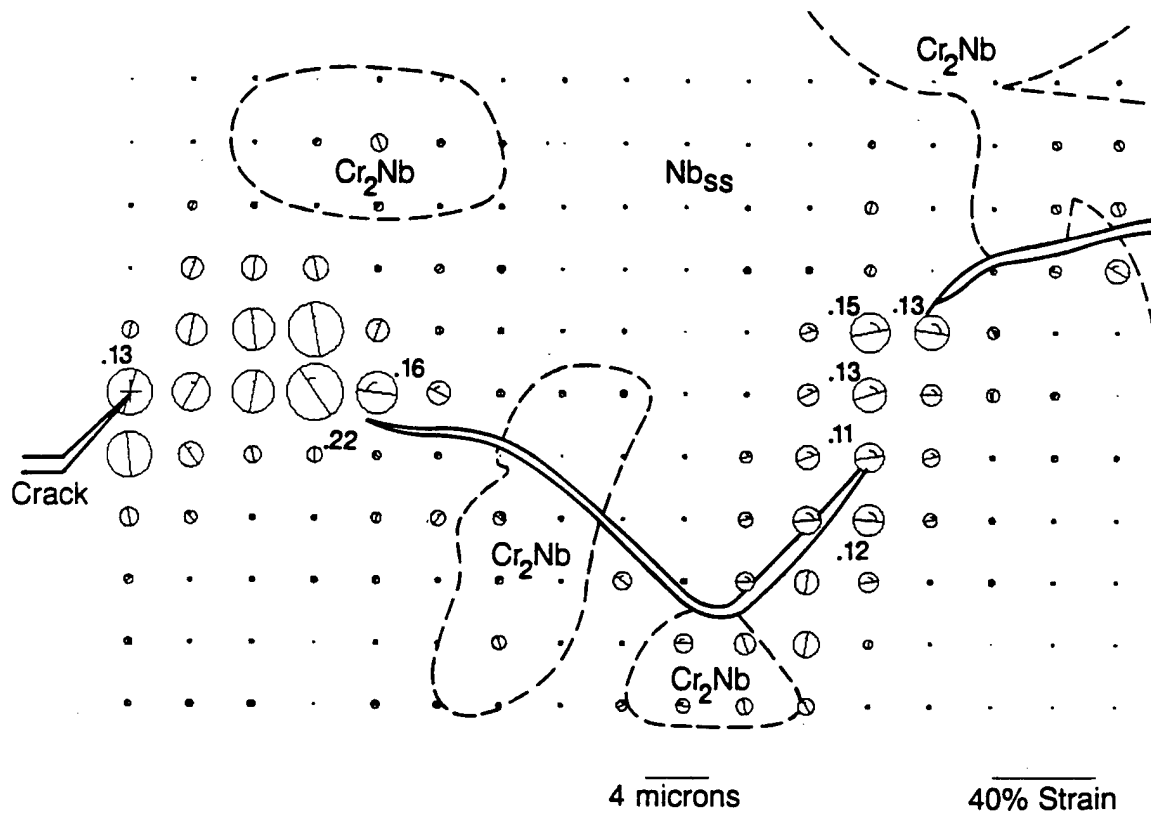
Fig. 48. Local strain distribution in bridging ligaments in the Cr$_2$Nb/Nb in-situ composite (Nb-3Cr-27Ti) tested at K = 19 $MPa\sqrt{m}$ at room temperature.
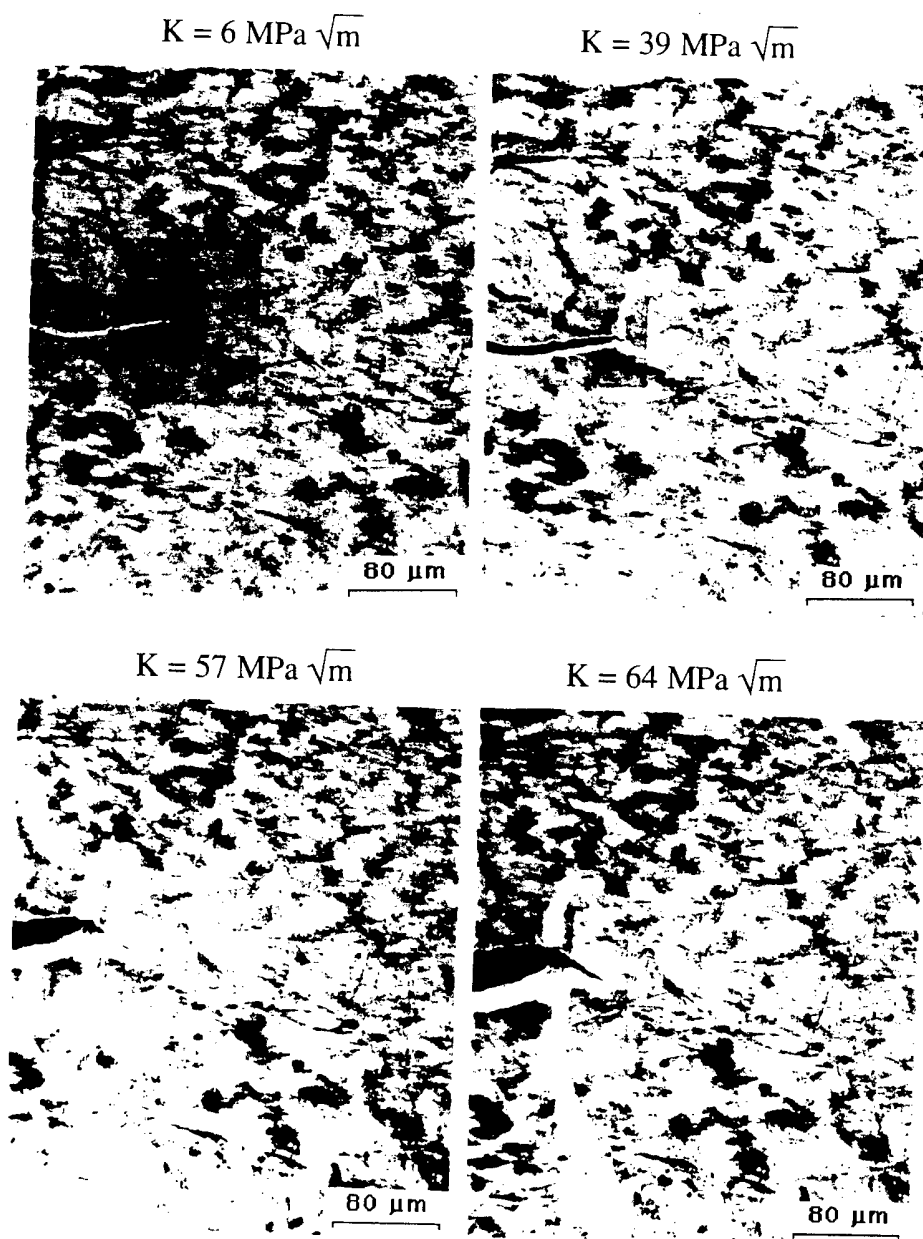
K = 6 MPa √m   K = 39 MPa √m

K = 57 MPa √m   K = 64 MPa √m

80 µm 80 µm

80 µm 80 µm

Fig. 49. Near-tip fracture process observed in the Nb(Cr, Ti) solid solution alloy with the Nb-13Cr-37Ti composition.

K = 68 MPa $\sqrt{m}$ K = 69 MPa $\sqrt{m}$

K = 77 MPa $\sqrt{m}$ K = 82 MPa $\sqrt{m}$
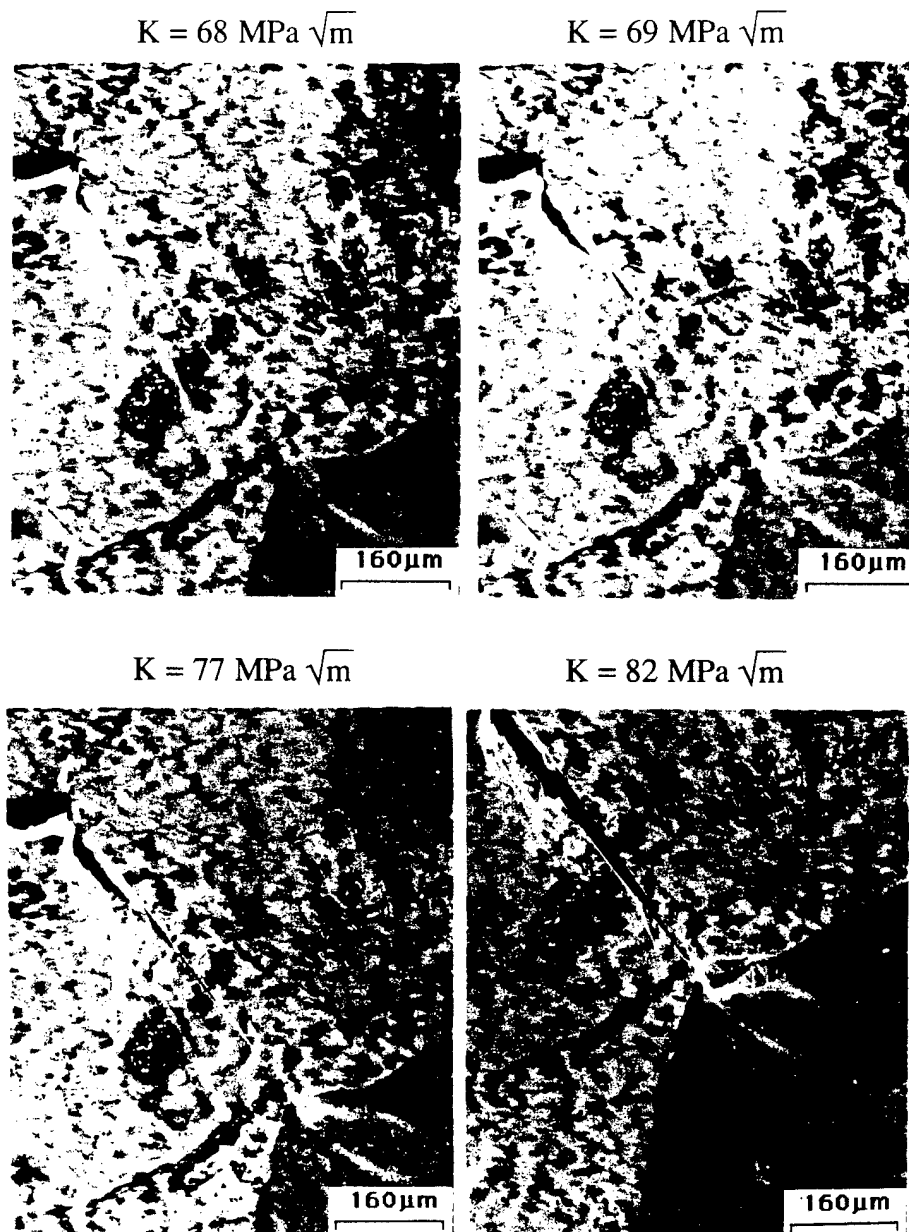
Fig. 49 (continued).   Near-tip fracture process observed in the
Nb(Cr, Ti) solid solution alloy with the Nb-13Cr-37Ti composition.
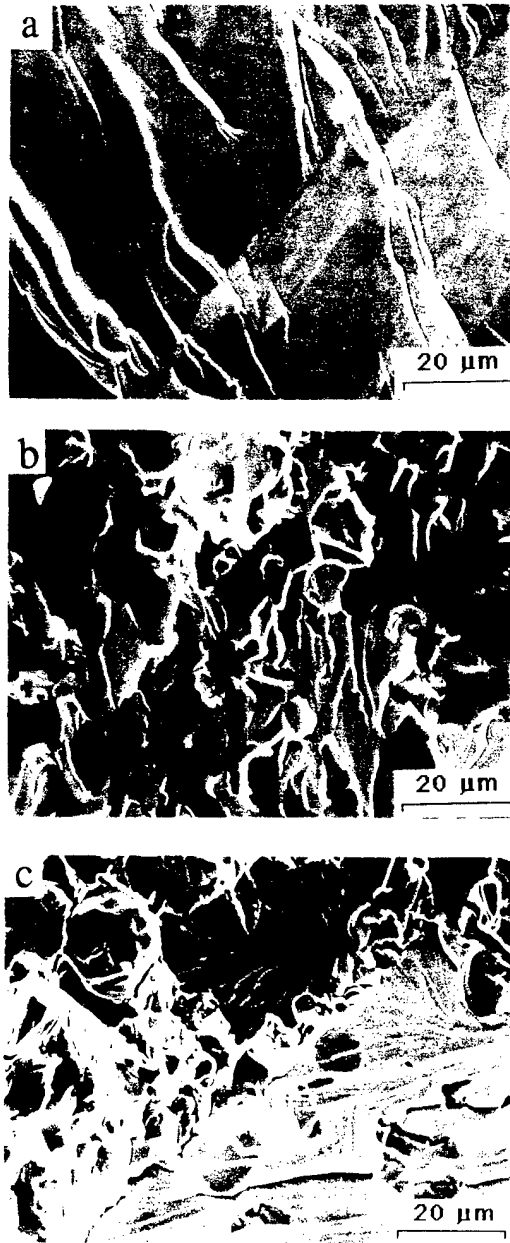
Fig. 50. Cleavage fracture in $Cr_2Nb/Nb(Cr, Ti)$ in-situ composites:
(a) Cr_2Nb (Nb-67Cr), (b) $Cr_2Nb/Nb(Cr, Ti)$ with continuous Cr_2Nb
(Nb-29Cr-29Ti), and (c) $Cr_2Nb/Nb(Cr, Ti)$ with continuous Nb_{ss}
(Nb-36Cr-27Ti).
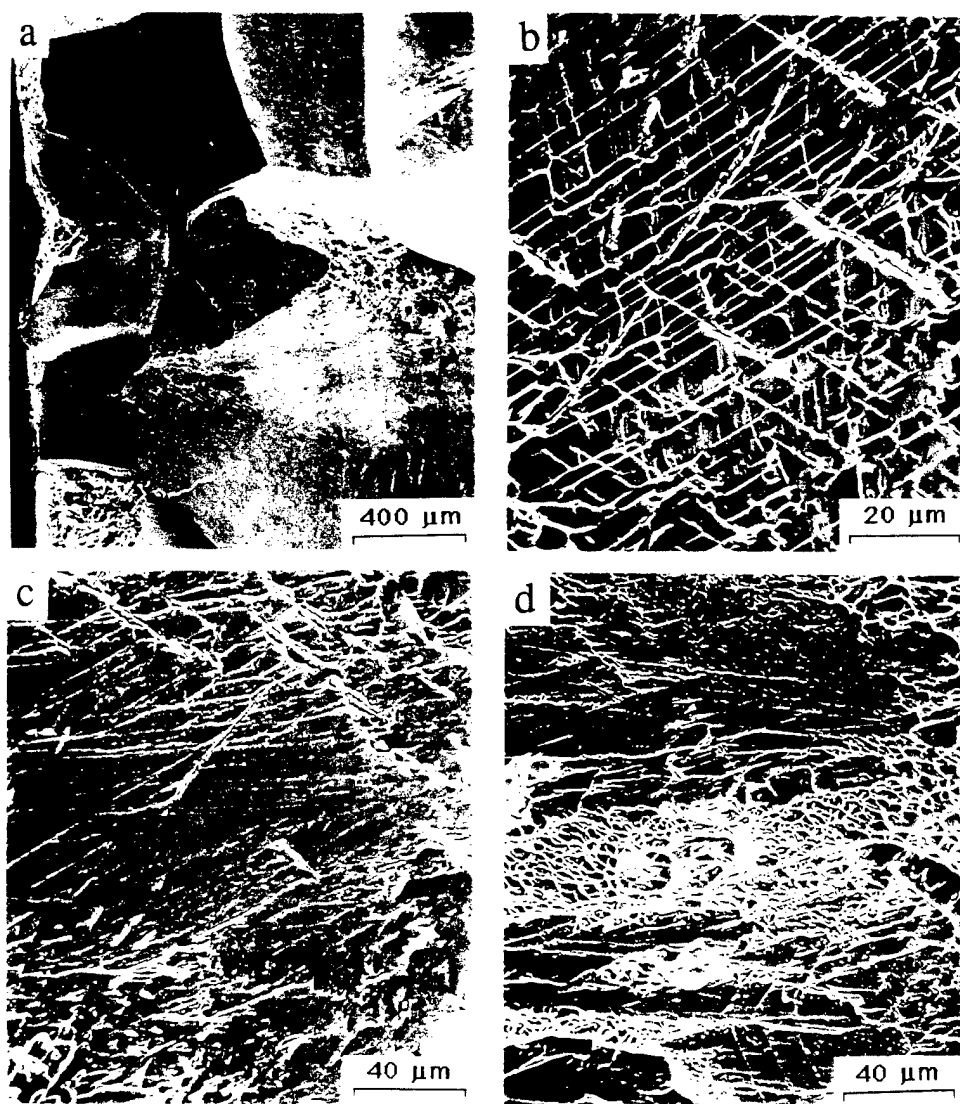
Fig. 51. Fractographic features observed on the fracture surfaces
of the Nb$_{ss}$ alloy, Nb-13Cr-37Ti: (a) low magnification view showing
intergranular facets, (b) slip traces on intergranular facets,
(c) fracture along a slip plane, and (d) dimples on a fractured slip
plane.

Nb solid solution alloy exhibited mostly intergranular fracture, as shown in **Figure 51(a)**. Many of the intergranular facets manifested slip markings, **Figure 51(b)**. Additionally, fracture along slip planes was observed, **Figure 51(c)**. In some cases, the slip planes contained evidence of dimples, as shown in **Figure 51(d)**. All of these fractographic features are different from the cleavage facets observed in the Nb_{ss} matrix in the in-situ composites. Thus, different fracture mechanisms occurred in the solid solution alloy and in the in-situ composites.

The K-resistance curve for the Nb_5Si/Nb in-situ composite, Nb-10Si, is shown in **Figure 52**. The initiation toughness was about 15.5 $MPa\sqrt{m}$. The was some crack-growth toughness due to bridging by the Nb solid solution phase, as shown in **Figure 53**. As in the Nb-Cr-Ti composites, the process zone size in the Nb_5Si/Nb in-situ composite was small and the Nb solid solution ligaments fractured relatively easily. As a result, the amount of ligament toughening instigated by the Nb_{ss} phase was relatively small; the maximum toughness achieved was about 21 $MPa\sqrt{m}$, as shown in **Figure 52**.

The results in **Figures 46** and **52** indicate that the composite microstructure affects both the initiation and crack growth toughness of in-situ composites containing Nb_{ss} as the toughening phase. The influence of the volume fraction of the Nb_{ss} phase on the initiation toughness of the Cr_2Nb/Nb composite was examined by comparison of experimental data with theoretical models developed in this program [17] as well as those in the literature [18]. **Figure 54** shows that the initiation toughness value of the $Cr_2Nb/Nb(Cr,Ti)$ in-situ composite increases with increasing volume fraction of the solid solution phase. The amount of toughness increase is, however, less than that calculated based on either the crack-trapping model [18] or the crack-tip blunting model [17]. The discrepancy between experimental observation and theoretical calculations appears to arise from the development of a high plastic constraint in the solid solution phase by the nondeformable, hard Cr_2Nb phase. The high constraint results in a lowering of the work of fracture for the solid solution phase, and therefore a lower initiation toughness value.

The presence of a high constraint in the solid solution phase of Cr_2Nb/Nb in-situ composite is supported by the fractographic evidence. The Cr_2Nb phase failed exclusively by cleavage fracture in either monolithic or composite form. In monolithic form, the Nb solid solution is ductile and tough, exhibiting a toughness in the range of 34-88 $MPa\sqrt{m}$. The fracture surface exhibits a combination of intergranular fracture, dimpled fracture, and decohesion of slip planes. In contrast, the Nb solid solution phase fails by cleavage when in the composite form. This change in the
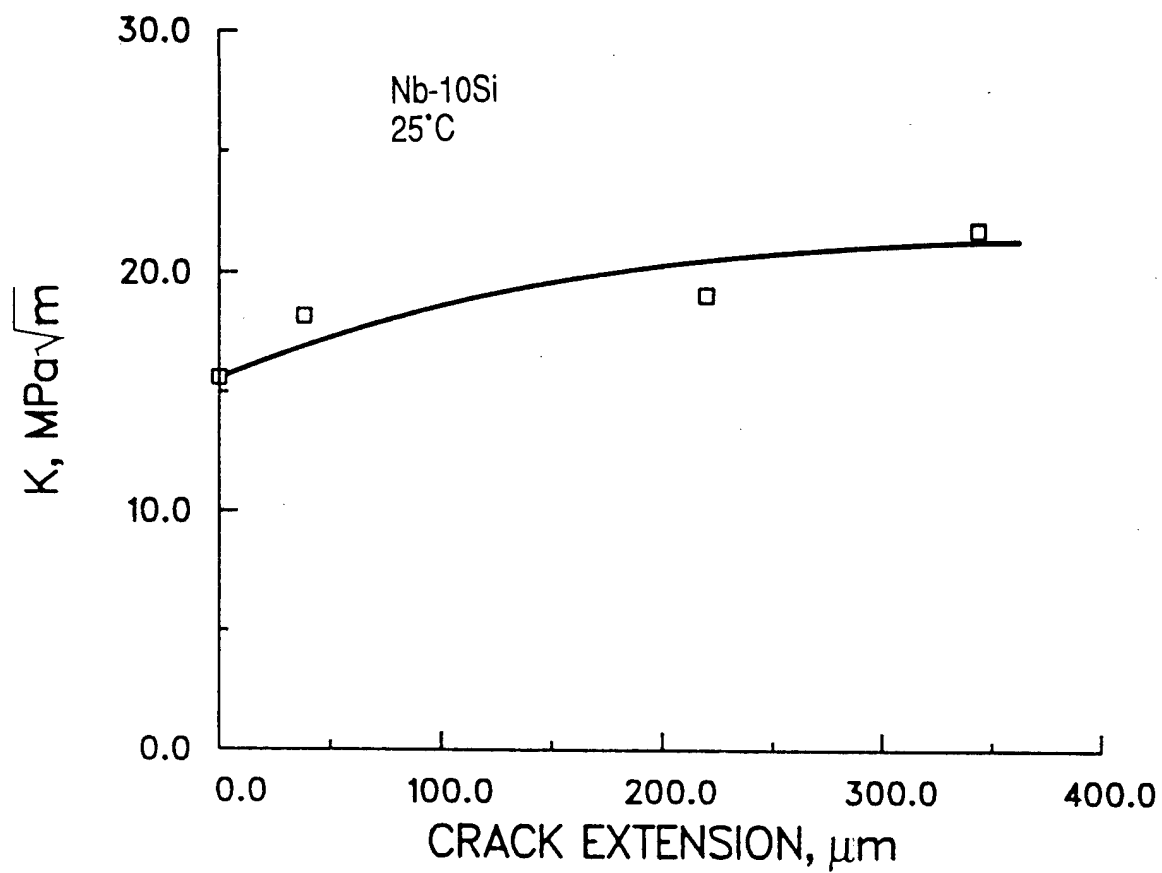
Fig. 52. K-resistance curve for the Nb_5Si/Nb in-situ composite with the Nb-10Si composition.
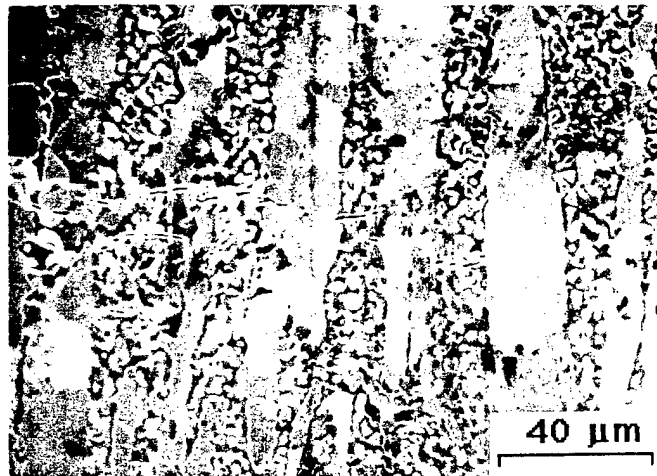
(a)
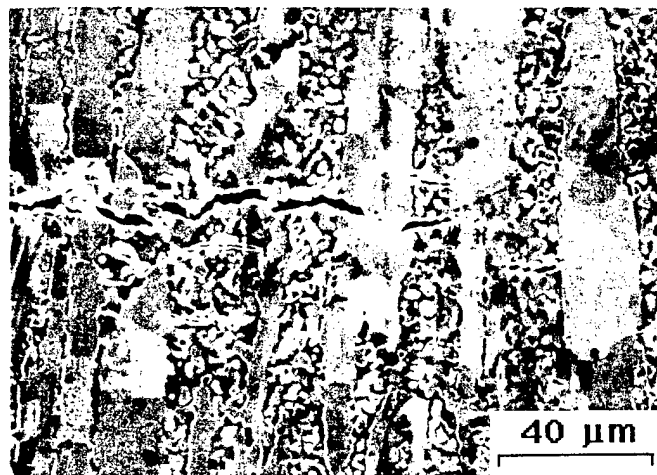
(b)

Fig. 53. Near-tip fracture process observed in the Nb$_5$Si/Nb in-situ composite with the Nb-10Si composition.
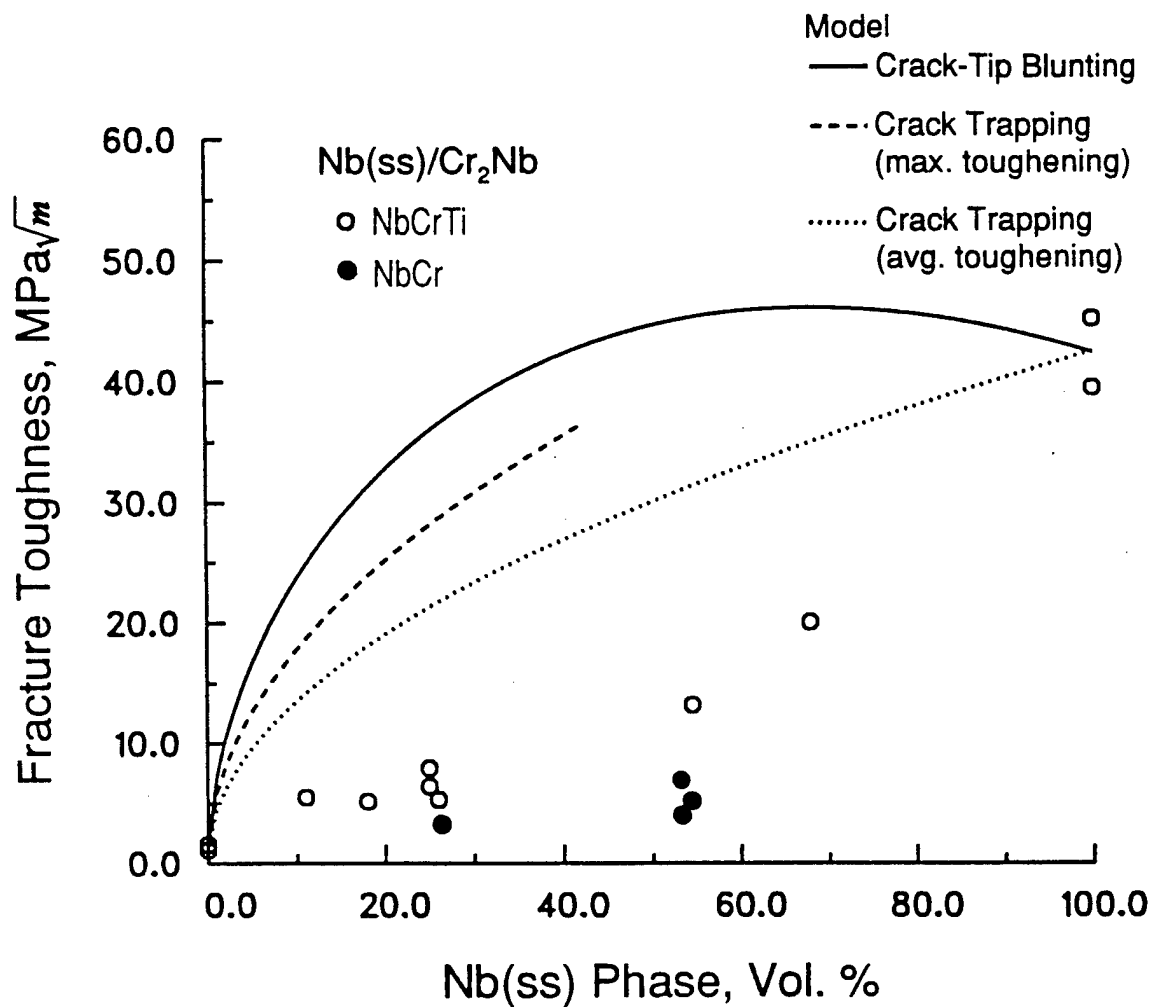
Fig. 54. Comparison of experimental data and theoretical calculations of initiation toughness as a function of volume fraction of the ductile Nb_{ss} phase for $Cr_2Nb/Nb(Cr, Ti)$ in-situ composites.

fracture mode can be explained on the basis that a high plastic constraint developed in the solid solution Nb phase in the composite so that the cleavage mechanism can be attained more easily than the other fracture mechanisms.

III. RECOMMENDATIONS FOR FURTHER ALLOY DEVELOPMENT

The damage tolerance of the composites would be greatly increased if the fracture toughness of the intermetallics was higher. Also, if the size intermetallic particles was reduced, they would fracture less frequently, thereby causing fatigue crack growth to occur through the tougher matrix material. Thus, additional development of these materials should concentrate on increasing intermetallic toughness and decreasing particle size. The interfaces between intermetallic and matrix were found broken very infrequently, indicating adequate interfacial strength.

The increase in the local level of matrix constraint caused by intermetallic particles in these composites can only be offset by increases in the toughness of the matrix alloys, which, presumably, could be attained by additional alloying.

The generally poor oxidation resistance of niobium has been recognized as problem in applications of niobium alloys, and significant progress has been made in increasing oxidation resistance through alloying. As development of oxidation resistance progresses, assessment must be made of the effects of alloying additions on fracture resistance. Preliminary assessment is encouraging in this respect because oxidation resistance has been shown to increase with additions of chromium, silicon and titanium. There are some indications that aluminum additions may cause fracture resistance problems, but this needs further exploration.

IV. SUMMARY OF FATIGUE AND FRACTURE RESEARCH ON TiAl-BASED ALLOYS

A. Introduction

The initial thrust of this project was on the micromechanics of fatigue and fracture toughness of two phase alloys TiAl and Ti_3Al, and most of the research effort was on materials heat treated to be fully lamellar. The research results attained on these alloys has been previously reported in either AFOSR annual reports or published in journals and conference proceedings. Because the results have been published and the length of this Final Report, only a summary is presented here.

B. Fatigue Crack Initiation

Fatigue crack initiation in lamellar materials was carefully investigated using rotating beam specimens so that R = -1 [19]. It was found that stresses approximating yield were required to initiate fatigue cracks within a million cycles, making the stress-cycles to failure curve very shallow — a slope of approximately 0.05 was determined for this relationship. Slip was detected after only a few cycles at near-yield stress within a few of the lamellar colonies. However, the magnitude of slip did not increase with additional cycles, as would be expected from conventional alloys; instead, the slip offsets in those colonies stabilized while slip spread to additional colonies. Only if stress was increased could slip could be induced within previously deforming colonies. When fatigue cracks finally initiated, they did not start within the deforming lamellar colonies. Instead, cracks initiated at what were thought to be forging related defects that occurred during materials processing. The sites consisted of small regions of bent and contorted lamellae surrounded by normal lamellar regions.

Slip development was observed through examination of plastic replicas made periodically from the specimen surface. Optical and atomic force microscopy (AFM) were used to make these observations. A new technique was developed to make AFM measurements from replica. This allowed the AFM to be used on non-flat specimen surfaces that could not otherwise be studied. Use of the AFM was found to be essential because the resolution of that device matched the spatial scale of the deformation. A typical AFM image obtained from a replica of the specimen surface is shown in **Figure 55**, where adjacent lamellae are seen to have slipped relative to one another. There appears to be little slip within each lamella, with most of the deformation within the boundary between adjacent lamellae. The scratches are not offset, indicating that interlamellar slip was almost entirely out of plane.

From the results obtained, it was thought that the misfit dislocation structure within lamellar boundaries that has been found by transmission electron microscopy allowed slip to occur during initial loading. But, subsequent cycles caused these dislocations to be stopped by impenetribule barriers; i.e., the material work hardened and did not form the usual persistant slip bands.
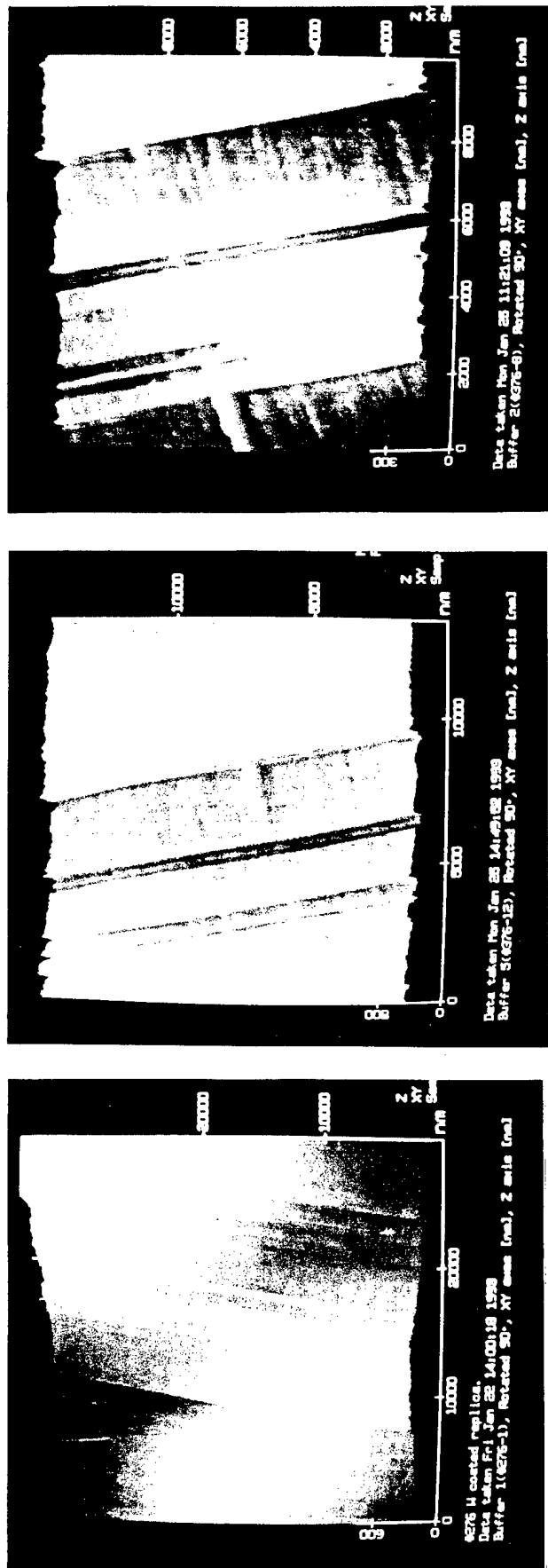
Fig. 55 Fully lamellar TiAl-based alloy. Atomic force microscope image of a coated plastic replica of the surface of a specimen cyclically loaded to 400 MPa for 6.7×10^4 cycles. Slip is seen to have been confined to the interfaces between lamellae.

C. Fatigue Crack Growth

Once fatigue cracks initiated, they were observed to grow at stress intensity factors below those required to grow large cracks, **Figure 56** [20]. This is the same result as found for many other materials. Small cracks in the lamellar TiAl-based alloy also grew faster than large cracks in the region of overlapping stress intensity factor. However, small crack growth equaled that of large cracks when the cracks were still physically small (about 0.5 mm).

The slope of the da/dN vs ΔK curve for large fatigue cracks was found to be ≈ 5, which is comparable to results for aluminum and titanium alloys [20]. Boundaries between lamellae were found to arrest fatigue cracks when crack growth was perpendicular to the boundaries. Crack growth was approximately twice as fast when growth was parallel to the lamella planes. Fatigue cracks were observed within the SEM while growing at 800°C. The events related to crack extension were found to be very similar to those observed at ambient temperature.

D. Fracture Toughness

Fracture studies of TiAl alloys has been concentrated on experimental studies and micromechanical modeling of the influence of microstructures on fracture resistance and tensile ductility. Since many of these works have been published [20-28], only a highlight of the important results is presented. Details of the experimental procedures and model development will be referred to the original publications.

Research obtained from this program has demonstrated that the fracture behavior of TiAl alloys is best described in terms of a fracture resistance curve which depicts the fracture resistance, usually in terms of the stress intensity factor, as a function of amounts of crack extension [21,28,29]. The K-resistance, K_R, curves for a wrought TiAl alloy heat-treated to either a lamellar or a duplex microstructure obtained in this program are presented in **Figure 57** [28,29]. In a K_R curve, the onset of crack extension is often referred to as the initiation toughness, K_i, which also corresponds to K_{IC} when the plane strain condition prevails. Once crack extension commences, crack growth can proceed stably or unstably depending on material's resistance against crack growth or tearing. A brittle material will undergo crack advance under an essentially constant K. This fracture behavior was observed in the duplex material, as shown in **Figure 57**. In contrast, the lamellar microstructure behaved in a more ductile manner exhibiting tearing resistance and increasing fracture resistance with increasing crack extension. The maximum stress intensity, K_S, in the K_R-curve may be referred to as the crack growth toughness. Compared to the duplex microstructure, the lamellar microstructure exhibits a higher initiation toughness, a more stable
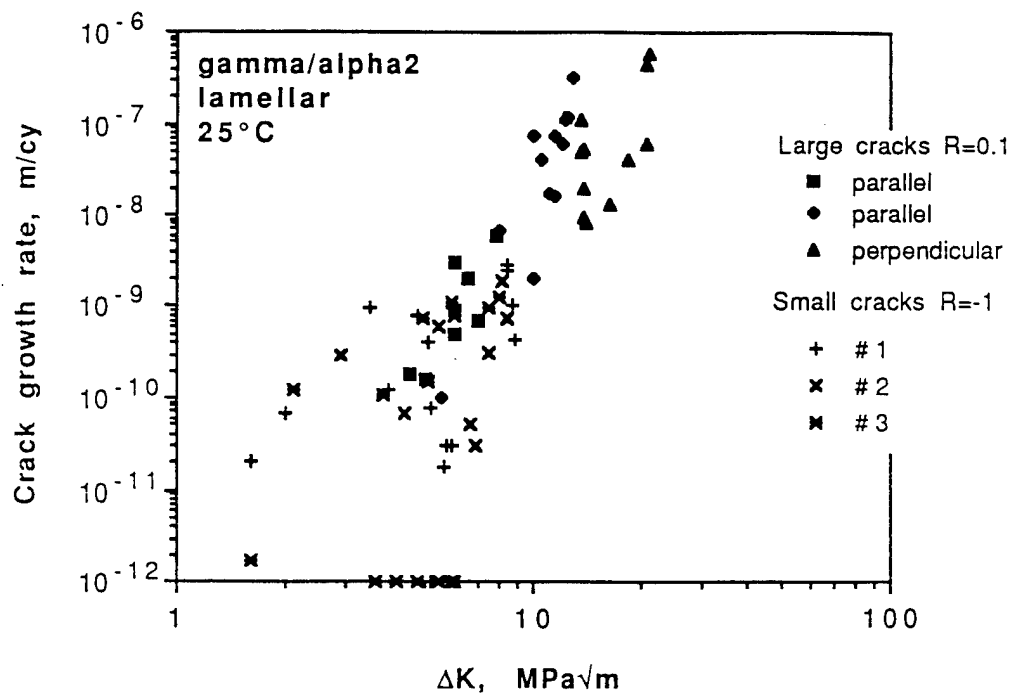
Fig. 56. Fatigue crack growth rates for small and large cracks in a fully lamellar TiAl-based alloy.
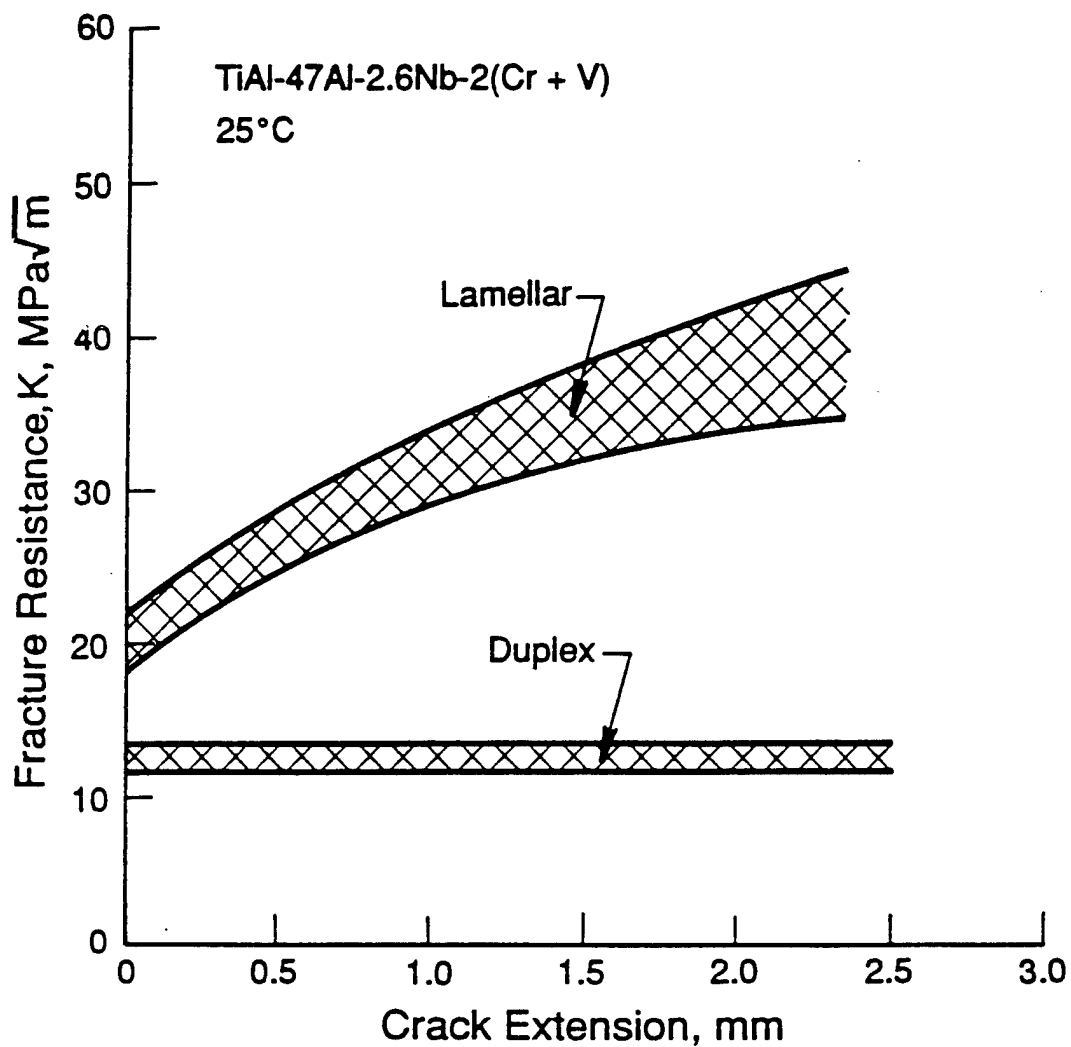
Fig. 57. Comparison of the K-resistance curves of a TiAl-alloy with the lamellar and duplex microstructures. The lamellar microstructure exhibits higher initiation and crack growth toughness than the duplex microstructure.

crack growth behavior, and a higher crack growth toughness as signified by the rising K-resistance curve. In contrast, the duplex material shows little fracture resistance above the initiation toughness.

Considerable efforts have been made to identify the toughening mechanisms responsible for the different resistance-curve behaviors observed in TiAl-alloys [23,24]. Crack-tip strain measurements have shown that the lamellar microstructure exhibits a higher initiation toughness because the microstructure is inherently more ductile and can sustain a higher effective strain near the crack tip than the duplex microstructure [30]. **Figure 58** shows a comparison of the Mises effective strain near the K_{IC} levels, which are 11 and 16 MPa$\sqrt{m}$ for the duplex and lamellar microstructure, respectively.

Both direct observation in SEM and sectioning of unfractured specimens have revealed that the formation of intact ligaments in the crack wake, **Figure 59**, are responsible for the resistance-curve behavior observed in the lamellar microstructure [21,23,24,26]. These crack-wake ligaments, which are formed as the result of the crack deflection and the formation of noncoplanar microcracks ahead of the crack tip, leads to an enhancement in the fracture toughness because they lower the near-tip stress intensity factor [26,27] and must be fractured for total separation of the crack surfaces to occur. The deformation and fracture of these ligaments usually occur by shear at multiple sites, and the toughening effect of these ligaments has been referred to as shear ligament toughening [31]. This toughening mechanism has been modeled in this program using a micromechanical approach. The modeling effort has revealed that the toughening achieved by the crack-wake shear ligaments can be described by [31]

$$K_C = \left\{ (1 - v_l)K_i^2 + \frac{v_l l E \tau_i \gamma_i^*}{1 - v^2}\left[1 + \left(\frac{L}{l}\right)\tan\phi \right] \right\}^{1/2}$$

(3)

which indicates that the amount of toughening achieved in a matrix with an initiation toughness, K_i, and Young's modulus, E, increases with the volume fraction, v_l, and the width, l, of the shear ligaments in the crack-wake, as well as the crack deflection angle, ϕ, and the projected crack length, L, to ligament width ratio, L/l. Toughness enhancement is provided by redundant shear deformation and fracture of the ligaments at a fracture stress in shear, τ_f, and a critical shear strain, γ_i^*. A comparison of the experimental data and model calculation, shown in **Figure 60**, indicates that fracture toughness of lamellar TiAl alloys increases with the volume fraction, v_l, and width, l, of the shear ligaments in the crack wake [26].
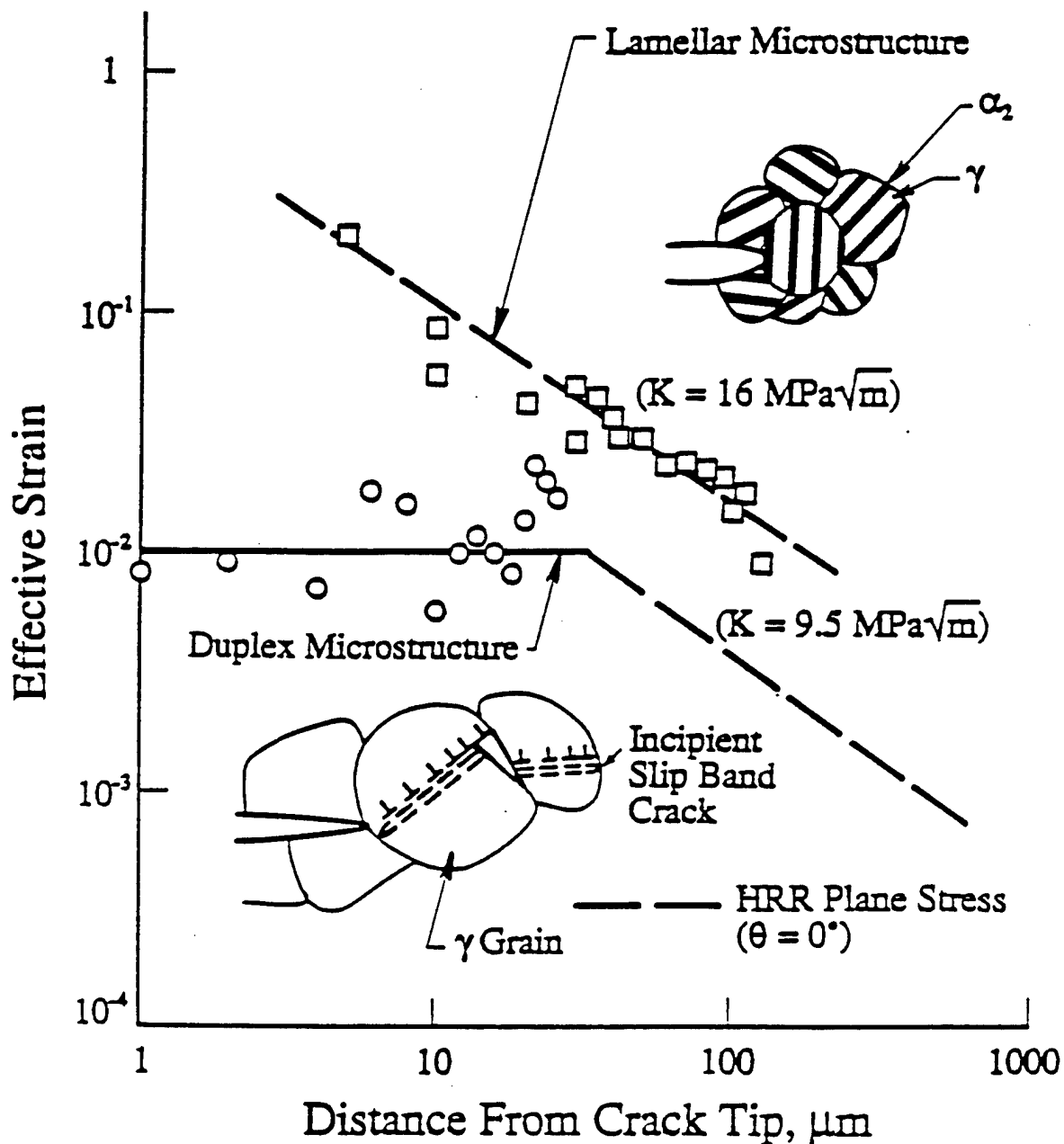
Fig. 58. Comparison of near-tip fracture process and strain distribution in the duplex and the lamellar microstructures of the two-phase TiAl-alloy, Ti-47Al-2.6Nb-2(Cr + V), at 25°C.

Fig. 59. A shear ligament under load in a lamellar TiAl alloy.

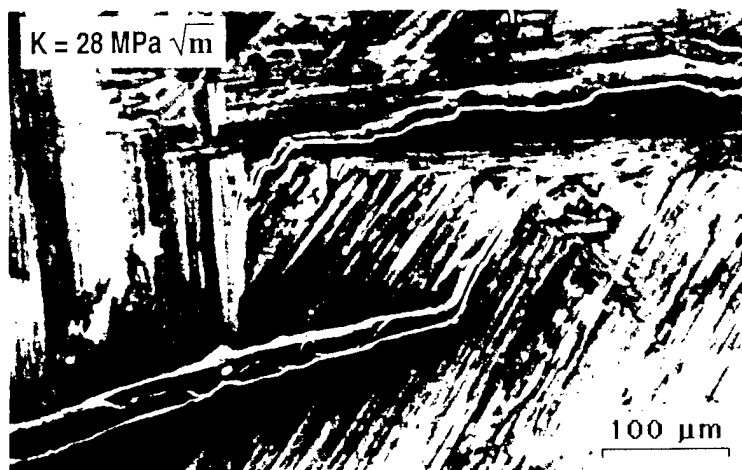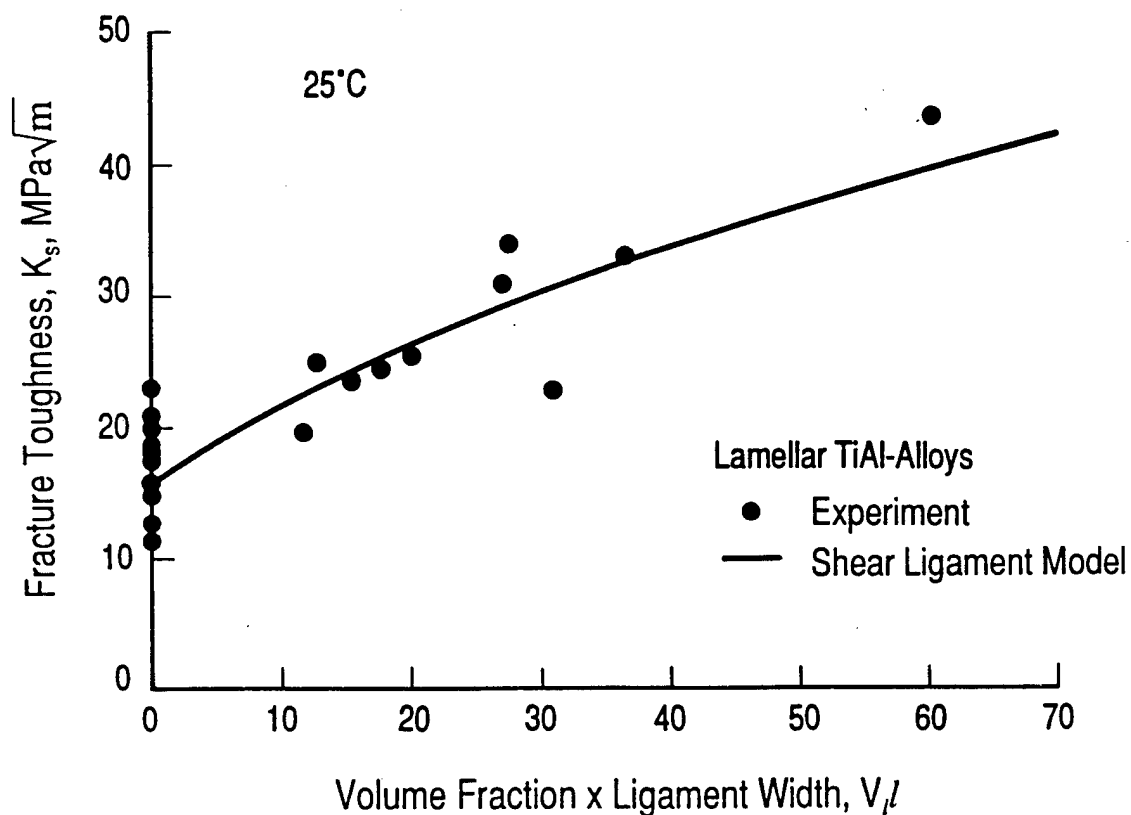Fig. 60. Comparison of the shear ligament model against experimental data of fracture toughness, K_s, as a function of the product of the volume fraction (v_l) and width (l) of the crack-wake ligament.

While crack-wake shear ligaments are responsible for the maximum fracture resistance, the initiation toughness, K_i, at the onset of stable crack growth is dictated by blunting of the crack tip by the α_2 and γ platelets within the lamellar colonies. The consequence is that the K initiation toughness, K_i, increases with increasing volume fraction of lamellar grains. This microstructural dependence has been modeled in this contract by considering the lamellar colonies as ductile grains dispersed in a matrix of the more brittle equiaxed γ grains. Using this approach, the initiation toughness for TiAl-alloys containing a microstructure of lamellar colonies and equiaxed γ grains is given by [32]

$$K_i = K_m[1 + V_\beta (\Sigma - 1)]^{\frac{n-1}{2n}} [1 + V_\beta (\Lambda - 1)]^{\frac{n+1}{2n}} [1 + V_\beta(\zeta - 1)]^{\frac{n+1}{2n}} \qquad (4)$$

where Σ, Λ, and ζ are the yield stress, fracture strain, and Young's modulus of the ductile phase, β, normalized by those of the matrix phase; K_m is the K_{IC} value for the matrix phase, which are the equiaxed γ grains; n is the inverse of the strain hardening exponent; V_β is the volume fraction of the ductile phase, which is the lamellar colonies. Application of the crack-tip blunting model [28] to predicting the initiation toughness of a XD^{TM}-processed TiAl alloy [33] indicates that the initiation toughness increases with increasing amounts of lamellar grains.

The crack-tip blunting and shear ligament toughening models have also been combined in this program to form a general framework by which one can predict maximum toughness attainable in a TiAl-alloy as a function of the amount of lamellar grains if the volume fraction and width of shear ligaments formed in the crack wake are known [29]. Measured values of the volume fraction of the crack-wake ligaments have been used in conjunction with Eqs. (3) and (4) to calculate the maximum fracture toughness. **Figure 61** shows a comparison of the model calculation against experimental data for Ti-47Al-(2.3-2.6)Nb-(1-1.6)Cr-1V alloy. The model calculation reveals that relatively high initiation and crack growth toughness can be expected in TiAl-alloys with a microstructure containing a high volume fraction of lamellar grains with fine ($< 2 \mu m$) lamellae spacing, as observed experimentally. For fully lamellar materials, the initiation toughness is 20 MPa$\sqrt{m}$, which originates mostly form crack-tip blunting and plastic work dissipation in the plastic zone. Additional toughness (about 15-25 MPa$\sqrt{m}$) comes from plastic dissipation in the crack-wake ligaments.

Fig. 61. Comparison of calculated and experimental values of initiation (K_i) and crack growth (K_s) toughness as a function of volume percent of lamellar grain in a TiAl-alloy containing mixtures of equiaxed γ and lamellar α_2 + γ colonies.
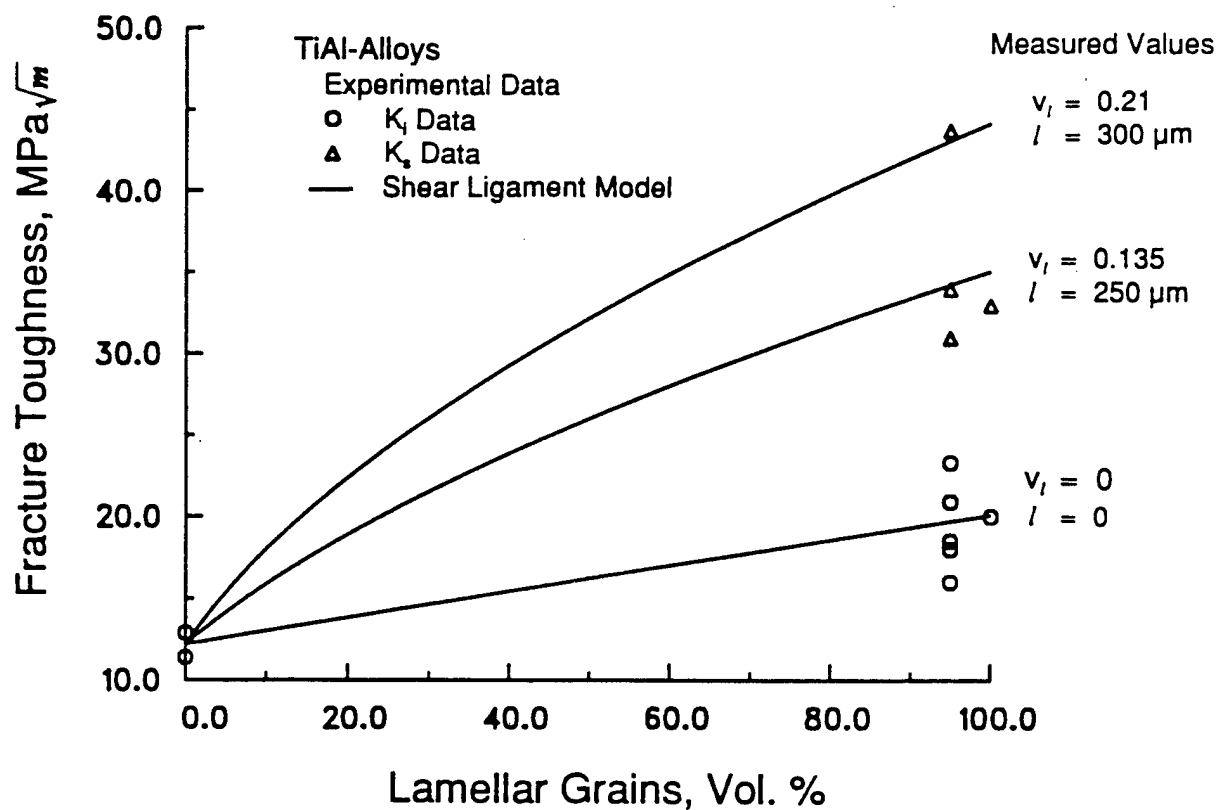
In addition to volume fraction, the lamellae width (or spacing) is also an important factor influencing the fracture resistance of large-grained material [24]. Both the initiation and crack growth toughness increased with decreasing lamellar spacing [24] in a manner similar to the Hall-Petch relation [34,35]. The lamellae spacing influences initiation and crack growth toughness values by affecting the ligament width and the propensity for ligament formation [24,26].

The crack growth toughness, K_S, has also been found to increase with the colony size due to increasing ligament width. However, for large-grained material (> 600 μm), the crack growth toughness is mostly controlled by the lamellae spacing because the crack-tip plastic zone is less than the colony size [24].

The dependence of the initiation toughness, K_{IC}, on grain size is also complicated. Compilation of experimental data of initiation toughness from this program and those in the literature [36], shown in **Figure 62**, indicates that K_{IC} increases slightly with increasing grain size [29]. In **Figure 62**, the result for the lamellar material of the G1 alloy, Ti-47Al-2.6Nb-1Cr-1V, suggests that the initiation toughness increases with grain size according to a power-law with an exponent of 0.183. The K_{IC} data for the G1 alloy can be described as [29]

$$K_{IC} = K_o \left\{ \frac{d}{d_o} \right\}^{\delta} \tag{5}$$

where δ has a value of 0.183, and K_o is the K_{IC} at the reference grain size, d_o, which is taken to be 1 μm. The K_{IC} values for both the duplex and lamellar microstructures have been fitted to a single equation because of the lack of experimental data in the 30-60 μm grain size range for the lamellar microstructure. The data for the G8 alloy, Ti-47Al-2.3Nb-1.6Cr-1V, however, do not appear to exhibit the same grain size dependence. The lack of correlation for the G8 alloy is due to variations in the lamellae spacing. The data base for the K5 alloy [36] is still limited, but exhibits a trend similar to the G1 alloy. The overall trend of the experimental data in **Figure 62** is that the K_{IC} value decreases slightly with decreasing grain size, when the effect of lamellae spacing is small or absent.

E. Tensile Ductility

Tensile deformation of current TiAl alloys at ambient temperature is dominated by fracture that terminates deformation at the peak load prior to the onset of necking or plastic instability [37]. The tensile ductility of TiAl alloys is generally in the range of 1-4% [36], depending on the microstructure. The duplex microstructure usually exhibits a higher tensile ductility than the lamellar microstructure, despite a lower fracture toughness [30]. This observation has led Chan
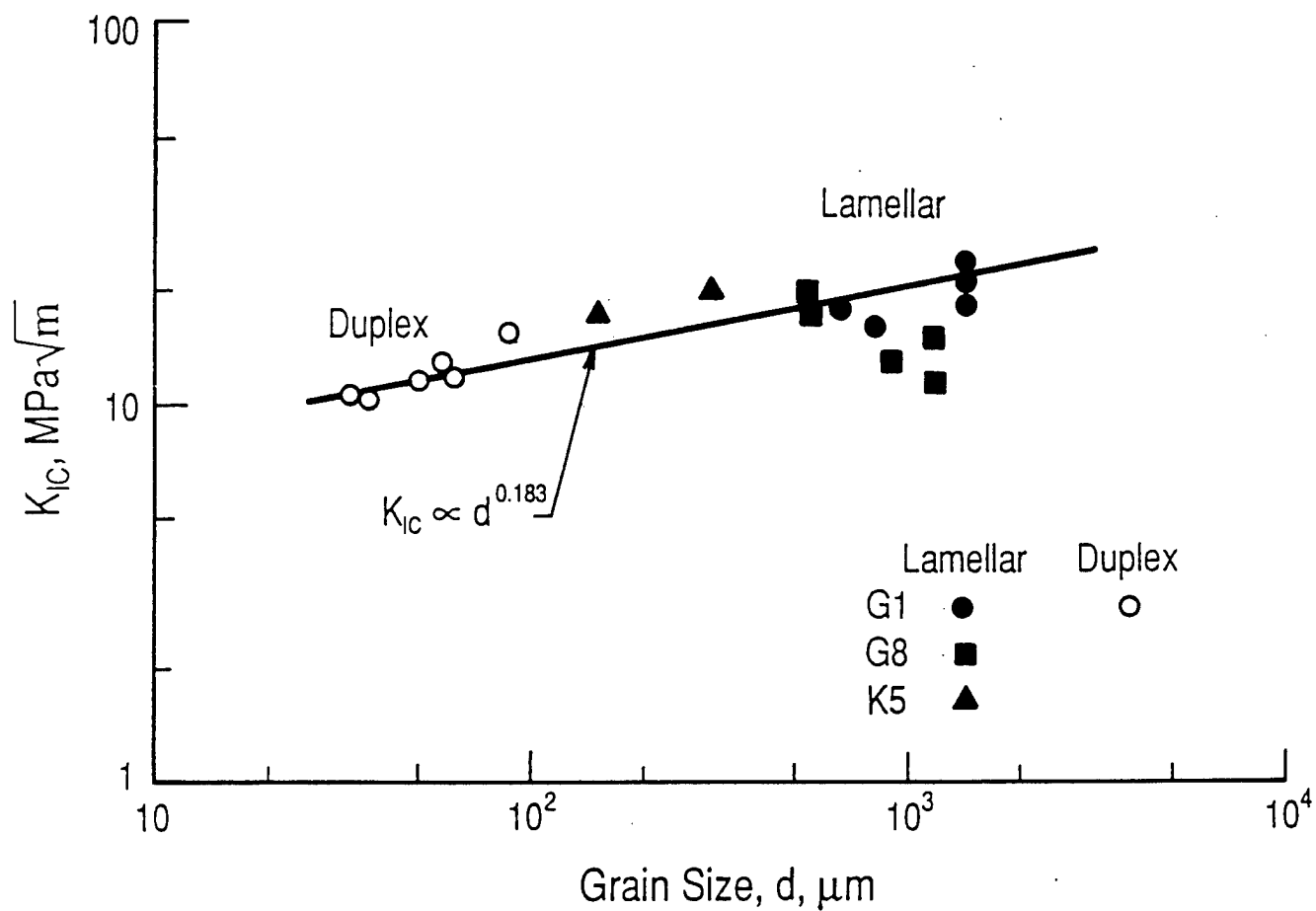
Fig. 62. Increase of initiation toughness, K_{IC}, with increasing grain size. Experimental data for alloy G1 and G8 are from Chan and Kim [24], while those for K5 are from Kim [36].

and Kim [30] to suggest that tensile ductility and fracture toughness in TiAl alloys are inversely related. **Figure 63** shows a compilation of both experimental data both from this program and from Y-W. Kim [22], which indicates that an inverse relationship between plastic elongation and initiation toughness, K_{IC}, exists in TiAl alloys. A similar inverse relationship also exists between plastic elongation and crack growth toughness, K_S, as reported earlier [30].

The origin of the inverse relationship between tensile ductility and initiation toughness, K_{IC}, arises from opposite dependence of these parameters on grain size. **Figure 63** shows that the plastic elongation of TiAl alloys increases with decreasing grain size, which is opposite to that observed for initiation toughness in **Figure 62**.

The relationships between tensile ductility, initiation toughness, and grain size have been explained in terms of a fracture-based tensile ductility model [37,38], which was previously developed in this program by considering the conditions for crack instability in a material that exhibits a resistance-curve fracture behavior. In this model [37,38], a tensile specimen containing an internal penny-shaped microcrack within a grain is subjected to an external stress. The length, 2a, of the penny-shaped microcrack is assumed to be the average grain diameter, d. Through a J-integral analysis, the stress intensity factor of the microcrack was calculated upon increasing external stresses and strains. The tensile specimen was considered to fail when the stress intensity factor reached the K_{IC} value, and the corresponding externally applied nominal plastic strain value was taken to be the plastic elongation.

The plastic elongation was also calculated as a function of the grain size using the tensile ductility model and the material constants for the lamellar material of the G1 alloy [37]. Shown as the solid line in **Figure 64**, the calculated result is in good agreement with the experiment data [22,34]. The important implications of these results are [29]: (1) tensile ductility is limited by a microcrack-dominated fracture process; (2) plastic elongation increases with K_{IC}, but decreases with increasing grain size; and (3) increasing the grain size leads to an increase in the K_{IC}, but a decease in plastic elongation, i.e., an inverse relationship between initiation toughness, K_{IC}, and plastic elongation, as shown in **Figure 63**.

The inverse relationship between K_{IC} and plastic elongation is an undesirable characteristic for TiAl alloys. It exists because the ductility limiting process in TiAl alloys at ambient temperature is the instability of microcracks that are nucleated in the microstructure during tensile deformation. To further improve tensile ductility, one must develop a means to (1) increase the
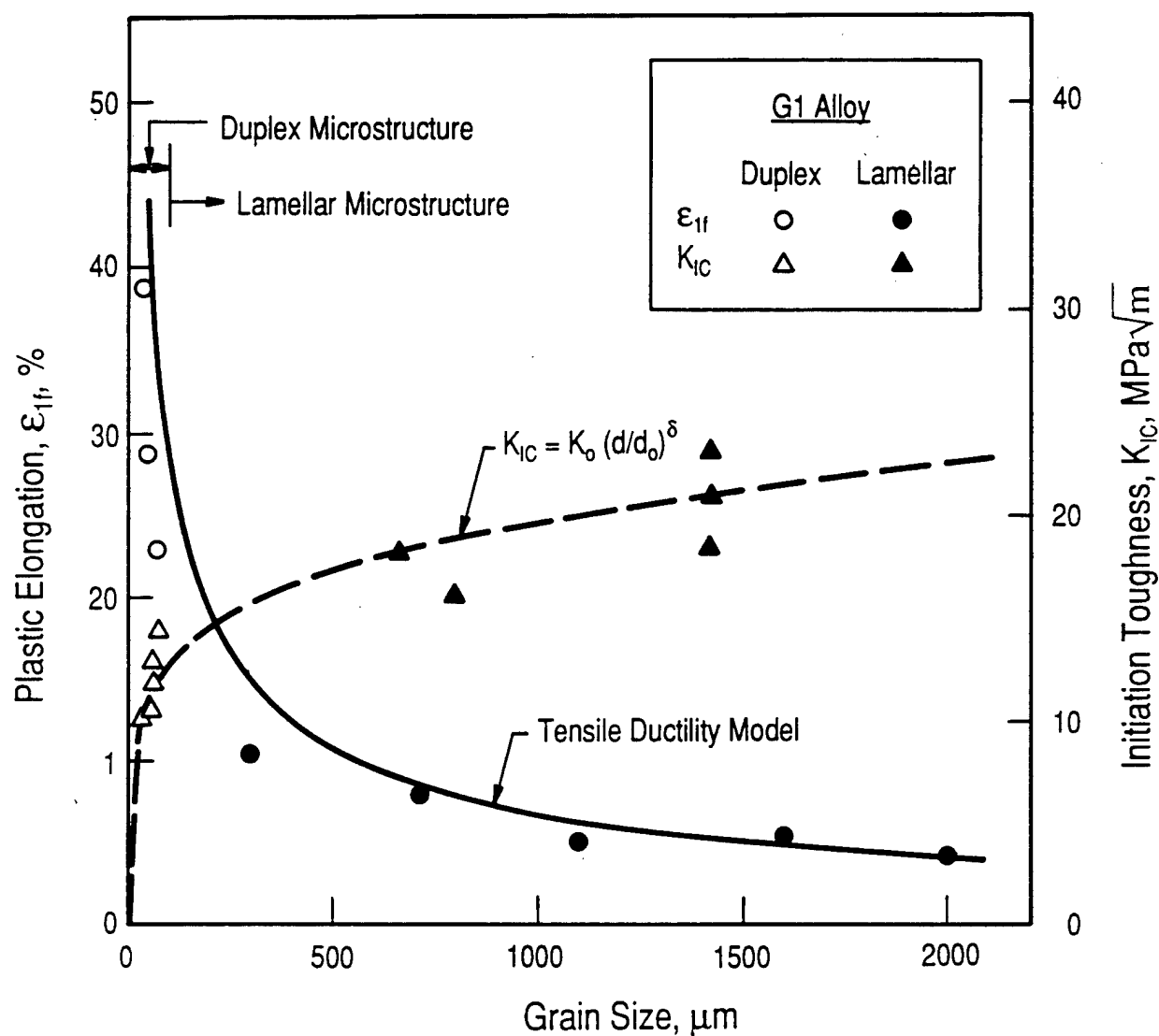
Fig. 63. Plot of plastic elongation and initiation toughness, K_{IC}, as a function of grain size showing an inverse relationship between K_{IC} and plastic elongation. The solid line is calculated based on the tensile ductility model proposed by Chan [37,38] using the experimentally observed K_{IC} and d relation, dashed line, as model input.
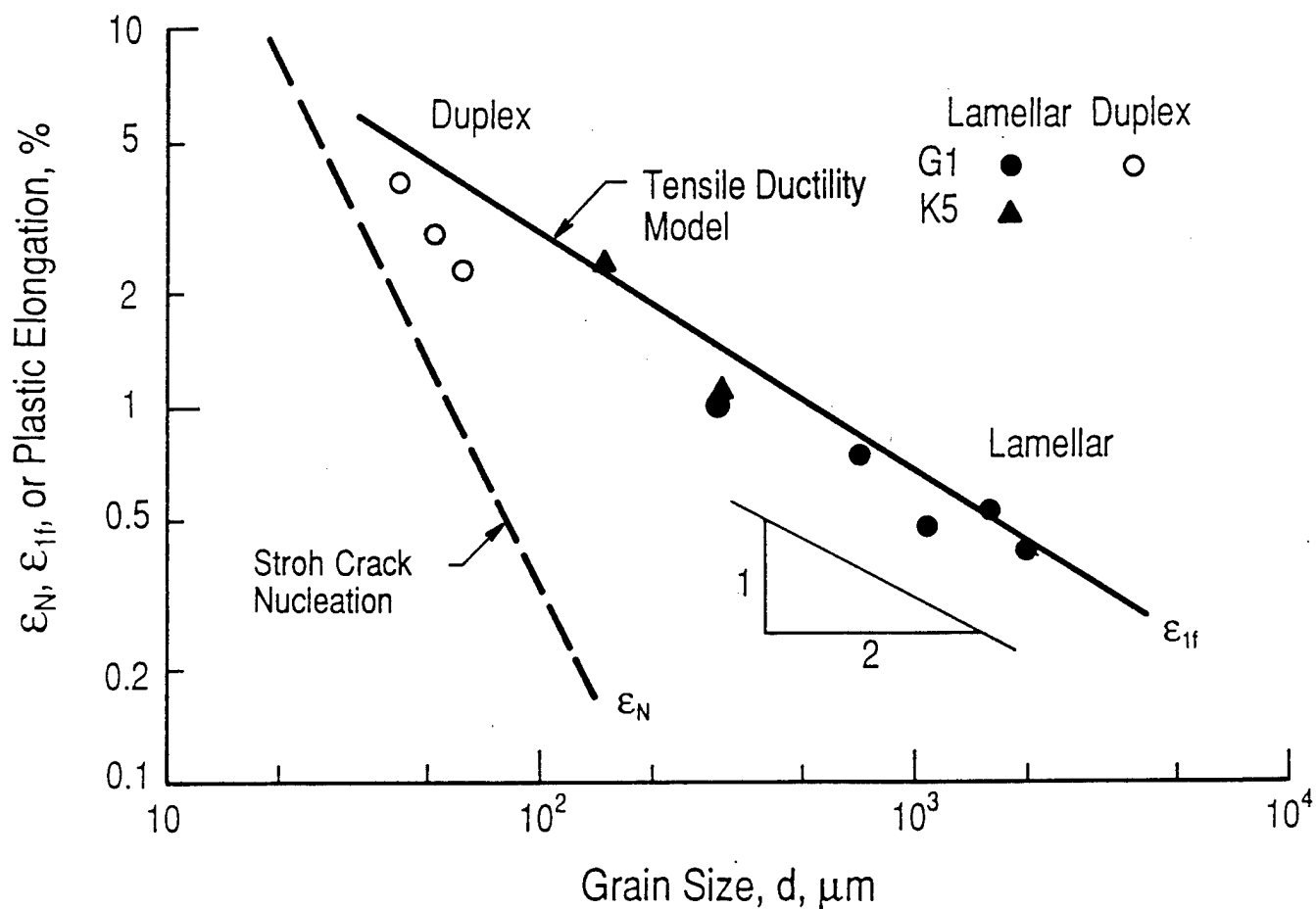
Fig. 64. Decrease of plastic elongation with increasing grain size.
Experimental data are from [36]. The solid line is based on the
tensile ductility model proposed by Chan [37,38] using the
experimentally observed K_{IC} and d relation, Eq. (5), as model input.
The dashed line, Eq. (6), is the calculated plastic strain at crack
nucleation by the Stroh process [39].

K_{IC} value, (2) reduce the effective length of the microstructural unit size or crack size, (3) prevent or delay the onset of microcrack nucleation, and (4) alter the dependence of K_{IC} on grain size currently observed in TiAl alloys.

These challenges can be tackled if the microcrack nucleation process is better understood. Unfortunately, only a limited understanding of the microcrack nucleation process has been developed so far. Microcrack nucleation in TiAl alloys has been modeled recently by assuming microcrack nucleation occurs when the pile-up stress reaches a critical value, i.e., by the Stroh process [39]. The analysis indicates that the plastic strain, ε_N, at microcrack nucleation is related to the grain size, d, according to the expression given by [29,40]

$$\varepsilon_N \, (d)^{\frac{n}{2}} = \alpha' \left(\frac{3}{\pi} \right)^{\frac{n}{2}} \left(\frac{\sigma_y}{E} \right) \left(\frac{K_{IC}}{4\sigma_y} \right)^n \tag{6}$$

which indicates that a log-log plot of ε_N versus d should give a slope of n/2, where n is the inverse of the strain hardening exponent. Eq. (6) is compared with the tensile ductility model and the experimental data of G1 alloy in **Figure 64**. For the G1 alloy, n = 6 and δ = 0.183. The slope for Stroh crack nucleation is about -3, while it is -0.54 for the crack instability criterion based on the tensile ductility model. The comparison reveals that the value of ε_N for microcrack nucleation is small for large-grained materials. If microcrack nucleation occurs by the Stroh process, these microcracks should be observed readily at the onset of yielding. Experimental observation of microcracks during deformation in tensile specimens prior to fracture has been difficult and these ductility limiting microcracks have not been observed. On the other hand, experimental evidence from crack-tip strain measurements indicates [29] that microcracks in TiAl alloys are formed after yielding has occurred, and the plastic strain at crack nucleation is greater than 1% [30,40]. The controlling mechanisms of crack nucleation, however, remain poorly understood. Further study is required to identify and alleviate the limiting process controlling microcrack nucleation in lamellar TiAl alloys in order to increase the K_{IC} value or alter the dependence of K_{IC} on grain size.

VI. ACKNOWLEDGEMENTS

VII. REFERENCES

1. D.M. Shah and D.L. Anton, *Mat. Sci. and Eng.*, v. A153, 1992, pp. 402-409.

2. D.L. Anton and D.M. Shah, *Mat. Sci. and Eng.*, v. A 153, 1992, 410-415.

3. D.L. Anton and D.M. Shah, *Mat. Res. Soc. Proc.*, v. 194, Pittsburgh, PA, 1990, pp. 45-52.

4. R.T. Begley "Columbium Alloy Development at Westinghouse" in Evolution of Refractory Metals and Alloys, E.N.C. Dalder, T. Grobstein, and C.S. Olsen, eds., TMS, Warrendale, PA, 1993.

5. D.J. Thoma "Microstructural Development in Niobium Chromium (2) — Based Alloys" PhD Dissertation, Univ. of Wisconsin, Madison, 1992, avail. from Univ. Microfilms, Ann Arbor, MI.

6. R.L. Fleischer and R.J. Zabala, *Met. Trans. A*, v. 21A, 1990, pp. 2149-2154.

7. V.K. Sikka, S. Viswanathan, and E.A. Loria "Processing and Properties of Nb-Ti-Based Alloys,"

8. M.F. Ashby, *Acta Met.*, v. 21, 1993, pp. 1313-1335.

9. M.G. Mendiratta, J.J. Lewandowski, and D.M. Dimiduk, *Met. Trans. A*, v. 22A, 1991, pp. 1573-1583.

10. R.M. Nekkanti and D.M. Dimiduk, *Mat. Res. Soc. Proc.*, v. 194, Pittsburgh, PA, 1990, pp. 175-183.

11. J.W. Martin, "Micromechanisms in Particle-Hardened Alloys," Cambridge Univ. Press, 1980, p. 41ff.

12. E. Fariabi, A.L.W. Collins, and K. Salama, *Mat. Trans. A*, v. 14A, 1983, pp. 701-707.

13. B.P. Somerday and R.P. Gangloff, "Global Constraint-Insensitive Fracture in SiC Particulate-Reinforced AA 2009," *Met. Trans. A*, v. 25A, 1994, pp. 1471-1479.

14.   S. Jun, *Int. J. Fracture*, v. 54, 1992, pp. 235-242.

15.   Y-H Kim, D. Kwon, and S. Lee, *Acta Metall. Mater.*, v. 42, 1994, pp. 1887- 1891.

16.   A. Mendelson "Plasticity: Theory and Application" R.E. Krieger Publ. Co., Malabar, FL, 1968, pp. 41 & 129.

17.   K. S. Chan, *Met. Trans. A*, Vol. 23A, 1992, pp. 183-199.

18.   A. F. Brown and M. Ortiz, *J. Mech. Phys. Solids*, Vol. 39, 1991, pp. 815-858.

19.   D.L. Davidson, J.B. Campbell and B.K. Chapa "Cyclic Plasticity and Small Fatigue Crack Growth in a TiAl-Based Alloy with a Lamellar Microstructure," *Met. Trans. A*, (submitted).

20.   D.L. Davidson and J.B. Campbell, *Met. Trans. A*, v. 24A, 1993, pp. 1555- 1574.

21.   "Fatigue and Fracture in Lamellar TiAl Alloys," K. S. Chan and D. L. Davidson, *Structural Intermetallics*, R. Darolia, et al. eds., TMS, Warrendale, PA, 1993, pp. 223-230.

22.   "Tensile Ductility of Extrinsically Toughened Intermetallics," K. S. Chan, *Metallurgical Transactions A.*, vol. 25A, 1994, pp. 299-308.

23.   "Relationships of Slip Morphology, Microcracking, and Fracture Resistance in Lamellar TiAl-Alloy," K. S. Chan and Y-W. Kim, *Metallurgical Transactions A.*, Vol. 25A, 1994, pp. 1217-1228.

24.   "Effects of Lamellae Spacing and Colony Size on the Fracture Resistance of a Fully Lamellar TiAl Alloy," K. S. Chan, *Acta Metallurgica et. Materialia*, Vol. 43, 1995, pp. 439-451.

25.   "Microstructure/Fatigue Crack Growth Relationships in Titanium Alloys and Aluminides," K. S. Chan, *Harold Margolin Symposium Conference Proceedings*, S. Ankem and J. A. Hall, eds., TMS, Warrendale, PA, 1994.

26.   "Evidence of Shear Ligament Toughening in TiAl-base Alloys," by K. S. Chan, *Metallurgical and Materials Transactions A*, 1995 (in press).

27.   "Crack-Tip Shielding Mechanisms in Lamellar Intermetallics," by K. S. Chan, *Proceedings of Intrinsic and Extrinsic Fracture Mechanisms in Inorganic Composite Systems*, J. J. Lewandowski and W. H. Hunt, Jr., eds, TMS, Warrendale, PA, 1995, pp. 157-166.

28. "Fracture Toughness of Multiphase Intermetallics," by K. S. Chan, *High-Temperature Ordered Intermetallic Alloys — VI*, MRS Symposium Proceedings, 1994 (in press).

29. "Microstructural Effects on Fracture Resistance in TiAl-base Alloys," by K. S. Chan, *Proceedings of International Symposium on Gamma Titanium Aluminides*, TMS, Warrendale, PA, 1995 (in press).

30. K. S. Chan and Y-W. Kim, *Met. Trans. A*, Vol. 23A, 1992, pp. 1663-1677.

31. K. S. Chan, *Met. Trans. A*, Vol. 22A, 1991, pp. 2021-2029.

32. K. S. Chan, *Met. Trans. A*, Vol. 23A, 1992, pp. 182-199.

33. S. L. Kampe, P. Sadler, D. E. Larsen, and L. Christodoulou, *Microstructure/Property Relationships in Titanium Alloys and Titanium Aluminides*, ed. Y-W. Kim and R. R. Boyer (Warrendale, PA: TMS, 1991) pp. 313-322.

34. E. O. Hall, *Proc. Phys. Soc., London*, Vol. 64 (B), 1951, pp. 747-753.

35. M. J. Petch, *J. Iron Steel Inst.*, Vol. 174, 1953, pp. 25-28.

36. Y-W. Kim, *JOM*, Vol. 46 (7), 1994, pp. 30-39.

37. K. S. Chan, *Met. Trans. A*, Vol. 25A, 1994, pp. 299-308.

38. K. S. Chan, *Scripta Met.*, Vol. 24, 1990, pp. 1725-1730.

39. A. N. Stroh, *Proc. Roy. Soc. A*, Vol. 232, 1955, pp. 548-561.

40. K. S. Chan, Southwest Research Institute, unpublished research, 1995.

VIII. PUBLICATIONS

1. "Fatigue and Fracture in Lamellar TiAl Alloys," K. S. Chan and D. L. Davidson, *Structural Intermetallics*, R. Darolia, et al. eds., TMS, Warrendale, PA, 1993, pp. 223-230.

2. "Tensile Ductility of Extrinsically Toughened Intermetallics," K. S. Chan, *Metallurgical Transactions A.*, vol. 25A, 1994, pp. 299-308.

3. "Relationships of Slip Morphology, Microcracking, and Fracture Resistance in Lamellar TiAl-Alloy," K. S. Chan and Y-W. Kim, *Metallurgical Transactions A.*, Vol. 25A, 1994, pp. 1217-1228.

4. "Effects of Lamellae Spacing and Colony Size on the Fracture Resistance of a Fully Lamellar TiAl Alloy," K. S. Chan, *Acta Metallurgica et. Materialia*, Vol. 43, 1995, pp. 439-451.

5. "Microstructure/Fatigue Crack Growth Relationships in Titanium Alloys and Aluminides," K. S. Chan, *Harold Margolin Symposium Conference Proceedings*, S. Ankem and J. A. Hall, eds., TMS, Warrendale, PA, 1994.

6. "Evidence of Shear Ligament Toughening in TiAl-base Alloys," by K. S. Chan, *Metallurgical and Materials Transactions A*, 1995 (in press).

7. "Crack-Tip Shielding Mechanisms in Lamellar Intermetallics," by K. S. Chan, *Proceedings of Intrinsic and Extrinsic Fracture Mechanisms in Inorganic Composite Systems*, J. J. Lewandowski and W. H. Hunt, Jr., eds, TMS, Warrendale, PA, 1995, pp. 157-166.

8. "Fracture Toughness of Multiphase Intermetallics," by K. S. Chan, *High-Temperature Ordered Intermetallic Alloys — VI*, MRS Symposium Proceedings, 1994 (in press).

9. "Microstructural Effects on Fracture Resistance in TiAl-base Alloys," by K. S. Chan, *Proceedings of International Symposium on Gamma Titanium Aluminides*, TMS, Warrendale, PA, 1995 (in press).

10. "Fatigue Crack Growth Through the Lamellar Microstructure of an Alloy Based on TiAl at 25° and 800°C," by D. L. Davidson and J. B. Campbell, *Met. Trans. A*, 24A, 1993, pp. 1555-1574.

11. "Cyclic Plasticity and Small Fatigue Crack Growth in a TiAl-Based Alloy With a Lamellar Microstructure," *Met. Trans. A* (submitted).

IX. LIST OF PRESENTATIONS

1. "Fracture Toughness of Multiphase Intermetallics," by K. S. Chan, Invited Paper, MRS Symposium on High Temperature Order Intermetallics — VI, MRS Fall Meeting, Boston, November 28-December 2, 1994.

2. "Microstructural Effects on Fracture Resistance in TiAl-base Alloys," by K. S. Chan, Invited Paper, International Symposium on Gamma Titanium Aluminides, TMS Annual Meeting, Las Vegas, February 12-16, 1995.

3. "Crack-Tip Shielding Mechanisms in Lamellar Intermetallics," by K. S. Chan, Symposium on Intrinsic and Extrinsic Fracture Mechanisms in Inorganic Composite Systems, TMS Annual Meeting, Las Vegas, February 12-16, 1995.

4. "Microstructural Effects on Fracture Resistance in TiAl Intermetallic Alloys," by K. S. Chan, Seminar to Materials Laboratory, Wright-Patterson AFB, OH, September 30, 1994.

5. "Cyclic Deformation and Fatigue Crack Initiation in a Lamellar TiAl-Based Alloy," by D. L. Davidson, TMS Meeting, Pittsburgh, PA, October 1993.

APPENDIX

Appendix
Derivation of Constraint In Terms of Strain

Constraint is usually defined as $\sigma_{mean}/\sigma_{effective}$. The purpose of this derivation is to show the equivalent definition of constraint in terms of strains.

1. Mendelson [16] gives expressions for stress and strain for a loading path divided into N segments. The total strain for the ith increment is

$$\epsilon_1 = \frac{1}{E}\left[\sigma_1 - \nu(\sigma_2 + \sigma_3)\right] + \Delta\epsilon_1^P \qquad \epsilon_2 = \frac{1}{E}\left[\sigma_2 - \nu(\sigma_1 + \sigma_3)\right] + \Delta\epsilon_2^P$$

$$\epsilon_3 = \frac{1}{E}\left[\sigma_3 - \nu(\sigma_1 + \sigma_2)\right] + \Delta\epsilon_3^P$$

   where ϵ_i = total principal strain, and $\Delta\epsilon_i^P$ = plastic component.

2. At the surface $\sigma_3 = 0$; i.e., the condition is plane stress.

3. Mean strain in-plane = $\epsilon_m = \dfrac{1}{2}(\epsilon_1 + \epsilon_2) = \dfrac{1}{2}\left\{\dfrac{1}{E}\left[\sigma_1 - \nu\sigma_2\right] + \Delta\epsilon_1^P + \dfrac{1}{E}\left[\sigma_2 - \nu\sigma_1\right] + \Delta\epsilon_2^P\right\}$

$$2\epsilon_m = \left[\frac{(1-\nu)}{E}(\sigma_1 + \sigma_2) + \Delta\epsilon_1^P + \Delta\epsilon_2^P\right]$$

4. From Mendelson, $\Delta\epsilon_1^P = \dfrac{\Delta\epsilon_P}{2\sigma_e}(2\sigma_2 - \sigma_2) \qquad \Delta\epsilon_2^P = \dfrac{\Delta\epsilon_P}{2\sigma_e}(2\sigma_2 - \sigma_1)$

   where σ_e = effective (or von Mises) stress = $\left[\sigma_1^2 + \sigma_2^2 - \sigma_1\sigma_2\right]^{1/2}$ for plane stress, and $\Delta\epsilon_P$ = effective strain.

   Therefore, $\qquad 2\sigma_m = \left[\left(\dfrac{1-\nu}{E}\right)(\sigma_1 + \sigma_2) + \dfrac{\Delta\epsilon_P}{2\sigma_e}(\sigma_1 + \sigma_2)\right]$

5. Assuming dominance by plasticity: $\epsilon_P > \epsilon_e \qquad 2\epsilon_m = \dfrac{\Delta\epsilon_P}{2\sigma_e}(\sigma_1 + \sigma_2)$

6. Constrain in terms of strain = $\dfrac{\epsilon_m}{\epsilon_{eff}}$ where $\epsilon_{eff} = \dfrac{2}{\sqrt{3}}\left(\epsilon_1^2 + \epsilon_2^2 + \epsilon_1\epsilon_2\right)^{1/2}$

$$\frac{\epsilon_m}{\epsilon_{eff}} = \frac{\sigma_1 + \sigma_2}{4\sigma_e} = \frac{\sigma_1 + \sigma_2}{4\left(\sigma_1^2 + \sigma_2^2 - \sigma_1\sigma_2\right)^{1/2}} = \frac{\sigma_m}{\sigma_{eff}}$$

Thus, there is an equivalence of constraint whether determined from stress or strain for the unique case when $\sigma_3 = 0$.